

Discrimination of Alpha Particles in CdZnTe Detectors with Coplanar Grid

(Diskriminierung von Alphateilchen in CdZnTe-Detektoren mit koplanarem Gitter)

von

Henning Rebber

geboren am

03.06.1988

**Masterarbeit im Studiengang Physik
Universität Hamburg**

2015

- 1. Gutachter: Dr. Björn Sönke Wonsak**
- 2. Gutachterin: Prof. Dr. Caren Hagner**

Abstract

The aim of the COBRA experiment is the search for neutrinoless double beta decay using CdZnTe semiconductor detectors. A background rate in the order of 10^{-3} counts per keV, kg and year is intended in order to be sensitive to a half-life larger than 10^{26} years. Measurements from a demonstrator set-up and Monte Carlo simulations indicate that a large background component is due to alpha particles. These generate charge clouds of only few μm in diameter in the detector, leading to characteristic pulse features.

Parameter-based cut criteria were developed to discriminate alpha events by means of their pulse shapes. The cuts were tested on data from alpha and beta irradiation of a $(1 \times 1 \times 1) \text{ cm}^3$ CdZnTe detector with coplanar grid. The pulse shapes of all event signals were read out by FADCs with a sampling rate of 100 MHz. It was possible to reduce the alphas to 20 % while nearly 60 % of the betas survived for 2 MeV particles. The results were reproduced well by a detector simulation which hence was used to study the cut for energies up to 3 MeV and different detector regions. The simulations show an enhanced cut performance towards the anode plane and for higher energies. Assuming a uniformly distributed alpha contamination, the COBRA half-life sensitivity could be increased by $(70 \pm 24) \%$. For a surface-only contamination, the gain is predicted to be $(32 \pm 19) \%$.

The applied detector simulation is a tool designed for COBRA. In the course of this thesis, it was substantially further developed based on 3D simulations of the electric field and studies of drift effects such as thermal diffusion, electrostatic repulsion and carrier trapping. All major effects in charge transport and electronic impacts during signal transmission are now being considered.

Zusammenfassung

Das Ziel des COBRA-Experiments ist die Suche nach neutrinolosem Doppelbetazerfall mit CdZnTe-Halbleiterdetektoren. Es wird eine Untergrundrate von 10^{-3} Ereignissen pro keV, kg und Jahr angestrebt, um eine Sensitivität auf die Halbwertszeit von mehr als 10^{26} Jahren zu erreichen. Aus Messungen an einem Demonstratoraufbau sowie aus Monte-Carlo-Simulationen ist bekannt, dass ein Großteil des Untergrundes auf Alphateilchen zurückzuführen ist. Diese generieren im Detektor Ladungswolken von nur wenigen μm im Durchmesser. Die Folge sind charakteristische Signaleigenschaften.

Es wurden parameterbasierte Schnittkriterien entwickelt, um Alpha- von Betaereignissen anhand ihrer Pulsformen zu unterscheiden. Diese wurden auf Daten angewandt, die zuvor durch Bestrahlung eines $(1 \times 1 \times 1) \text{ cm}^3$ großen CdZnTe-Detektors mit koplanarem Gitter gewonnen wurden. Die Pulsformen aller Ereignisse wurden von FADCs mit einer Abtastrate von 100 MHz ausgelesen. Bei Teilchenenergien von 2 MeV konnten die Alphas auf 20 % reduziert werden, während nahezu 60 % der Betas überlebten. Die Ergebnisse konnten von einer Detektorsimulation reproduziert werden, die daraufhin für die Untersuchung von Energien bis zu 3 MeV und unterschiedlicher Detektorbereiche eingesetzt wurde. Entgegen der Anodenfläche und zu höheren Energien prognostizieren die Simulationen eine gesteigerte Leistungsfähigkeit der Schnitte. Unter der Annahme, dass Verunreinigungen durch Alphazerfälle gleichmäßig über den Detektor verteilt sind, könnte die Sensitivität von COBRA auf die Halbwertszeit um $(70 \pm 24) \%$ erhöht werden. Im Falle einer ausschließlichen Oberflächenkontamination läge die Steigerung bei $(32 \pm 19) \%$.

Die verwendete Detektorsimulation ist ein eigens für COBRA entwickeltes Werkzeug. Im Zuge dieser Arbeit wurde es, basierend auf 3D-Simulationen des elektrischen Feldes und Studien von Drifteffekten wie etwa thermischer Diffusion, elektrostatischer Abstoßung und Ladungsverlust durch Trapping, maßgeblich weiterentwickelt. Alle Hauptaspekte des Ladungstransports und der elektronischen Einflüsse während der Signalübermittlung werden nun berücksichtigt.

Contents

| | | |
|----------|--|-----------|
| 1 | Introduction | 9 |
| 2 | Neutrino Physics | 11 |
| 2.1 | Neutrino Oscillations | 11 |
| 2.2 | Majorana Fermions | 13 |
| 2.2.1 | Lagrangian Mass Terms and the Seesaw Mechanism | 14 |
| 2.2.2 | Effective Majorana Mass | 16 |
| 2.3 | Double Beta Decay | 17 |
| 2.3.1 | Derivation and Decay Modes | 17 |
| 2.3.2 | Decay Rates | 20 |
| 2.3.3 | Detection | 21 |
| 3 | The COBRA Experiment | 24 |
| 3.1 | Idea and Concept | 24 |
| 3.2 | Background Sources | 26 |
| 3.2.1 | Primordial Background | 26 |
| 3.2.2 | Cosmogenic Background | 27 |
| 3.2.3 | Neutrons | 27 |
| 3.2.4 | $2\nu\beta\beta$ Decay | 28 |
| 3.3 | Demonstrator Setup | 28 |
| 3.3.1 | Shielding | 29 |
| 3.3.2 | DAQ Chain | 31 |
| 3.3.3 | Current Status | 32 |
| 3.4 | Large-Scale Prospects | 34 |
| 4 | Properties of CdZnTe CPG Detectors | 37 |
| 4.1 | Signal Generation | 38 |
| 4.1.1 | Shockley-Ramo Theorem | 38 |
| 4.1.2 | Pulse Shapes | 39 |
| 4.1.3 | Reconstruction of Energy and Interaction Depth | 41 |
| 4.2 | Charge Cloud Dynamics | 42 |
| 4.2.1 | Size and Shape of the Initial Cloud | 43 |

| | | |
|----------|---|------------|
| 4.2.2 | Trapping | 46 |
| 4.2.3 | Thermal Diffusion | 48 |
| 4.2.4 | Electrostatic Repulsion | 48 |
| 4.3 | Electric Field Studies | 50 |
| 4.3.1 | Electrode Biases | 50 |
| 4.3.2 | Space Charge Regions | 52 |
| 4.3.3 | Metal-Semiconductor Junctions | 52 |
| 5 | Development of a Detector Simulation | 57 |
| 5.1 | Process | 58 |
| 5.1.1 | VENOM Event Simulation | 60 |
| 5.1.2 | Calculating Tracks | 60 |
| 5.1.3 | Generating Signals | 64 |
| 5.1.4 | Adding Impact of Electronics | 66 |
| 5.2 | Results | 68 |
| 5.2.1 | Pulse Samples | 68 |
| 5.2.2 | Energy Resolution | 71 |
| 5.3 | Discussion | 73 |
| 6 | Development of an Alpha Discrimination Cut | 75 |
| 6.1 | Definition of Cut Parameters | 76 |
| 6.2 | Pulse Smoothing and Differentiation | 78 |
| 6.2.1 | Mean Value Method | 78 |
| 6.2.2 | Whittaker-Henderson Method | 78 |
| 6.3 | Test with Laboratory Measurements | 80 |
| 6.3.1 | Setup | 80 |
| 6.3.2 | Pulse Shape Analysis | 80 |
| 6.3.3 | Discussion | 85 |
| 6.4 | Test with Simulated Data | 87 |
| 6.4.1 | Reproduction of Laboratory Measurements | 88 |
| 6.4.2 | Depth Dependent Efficiency | 89 |
| 6.4.3 | Overall Efficiency | 91 |
| 6.4.4 | Lateral Surface Efficiency | 95 |
| 6.5 | Test with Coincidence Data | 95 |
| 6.6 | Discussion | 97 |
| 7 | Conclusion and Outlook | 100 |
| A | Natural Decay Chains | 102 |
| B | Software | 105 |

| | |
|------------------------|------------|
| List of Figures | 108 |
| List of Tables | 109 |
| Bibliography | 115 |

Chapter 1

Introduction

The semiconducting compound material cadmium zinc telluride – also CdZnTe or simply CZT – has gained growing importance over the last decades. Proclaimed in the 1970s as a promising candidate to replace germanium detectors, which need cooling to cryogenic temperatures, CdTe and later also CZT crystals can by now be produced in high quality thanks to remarkable progress in the technology of crystal growth in the 1990s [TW00, Sch01]. A large band gap allows for room temperature operation. The high density makes CZT suitable for hard X-ray and γ -ray detection. The energy resolution is high enough for spectroscopic purposes. Nowadays, CZT devices are commonly used for nuclear instrumentation in science and industry as well as for medical imaging.

A substantial role for CZT is foreseen at the COBRA experiment. COBRA is a next generation experiment to search for neutrinoless double beta ($0\nu\beta\beta$) decay. Not only do CZT crystals have the function to detect the signal, they also serve as source of the decay, since several candidate isotopes are contained. $0\nu\beta\beta$ decay would, if actually observed, represent a twofold violation of the total lepton number – a fact clearly contradicting the Standard Model of particle physics. For the neutrino itself, this would mean that it is identical to its own antiparticle, a so-called Majorana particle. Furthermore, the measured half-life can give a hint on the ordering of neutrino mass eigenstates, known as mass hierarchy. The comprehension of these fundamental aspects of particle physics has also contribution to the solution of hot astroparticle and cosmological problems, related to the neutrino mass scale and nature [GP12].

Half-lives of $0\nu\beta\beta$ decay are predicted to be in the order of 10^{26} years and higher. The extreme rarity demands for a detector operation under ultra low background conditions. Currently, a demonstrator setup is taking data with an array of 1 cm^3 CZT detectors of coplanar grid (CPG) type [T⁺15]. A multi-layer shielding and additional analysis cuts suppress the background to less than $1\frac{\text{counts}}{\text{keV}\cdot\text{kg}\cdot\text{yr}}$. The aim is to reach $10^{-3}\frac{\text{counts}}{\text{keV}\cdot\text{kg}\cdot\text{yr}}$ in order to be sensitive to $2 \cdot 10^{26}$ years of half-life, corresponding to a Majorana mass of 0.05 eV.

The current background is dominated by alpha-induced events. With regard to detection sensitivity, a lot can be gained from methods to separate these from the signal, i.e. the two betas emerging from $0\nu\beta\beta$ decay. The point of departure for a discrimination is the different ionization

behavior of alphas and betas, leading to characteristic attenuation lengths. While incident alphas travel only a couple of μm in CZT, betas of comparable energy cover up to mm distances. It could be verified with pixelated CdTe detectors that the clouds of generated electrons and holes are indeed much more compact for alphas than for betas [Gle14]. At COBRA, fast analog-to-digital converters allow for a detailed analysis of the pulse shapes. An extended charge cloud causes the charge collection at the electrodes to take longer. An impact on the detector signals is expected.

In the course of this thesis it is investigated how the different sizes and profiles of the clouds affect the detector signals with regard to a discrimination of alpha events. The following chapter gives an overview on the aspects of neutrino physics that motivate the COBRA experiment. The experiment itself is presented in chapter 3, including a description of the readout chain and shielding currently in use for the demonstrator. Chapter 4 is devoted to the function and features of CZT detectors with CPG design. It is explained how signals arise and how event reconstruction is done. Great emphasis was placed on the generation and transport of charge clouds. Simulations of the electric field inside the detectors are presented, taking into account also surface effects and junctions. Chapter 5 describes a detector simulation which was developed for COBRA to reproduce pulse shapes of CPG devices. Throughout this thesis, the tool was essentially further developed and can now be used for validations of pulse shape analyses and efficiency predictions. The conclusions from the previous chapter are considered to provide appropriate treatment of drift effects. The CPG studies are also the basis of the pulse shape analysis presented in chapter 6. Suitable parameters are developed to tell alpha from beta events. Cut criteria are formulated and used on signals from dedicated measurements. The detector simulation is used to investigate the cut behavior in different detector areas and to predict cut efficiencies. All results are summarized and briefly reviewed in a final chapter.

Chapter 2

Neutrino Physics

During the past 50 years a series of discoveries changed the fundamental assumptions in particle physics every so often, always going along with a deeper understanding of the basic elements and concepts that our world is made of. The Standard Model (SM) that was developed throughout the decades helps to explain various observations but is also stretched to its limits at some points, especially in the neutrino sector. The facts that neutrinos are able to change their flavor eigenstates and must therefore have finite mass are both not compatible with the conservative SM theories. Furthermore it is believed that neutrinos are Majorana fermions, another property not anticipated by the SM.

This chapter gives a brief overview on some of the various aspects of neutrino physics and the latest observations in this field. The basic concept of neutrino oscillations are depicted, leading to two contrary mass hierarchies. Majorana fermions are introduced before both neutrino accompanied and neutrinoless double beta decay are treated.

2.1 Neutrino Oscillations

In the early 1970s, R. Davis *et al.* were the first to observe the solar neutrino problem [BD76]. In the Homestake experiment they measured the rate of electron neutrinos (ν_e) produced by nuclear fusion in the sun and found that a significantly lower rate of ν_e reached the earth than predicted.

The neutrino oscillation is a mechanism to explain this issue. According to the formalism neutrinos can be described by either mass eigenstates $|\nu_i\rangle$ with eigenvalues m_i or flavor eigenstates $|\nu_\alpha\rangle$ which are linear superpositions of each other:

$$|\nu_\alpha\rangle = \sum_i U_{\alpha i} |\nu_i\rangle, \quad |\nu_i\rangle = \sum_\alpha U_{\alpha i}^* |\nu_\alpha\rangle, \quad (2.1)$$

where the $U_{\alpha i}$ are the entries of a unitary mixing matrix U and the $U_{\alpha i}^*$ their complex conjugations. Neutrinos take part in weak interactions in their flavor eigenstates. The underlying mass eigenstates are time dependent and while a neutrino propagates through space the probability

Table 2.1: Current values for mixing angles and squared mass differences [Gro14]. Where necessary, values are given both for normal and inverted mass hierarchy (NH and IH, respectively).

| Parameter | Value |
|---------------------------|---|
| $\sin(2\theta_{12})$ | 0.846 ± 0.021 |
| $\sin(2\theta_{23})_{NH}$ | $0.999^{+0.001}_{-0.018}$ |
| $\sin(2\theta_{23})_{IH}$ | $1.000^{+0.000}_{-0.017}$ |
| $\sin(2\theta_{13})$ | $(9.3 \pm 0.8) \cdot 10^{-2}$ |
| Δm_{21}^2 | $(7.53 \pm 0.18) \cdot 10^{-5} \text{eV}^2$ |
| $ \Delta m_{32}^2 _{NH}$ | $(2.44 \pm 0.06) \cdot 10^{-3} \text{eV}^2$ |
| $ \Delta m_{32}^2 _{IH}$ | $(2.52 \pm 0.07) \cdot 10^{-3} \text{eV}^2$ |

to find it in a certain flavor eigenstate changes. For a neutrino with energy E that is produced as $|\nu_\alpha\rangle$, the probability to observe it as $|\nu_\beta\rangle$ after a travelling distance L in vacuum¹ is given as

$$P(\alpha \rightarrow \beta, L) = \sum_{i,j} U_{\alpha i} U_{\alpha j}^* U_{\beta i}^* U_{\beta j} \exp\left(-i \frac{\Delta m_{ij}^2 L}{2E}\right) \quad (2.2)$$

with Δm_{ij}^2 being the squared mass difference between m_i and m_j . Thus an oscillation between flavor eigenstates arises whose frequency is given by the Δm_{ij}^2 and whose amplitude is defined by the $U_{\alpha i}$. In case of three neutrino flavors ($\alpha = e, \mu, \tau, i = 1, 2, 3$) the mixing matrix can be parametrized as follows:

$$U_{PMNS} = \begin{pmatrix} 1 & 0 & 0 \\ 0 & \cos \theta_{23} & \sin \theta_{23} \\ 0 & -\sin \theta_{23} & \cos \theta_{23} \end{pmatrix} \begin{pmatrix} \cos \theta_{13} & 0 & \sin \theta_{13} e^{-i\delta_{CP}} \\ 0 & 1 & 0 \\ -\sin \theta_{13} e^{i\delta_{CP}} & 0 & \cos \theta_{13} \end{pmatrix} \begin{pmatrix} \cos \theta_{12} & \sin \theta_{12} & 0 \\ -\sin \theta_{12} & \cos \theta_{12} & 0 \\ 0 & 0 & 1 \end{pmatrix}. \quad (2.3)$$

Besides the three mixing angles θ_{ij} , a complex phase δ_{CP} is introduced which allows for CP violation. U_{PMNS} is usually referred to as PMNS matrix² [MNS62].

From the 1990s on, numerous experiments (e.g. SNO, SuperKamiokande, KamLAND, OPERA) confirmed the oscillation nature of neutrinos and helped to determine all mixing angles and squared mass differences. The value for δ_{CP} has not been determined yet. Current oscillation parameters are listed in table 2.1. It was found that Δm_{21}^2 is two orders of magnitude smaller than $|\Delta m_{32}^2|$ and it can be concluded that $|\Delta m_{32}^2| \approx |\Delta m_{31}^2|$. No absolute masses are known, so that it is in principle possible for the lightest m_i to be massless. As only the sign of Δm_{21}^2 has been identified yet, two different ways of ordering the mass eigenvalues are thinkable, as illustrated in figure 2.1. The orderings are referred to as mass hierarchies, whereas either m_1 is the lightest mass eigenvalue (normal hierarchy, NH) or m_3 (inverted hierarchy, IH). Up to date no hierarchy could yet be excluded.

¹For neutrino oscillations in matter an adaptation of the formalism has to be made, known as the MSW effect. A detailed description can be found e.g. in [Zub12].

²Pontecorvo-Maki-Nakagawa-Sakata matrix

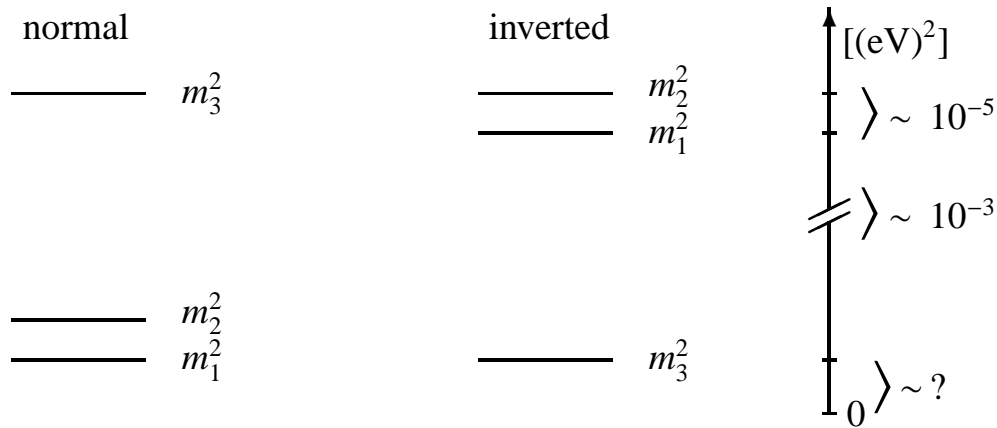


Figure 2.1: Illustration of mass orderings [JT]. Depending on the identity of the lightest mass eigenstate, two orders are thinkable referred to as normal and inverted hierarchy.

2.2 Majorana Fermions

The difference between a Majorana and a Dirac particle can be explained rather simply: A Majorana particle is its own antiparticle while a Dirac particle is not. As the idea and its consequences are fundamental in the context of $0\nu\beta\beta$ -experiments, the following section is dedicated to this topic.

For the following it is useful to have the meaning of chirality in mind. The term often comes along with the concept of helicity, although they do not necessarily mean the same. Helicity is the projection of the particle spin \vec{s} onto the direction of momentum \vec{p} ,

$$\mathcal{H} = \frac{\vec{s}\vec{p}}{|\vec{s}||\vec{p}|} . \quad (2.4)$$

As \vec{s} and \vec{p} are either parallel or antiparallel, $\mathcal{H} = \pm 1$. Chirality describes the way a particle transforms in the Minkowski spacetime isometries³ which is either right- or left-handed. According to the V-A theory of weak interaction, only left-handed particles (right-handed antiparticles) couple to W^\pm bosons. For massless particles on the one side, right-handedness is equivalent to negative (positive) helicity. For particles with rest mass $m \neq 0$ on the other side, chirality and helicity are not inevitably consistent. Here, the probability for a contrary helicity is $P = 1 - \frac{v}{c}$ with v being the velocity of the particle and c the speed of light.

According to the SM, all fundamental fermions are Dirac fermions. Table 2.2 shows the elementary SM fermions and their division into quarks and leptons. The arrangement in so-called isospin doublets implies pairwise identical behavior with respect to weak interactions. As only left-handed particles couple to W^\pm bosons, right-handed particles make up weak isospin singlets. For the existence of right-handed neutrinos no evidence has been found yet and if they

³An isometry is a Lorentz invariant linear bijection. Minkowski spacetime isometries are therefore translations in time or space. The group of all Minkowski spacetime isometries is the Poincaré group.

Table 2.2: Division of the elementary SM fermions into quarks and leptons. Transitions within one generation are possible only for left-handed particles.

| | | | |
|--|--|--|---------|
| $\begin{pmatrix} \nu_e \\ e^- \end{pmatrix}_L$ | $\begin{pmatrix} \nu_\mu \\ \mu^- \end{pmatrix}_L$ | $\begin{pmatrix} \nu_\tau \\ \tau^- \end{pmatrix}_L$ | leptons |
| $\begin{pmatrix} u \\ d' \end{pmatrix}_L$ | $\begin{pmatrix} c \\ s' \end{pmatrix}_L$ | $\begin{pmatrix} t \\ b' \end{pmatrix}_L$ | quarks |
| e^-_R | μ^-_R | τ^-_R | |
| u_R | c_R | t_R | |
| d_R | s_R | b_R | |

exist, they must be sterile, i.e. not taking part in any SM interaction.

As a matter of fact the relative mass difference between neutrinos and any of the charged leptons is by far greater than for quarks within one generation. It so happens that this might be explained by Majorana fermions.

2.2.1 Lagrangian Mass Terms and the Seesaw Mechanism

The relativistic behavior of fermions with spin $\frac{1}{2}$ and mass m was derived by Paul Dirac, who in 1928 described it in [Dir28]. In the equation named after him, Dirac used a wave function ψ to describe the fermion. To consider both particle and antiparticle with each of the spin configurations *up* and *down*, ψ can be treated as a spinor of at least four independent and complex components (Dirac spinor).

In quantum electro dynamics (QED), as in any quantum field theory, the Lagrangian \mathcal{L} determines all fundamental fields and quantum states. Therefore, it is not surprising to find the Dirac equation as part of the QED Lagrangian:

$$\mathcal{L} = \bar{\psi} \left(i\gamma_\mu \frac{\partial}{\partial x_\mu} - m \right) \psi \quad , \quad (2.5)$$

with $\mu = 0, 1, 2, 3$ and the γ_μ being 4×4 matrices. The first term corresponds to the kinetic energy and is thus called kinetic term while the second is the mass term.

ψ can be separated into a right- and a left-handed chiral component by the help of a projection operator $P_{L,R}$ via

$$\psi = \psi_R + \psi_L \quad , \quad \text{where} \quad \psi_{L,R} = P_{L,R}\psi \quad . \quad (2.6)$$

The Dirac mass term can be expressed with the chiral component Weyl spinors as

$$\mathcal{L}_{\text{Dirac}} = m_D (\bar{\psi}_L \psi_R + \bar{\psi}_R \psi_L) \quad , \quad (2.7)$$

speaking now of a Dirac mass m_D instead of m .

In 1937, Ettore Majorana stated that the Dirac equation might be solved for a spinor of four real components, thus describing a fermion that is identical to its antiparticle [Maj37]. Apparently this condition applies only to uncharged particles. For this reason the Majorana character can only apply to the neutrinos.

For the description of a Majorana particle, a two-component spinor is sufficient. The mass term reads

$$\mathcal{L}_{\text{Majorana}} = \frac{1}{2}(m_M \bar{\psi} \psi^c + m_M^* \bar{\psi}^c \psi) = \frac{1}{2}(m_M \bar{\psi} \psi^c) + h.c. \quad (2.8)$$

It was necessary to introduce the charge-conjugated spinor ψ^c and the Majorana mass m_M . Here and below, the letters *h.c.* depict the Hermitian conjugate.

Again it is possible to project the right- and left-handed chiral components of ψ . To formulate a right- and a left-handed mass term, also m_M has to be split, thus

$$\begin{aligned} \mathcal{L}_{\text{Majorana}} &= \mathcal{L}_{\text{Majorana}}^L + \mathcal{L}_{\text{Majorana}}^R \\ &= \frac{1}{2} m_L \bar{\psi}_L \psi_R^c + \frac{1}{2} m_R \bar{\psi}_L^c \psi_R + h.c. \quad (2.9) \end{aligned}$$

In combination, eq. (2.7) and (2.9) lead to the most general mass term

$$\begin{aligned} 2\mathcal{L}_{\text{Dirac-Majorana}} &= m_D(\bar{\psi}_L \psi_R + \bar{\psi}_L^c \psi_R^c) + m_L \bar{\psi}_L \psi_R^c + m_R \bar{\psi}_L^c \psi_R + h.c. \\ &= \begin{pmatrix} \bar{\psi}_L & \bar{\psi}_L^c \end{pmatrix} M \begin{pmatrix} \psi_R^c \\ \psi_R \end{pmatrix} + h.c. \quad \text{with } M = \begin{pmatrix} m_L & m_D \\ m_D & m_R \end{pmatrix} . \quad (2.10) \end{aligned}$$

By diagonalizing M , one can obtain the mass eigenstates and thus the corresponding mass eigenvalues. The pure Dirac case as given by the Dirac Lagrangian in equation (2.7) follows if $m_L = m_R = 0$, then the mass eigenstate is the Dirac mass m_D .

Another popular scenario is the case $m_R \gg m_D$, $m_L = 0$. Two mass eigenvalues are obtained:

$$m_1 = \frac{m_D^2}{m_R}, \quad m_2 = m_R \left(1 + \frac{m_D^2}{m_R^2} \right) \approx m_R \quad (2.11)$$

m_1 can be identified with the mass of the left-handed neutrino, which could in principle explain why the observed mass values are so small. The consequence however would be a very heavy partner neutrino with mass m_2 . Because of the inverse mass relation between the neutrino and its partner, this theory was given the illustrative name *seesaw mechanism*. The reason why we did not already come across the partner neutrino experimentally is its chirality, as it would be right-handed – and therefore sterile. Actually, the massive seesaw partner is one of the candidates for cold dark matter [Dre13, L⁺15]. But on the basis of the above, the key feature to this theory is the Majorana nature of the neutrino.

2.2.2 Effective Majorana Mass

A neutrino will always interact in one of its flavor eigenstates. The electron neutrino mass $\langle m_{\nu_e} \rangle$ observed in experiments measuring the end point of a β -decay spectrum is the incoherent sum of the mass eigenvalues:

$$\langle m_{\nu_e} \rangle = \sqrt{\sum_{i=1}^3 |m_i U_{ei}|^2} . \quad (2.12)$$

The Mainz experiment determined an upper limit of 2 eV for $\langle m_{\nu_e} \rangle$ at 95 % C.L.⁴ by measuring the end point of the tritium decay spectrum [K⁺05, OW08]. Currently the KATRIN experiment is attempting to lower this value down to 0.2 eV [Par13].

As will be depicted in more detail in section 2.3, $0\nu\beta\beta$ -experiments such as COBRA, GERDA and CUORE are sensitive to the coherent sum $\langle m_{\beta\beta} \rangle$ of the mass eigenvalues, often referred to as effective Majorana mass:

$$\langle m_{\beta\beta} \rangle = \left| \sum_{i=1}^3 m_i U_{ei}^2 \right| . \quad (2.13)$$

In case of Majorana neutrinos, the mixing matrix has to be adapted in such a way that

$$U_M = U_{PMNS} \cdot \begin{pmatrix} 1 & 0 & 0 \\ 0 & e^{i\alpha_1} & 0 \\ 0 & 0 & e^{i\alpha_2} \end{pmatrix} . \quad (2.14)$$

The two Majorana phases α_1 and α_2 are introduced as new free parameters of U . It can be seen in equation (2.12) and (2.13) that unlike the effective Majorana mass, the observed neutrino mass $\langle m_{\nu_e} \rangle$ remains untouched by the Majorana phases.

Figure 2.2 is a good illustration of how experiments on the $0\nu\beta\beta$ decay are sensitive to the mass hierarchy and also to the neutrino mass. It shows the dependence of the effective Majorana mass on the lightest neutrino mass. One band appears for each mass hierarchy. The width is determined by the unknown Majorana phases (stripes region). The broadening from the 1σ uncertainties on the oscillation parameters is indicated by the cross hatched region. In case of an inverted hierarchy, $\langle m_{\beta\beta} \rangle$ is always larger than zero. For the normal hierarchy, $\langle m_{\beta\beta} \rangle = 0$ is not excluded. For a minimum neutrino mass below 10^{-2} eV, NH and IH are clearly distinguishable w.r.t. $\langle m_{\beta\beta} \rangle$. They become degenerate above that value. From measurements of the cosmic microwave background as part of the PLANCK experiment, the direct sum of the active neutrino masses is known to be $\sum_i m_i < 0.23$ eV at 95 % C.L. [LP14]. Therefore, the plot region for higher neutrino masses is disfavored by cosmology. As described in the following section, the half-life of the $0\nu\beta\beta$ decay depends on $\langle m_{\beta\beta} \rangle$. That is how the upper region of the plot could be excluded by $0\nu\beta\beta$ -experiments.

⁴The confidence level (C.L.) states the probability for the true value of an observable to lie within certain confidence bounds.

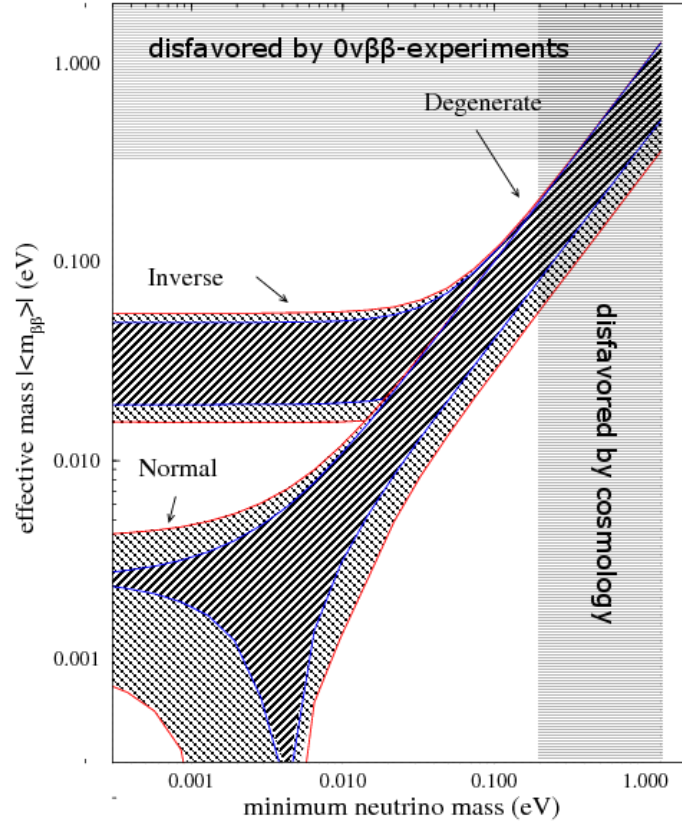


Figure 2.2: Effective Majorana mass $\langle m_{\beta\beta} \rangle$ depending on the lightest neutrino mass, adapted from [MV04]. One band appears for each mass hierarchy. The width is determined by the unknown Majorana phases (stripes region). The broadening from the 1σ uncertainties on the oscillation parameters is indicated by the cross hatched region.

2.3 Double Beta Decay

2.3.1 Derivation and Decay Modes

A nucleus has a lower mass than the sum of its constituents. The difference is called binding energy E_B or mass excess. E_B can be calculated by the semi-empirical mass formula, which was postulated by C.F. von Weizsäcker in 1935 and further developed by H. Bethe in 1936 [vW35, BB36]. E_B is calculated from the number of protons Z and the number of nucleons A in the nucleus:

$$E_B(A, Z) = a_V A - a_S A^{2/3} - a_C \frac{Z^2}{A^{1/3}} - a_A \frac{(A - 2Z)^2}{A} + \delta \cdot \frac{a_P}{A^{1/2}} \quad (2.15)$$

The five terms are the energetic contributions of volume, surface, Coulomb forces, asymmetry in the proton-neutron ratio and the pairing, adjusted by the constants a_V , a_S , a_C , a_A and a_P , respectively. The latter accounts for the fact that E_B complies with the numbers of neutrons and protons to be even or odd. According to this,

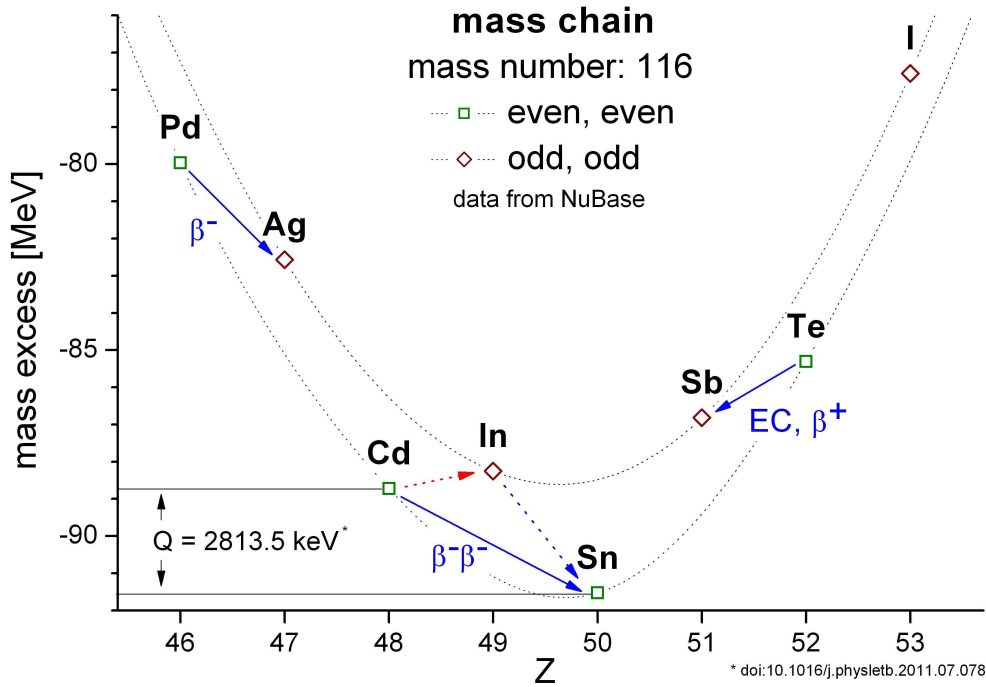


Figure 2.3: Mass excess for $A = 116$ [JT]. B_E splits up into two parabolae for even-even and odd-odd nuclei. A decay is only possible if the daughter nuclide has a higher mass excess than its mother.

$$\delta = \begin{cases} +1 & \text{for even-even nuclei,} \\ 0 & \text{for even-odd or odd-even nuclei,} \\ -1 & \text{for odd-odd nuclei.} \end{cases} \quad (2.16)$$

Considering only isobars, $E_B(A, Z)$ has a parabolic shape for nuclei with odd A . For even A , the function splits up into two parabolae due to the different pairing terms for even-even and odd-odd combinations.

Figure 2.3 shows $E_B(A, Z)$ for the case $A = 116$. The odd-odd nuclides are lined up on the upper parabola, the even-even nuclides make up the lower one. Due to energy conservation, a decay is only possible if the daughter nuclide has a higher mass excess than its mother, or to put it simple, if it is lighter. A β^- decay of a nucleus ${}^A_Z\text{X}$ as per



is allowed for Pd into Ag, to stick to the example of $A = 116$ nuclei. For the transition Te into Sb, besides the β^+ decay also an electron capture process (EC) is possible:



While a decay from Cd into In is energetically suppressed, it is thinkable for Cd to skip the

indium state and transition directly into Sn via two simultaneous β^- decays. The so described double beta minus ($\beta^-\beta^-$) decay accompanied by two antineutrinos as per



has experimentally been observed. Current experiments also search for the variants ($\beta^+\beta^+$), (β^+/EC) and (EC/EC) but have not yet been observed. In total 36 isotopes are expected to undergo the $2\nu\beta\beta$ decay [Gro14]. Due to the higher order of the effect, the process is very rare. The calculated and observed half-lives are in the order of 10^{19} years and higher.

In 1939, shortly after Majorana's postulation of two-component neutrinos, G. Racah and W.H. Furry discussed another double beta decay mode [Rac37, Fur39]:



Here, no neutrinos feature in the outcome of the process anymore. One plausible way to explain the absence of neutrinos is the Racah sequence



A right-handed antineutrino is created virtually in a β^- process and instantaneously absorbed as a left-handed neutrino by the intermediate nuclide Y. Hereby a second decay is induced and no neutrino remains in the final state. The conditions for this to happen become obvious:

- (i) To induce the second step, the neutrino has to be its own antiparticle.
- (ii) To satisfy the V-A theory, the neutrino has to undergo a helicity flip. This is only possible for massive particles, and therefore $m_{\nu_e} \neq 0$.
- (iii) The total lepton number⁵ is not a conserved quantity.

It is clear from neutrino oscillations that (ii) is fulfilled. An alternative to (ii) would be unprecedented right-handed weak currents [SH93].

Apart from the Racah sequence depicted in equation (2.22), several other processes can lead to a neutrinoless final state. J. Schlechter and J.W.F. Valle showed in [SV82] that in case of $0\nu\beta\beta$ decay the neutrino must have a non-vanishing Majorana mass, no matter the underlying mechanism. This is illustrated schematically in figure 2.4. The two d quarks that transition into u quarks within the nucleons are somehow coupled to the emitted electrons. The fact that the exact kind of coupling is unknown is represented by the black box. According to Schlechter and Valle, at some loop level within the black box a neutrino-antineutrino transition as described by the Majorana mass term in equation (2.9) can occur [Zub12]. Consequently, another name for this argumentation is Black Box theorem.

⁵Lepton numbers $L_i = 1$ ($L_i = -1$) are assigned to leptons (antileptons) from generation i . The L_i are conserved in every SM process. Neutrino oscillations violate this law, although the total lepton number $L = \sum_i L_i$ is conserved anyway.

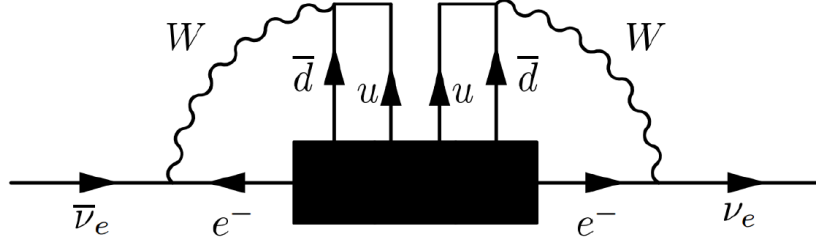


Figure 2.4: Schematic view of the Schlechter-Valle theorem [SV82]. The two d quarks that transition into u quarks within the nucleons are somehow coupled to the emitted electrons. The fact that the exact kind of coupling is unknown is represented by the black box. At some loop level within the black box a neutrino-antineutrino transition as described by the Majorana mass term can occur.

2.3.2 Decay Rates

A positive result in the search for $0\nu\beta\beta$ decay would prove that neutrinos are Majorana particles. Unfortunately, a long half-life causes the experimental realization to be challenging. The decay rate can be derived from Fermi's golden rule⁶. For the neutrino-accompanied case it is given by

$$\left(T_{\frac{1}{2}}^{2\nu}\right)^{-1} = G^{2\nu}(Q, Z) \left| \mathcal{M}_{GT}^{2\nu} + \frac{g_V^2}{g_A^2} \mathcal{M}_F^{2\nu} \right|^2 \propto Q^{11} \quad , \quad (2.23)$$

with $G^{2\nu}$ denoting the phase space integral, and $\mathcal{M}_{GT}^{2\nu}$ and $\mathcal{M}_F^{2\nu}$ being the matrix elements for Gamow-Teller and Fermi transitions, respectively. g_V and g_A are coupling constants originating from the V-A theory. Q , in the following referred to as Q-value, is the energy released in a nuclear transition.

The decay rate for $0\nu\beta\beta$ decay reads

$$\begin{aligned} \left(T_{\frac{1}{2}}^{0\nu}\right)^{-1} &= G^{0\nu}(Q, Z) \left| \mathcal{M}_{GT}^{0\nu} - \mathcal{M}_F^{0\nu} \right|^2 \left(\frac{\langle m_{\beta\beta} \rangle}{m_e} \right)^2 \\ &= G^{0\nu}(Q, Z) \left| \mathcal{M}^{0\nu} \right|^2 \left(\frac{\langle m_{\beta\beta} \rangle}{m_e} \right)^2 \propto Q^5 \quad , \quad \text{with } \mathcal{M}^{0\nu} := \mathcal{M}_{GT}^{0\nu} - \mathcal{M}_F^{0\nu} \quad . \end{aligned} \quad (2.24)$$

Besides the electron mass m_e also the effective Majorana mass $\langle m_{\beta\beta} \rangle$ controls the rate. A measurement of the half-life $T_{\frac{1}{2}}^{0\nu}$ would therefore help to determine $\langle m_{\beta\beta} \rangle$. Hence knowledge on the further parameters is required, but while $G^{0\nu}$ can be calculated precisely from Z and Q , the matrix elements are of great uncertainty. Their values depend on the nuclear model parameters and also on the calculation frameworks. The need for helicities to match diminishes the nuclear matrix elements significantly, so that $0\nu\beta\beta$ half-lives exceed the corresponding values for the neutrino accompanied case by several orders of magnitude. An overview on current $\mathcal{M}^{0\nu}$ results

⁶See [Zub12] for derivation of the decay rates and their approximate dependence on the Q-value.

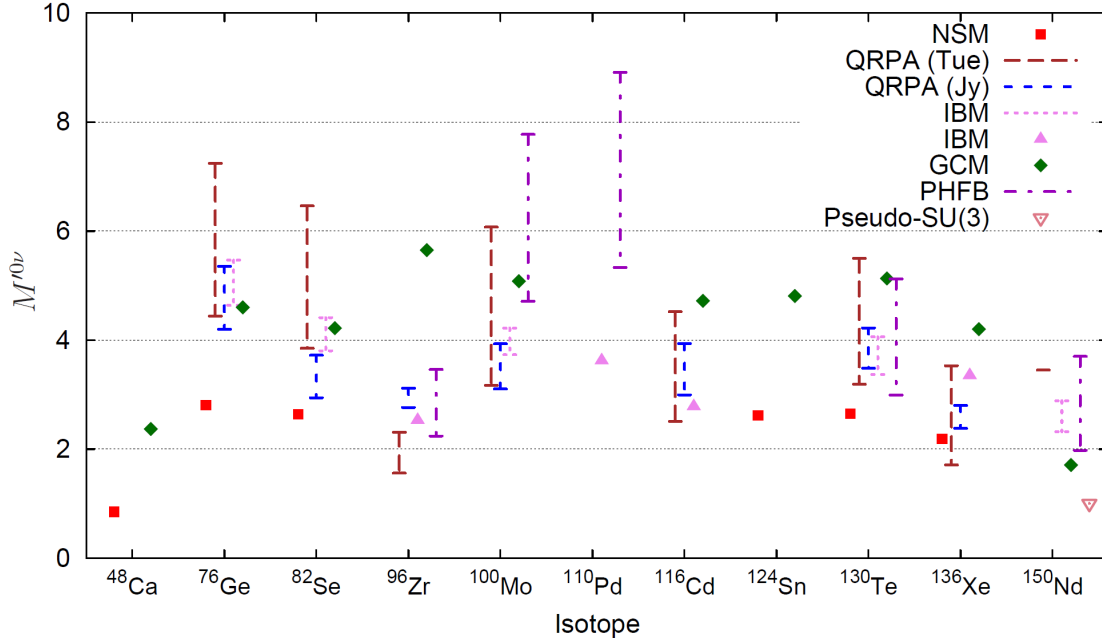


Figure 2.5: Overview on nuclear matrix elements $M^{0\nu}$ for $0\nu\beta\beta$ decay [D⁺11]. Values for several double beta isotopes were calculated in different frameworks.

Table 2.3: Phase space factor $Q^{0\nu}$ for several double beta isotopes [D⁺11].

| Isotope | $G^{0\nu}$ [10^{-14}yrs^{-1}] | Q [keV] |
|-------------------|--|-----------|
| ⁴⁸ Ca | 6.35 | 4273.7 |
| ⁷⁶ Ge | 0.623 | 2039.1 |
| ⁸² Se | 2.70 | 2995.5 |
| ⁹⁶ Zr | 5.63 | 3347.7 |
| ¹⁰⁰ Mo | 4.36 | 3035.0 |
| ¹¹⁰ Pd | 1.40 | 2004.0 |
| ¹¹⁶ Cd | 4.62 | 2809.1 |
| ¹²⁴ Sn | 2.55 | 2287.7 |
| ¹³⁰ Te | 4.09 | 2530.3 |
| ¹³⁶ Xe | 4.31 | 2461.9 |
| ¹⁵⁰ Nd | 19.2 | 3367.3 |

for selected double beta isotopes is given in figure 2.5. See table 2.3 for a list of $G^{0\nu}$ values.

2.3.3 Detection

$0\nu\beta\beta$ decay is a field of high scientific interest. Numerous experiments search for the decay with distinct approaches. The collaborations GERDA [A⁺04a] and COBRA [Zub01] both apply semiconductor detectors. The NEMO collaboration (also SuperNEMO) combines calorimeters with particle trackers. SNO+ [Che08] builds on a liquid scintillator, while CUORE [A⁺04b] uses cryogenic methods, just to name a few. They all have in common the search for one spectral feature.

In general β^- decay such as described by equation (2.17), the released energy is mainly distributed to the two emitted particles e^- and $\bar{\nu}_e$, thus leading to a continuous electron energy

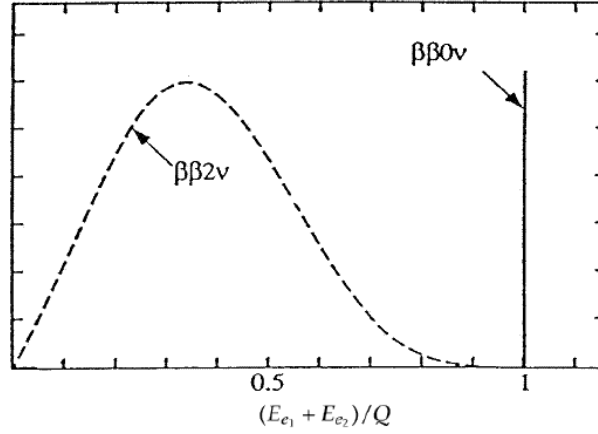


Figure 2.6: Summed electron spectra for $2\nu\beta\beta$ and $0\nu\beta\beta$ decay. In the first case, the Q -value is shared among two e^- and two $\bar{\nu}_e$, leading to a continuous shape. In the latter case, the absence of neutrinos causes the spectrum to be a discrete peak at Q . The height of the peak is strongly overstated. [htte].

Table 2.4: Current limits on half-lives for $0\nu\beta\beta$ -decay and effective Majorana masses [HM14]. Since the effective Majorana mass depends strongly on the choice of models for matrix element calculation, $\langle m_{\beta\beta} \rangle_1$ and $\langle m_{\beta\beta} \rangle_2$ denote a lower and an upper bound, respectively.

| Isotope | Experiment | $T_{\frac{1}{2}}^{0\nu}$ [10^{24} yr] | $\langle m_{\beta\beta} \rangle_1$ [eV] | $\langle m_{\beta\beta} \rangle_2$ [eV] |
|-------------------|-------------------|--|---|---|
| ^{76}Ge | Heidelberg-Moscow | 9.6 | 0.357 | 0.739 |
| | GERDA | 25 | 0.221 | 0.458 |
| ^{82}Se | NEMO-3 | 0.32 | 0.971 | 2.082 |
| ^{100}Mo | NEMO-3 | 1.0 | 0.473 | 0.923 |
| ^{130}Te | CUORICINO | 4.1 | 0.243 | 0.470 |
| ^{136}Xe | KamLAND-Zen | 26 | 0.115 | 0.221 |
| | EXO-200 | 11 | 0.177 | 0.339 |

spectrum – the very feature that caused W. Pauli to speculate about the existence of neutrinos in 1930. Given a $2\nu\beta\beta$ decay (equation (2.20)), the Q -value is shared among the four emitted particles. As before, the neutrinos escape the detector and the detectable sum of the electron energies E_{e_1} and E_{e_2} originates from a continuous spectrum as depicted in figure 2.6. If no neutrinos come out, as it is the case as in equation (2.21), the whole energy is left to the electrons, causing the summed electron spectrum to resemble a discrete peak at the Q -value. The peak is what $0\nu\beta\beta$ experiments are after, whereas the height of the line is heavily overstated in figure 2.6 due to the difference in half-life.

Unlike for $2\nu\beta\beta$ decay, no $0\nu\beta\beta$ decay has been found yet. Previously reported observations in ^{76}Ge by the Heidelberg-Moscow collaboration [KKK06] were ruled out by latest GERDA measurements [A⁺13]. Upper limits for $0\nu\beta\beta$ decay, though depending strongly on calculation frameworks of the nuclear matrix elements, range up to 10^{25} years [HM14]. The corresponding effective Majorana masses come close to the upper edge of the inverted hierarchy band (see figure 2.2). Current values for half-lives and effective Majorana masses are listed in table 2.4. COBRA half-lives from a demonstrator setup range currently at the order of 10^{21} years, see also table 3.3 in the next chapter.

Chapter 3

The COBRA Experiment

Among the $0\nu\beta\beta$ community, the COBRA experiment has the distinction of being the only aspirant to search for the decay in CdZnTe – and having therefore access to the $0\nu\beta\beta$ decay half-life of the isotope ^{116}Cd . This chapter explains the idea behind the approach and describes in detail the demonstrator setup that is currently operated in the underground laboratories at LNGS¹. The chapter closes with an outlook on a potential large scale setup.

3.1 Idea and Concept

The next-generation experiment COBRA was originally proposed by K. Zuber in 2001 [Zub01]. The name stands for "CdZnTe **0** Neutrino Double **B**eta **R**esearch **A**pparatus" and as indicated in the acronym, the intention is to use CdZnTe (or simply CZT) semiconductor detectors to search for $0\nu\beta\beta$ decay. Containing itself a total of nine double beta candidates, the detector material serves as its own source. The big benefit is a high detection efficiency. All candidate isotopes, their Q-values, natural abundances, and predicted decay modes are listed in table 3.1.

Since the Q-value of the decaying isotope has a significant impact on its decay half-life (as stated in section 2.3.2), the isotopes ^{130}Te , ^{106}Cd and ^{116}Cd are of special interest for COBRA.

Table 3.1: List of $0\nu\beta\beta$ candidate isotopes contained in CZT. Values taken from [R⁺11] except for ^{116}Cd and ^{130}Te , where Q is taken from [S⁺90].

| Isotope | Decay Mode | Q [keV] | Nat. Abundance [%] |
|-------------------|--|-----------|--------------------|
| ^{64}Zn | $\beta^+/\text{EC}, \text{EC}/\text{EC}$ | 1096 | 48.6 |
| ^{70}Zn | $\beta^-\beta^-$ | 1001 | 0.62 |
| ^{106}Cd | $\beta^+\beta^+, \beta^+/\text{EC}, \text{EC}/\text{EC}$ | 2771 | 1.21 |
| ^{108}Cd | EC/EC | 231 | 0.9 |
| ^{114}Cd | $\beta^-\beta^-$ | 534 | 28.7 |
| ^{116}Cd | $\beta^-\beta^-$ | 2814 | 7.5 |
| ^{120}Te | $\beta^+/\text{EC}, \text{EC}/\text{EC}$ | 1722 | 0.1 |
| ^{128}Te | $\beta^-\beta^-$ | 868 | 31.7 |
| ^{130}Te | $\beta^-\beta^-$ | 2527 | 33.8 |

¹Laboratori Nazionali del Gran Sasso

Table 3.2: Material properties of CZT in comparison with CdTe, Ge, and Si [eV 13].

| Material | Cd _{0.9} Zn _{0.1} Te | CdTe | Ge | Si |
|---|--|----------------------|-------------|--------------------|
| Atomic number Z | 48, 30, 52 | 48, 52 | 32 | 14 |
| Density ρ [g/cm ³] | 5.78 | 5.85 | 5.33 | 2.33 |
| Band gap E_g [eV] | 1.572 | 1.5 | 0.67 | 1.12 |
| Ionization energy E_{ion} [eV] | 4.64 | 4.43 | 2.95 | 3.62 |
| Relative permittivity ϵ_r | 10.9 | 11 | 16 | 11.7 |
| Electron mobility μ_e [cm ² /(Vs)] | 1000 | 1100 | 3900 | 1400 |
| Electron lifetime τ_e [s] | 3×10^{-6} | 3×10^{-6} | $> 10^{-3}$ | $> 10^{-3}$ |
| Hole mobility μ_h [cm ² /(Vs)] | 50 - 80 | 100 | 1900 | 480 |
| Hole lifetime τ_h [s] | 310^{-6} | 2×10^{-6} | 10^{-3} | 2×10^{-3} |
| $(\mu\tau)_e$ [cm ² /V] | $(3 - 10) \times 10^{-3}$ | 3.3×10^{-3} | > 1 | > 1 |
| $(\mu\tau)_h$ [cm ² /V] | 5×10^{-5} | 2×10^{-4} | > 1 | ≈ 1 |

The most promising candidate is ¹¹⁶Cd, whose Q-value exceeds the prominent gamma line from natural ²⁰⁸Tl at 2614 MeV. ¹³⁰Te features a high natural abundance in favor of its detectability while ¹⁰⁶Cd gives access to the $\beta^+\beta^+$ decay channel.

The working principle of a semiconductor detector can be condensed as follows: An electromagnetic interacting particle traversing the semiconducting material causes the excitation of electrons from the valence into the conduction band. The generated mobile charge carriers, namely electrons and holes, get separated by an external electric field and are collected at the respective electrodes. The amount of charge carriers can be measured and is directly proportional to the energy previously deposited in the crystal. The total kinetic energy of a particle can be determined only if it is stopped within the fiducial semiconductor volume.

Comparable experiments like GERDA use germanium detectors. Material parameters for Ge and CdZnTe, as well as for CdTe and Si, are given in table 3.2. As compared to Ge, CdTe and CdZnTe show some advantages with regard to detection qualities. While Ge detectors need to be cooled to liquid nitrogen temperatures, the large band gap E_g of CdTe allows for an operation at room temperature, since fewer valence electrons get into the conduction band due to thermal excitation. At the same time, E_g adversely affects the energy resolution, since in average more energy E_{ion} is needed to create an electron-hole pair. It turned out that the admixture of a small amount of Zn enlarges E_g even more. CdZnTe detectors also benefit from the relatively high average atomic number and density, causing ionizing particles to be stopped fast.

The drift mobility μ and lifetime τ of the charge carriers are essential transport properties for semiconductor detectors as they directly affect the energy resolution. Their product $\mu\tau$ is hence an important measure for the detector performance. A further look at table 3.2 shows that $\mu\tau$ is quite low for CdZnTe, especially for holes. At COBRA, the lack of hole information is compensated by the use of coplanar grid detectors (CPG), whose working principle is depicted in detail in chapter 4.

CdZnTe is a three-component II-VI semiconductor with the elements Cd and Zn from the second and Te from the sixth main group. Although the detectors are commercially available,

their size is limited due to the complex manufacturing processes required. Currently available monolithic crystals do not go beyond a couple of cubic centimeters. Several thousand crystals are needed to reach the requisite fiducial mass of several hundred kilograms. The need for this huge amount of detectors is turned into a strength since the arrangement in a three-dimensional array allows for the spatially resolved reconstruction of timing coincidences.

Generally speaking, complementary approaches are, as in any scientific discipline, an important instrument to obtain evident results. It is thus highly desirable to search for $0\nu\beta\beta$ decay with different techniques and materials, especially as the calculation of the exact nuclear matrix elements proves to be rather difficult, so that the determination of the effective Majorana mass from the decay half-life would not be straightforward. COBRA should therefore not only be understood as competitive but in particular as a crucial complement to further established approaches.

3.2 Background Sources

With half-lives in the order of 10^{20} years, the $2\nu\beta\beta$ decay ranges among the most seldom natural processes ever observed. Half-lives for the neutrinoless variety are expected to exceed those values by several orders of magnitude, making background an essential experimental issue. In order to recognize significant spectral features induced by the sought decay, the experimentalist must be aware of any type of background. Only then he might be able to studiously shield and individually identify unwanted events.

3.2.1 Primordial Background

Background resulting from the natural decay chains and ^{40}K decay is generally classified as primordial background. Certain decay stages in the thorium series, originating from ^{232}Th , and the uranium series, leading back to ^{238}U , are relevant to COBRA since they might deposit energy in the crucial energy regions. In case of ^{116}Cd , the region of interest (ROI) is situated around 2.8 MeV. As depicted in appendix A, where an overview on both series is given, mostly alphas range within or above the ROI, besides one β -decay and a few γ -transitions.

Treacherous links in both chains are radon stages. As a noble gas, radon can easily diffuse from out of the surrounding rock and materials into the immediate detector environment. There it is likely to be attracted by statically charged surfaces and the high detector potentials. From the thorium series, this is ^{220}Rn with a half-life of one brief minute, while ^{222}Rn from the uranium series is even more dangerous with nearly four days half-life. All following α -decays as well as the β -decay from ^{214}Bi into ^{214}Po must be taken into account as potential background. The latter goes along with γ -emissions with energies up to 3.27 MeV, including several γ -lines in the ROI.

3.2.2 Cosmogenic Background

Although just a small fraction of the cosmic radiation reaches the experiment at its underground location at LNGS, cosmogenic background has to be considered carefully. The hadronic component is absorbed by the rock material. Although reduced by a factor of 10^6 , cosmic muons can deposit energy in the detectors or produce hadronic showers in their environment. Furthermore, detectors and shielding material were exposed to cosmogenic hadrons previously during manufacturing, shipping and storage at the earth's surface. Accordingly, radionuclides are produced and cause intrinsic contamination.

3.2.3 Neutrons

Due to the absence of electric charge, neutrons can easily diffuse from their point of origin through air and solids if no adequate shielding is present, and in this way they are invisible to the detectors as long as they do not interact. Neutrons in the underground laboratory arise mostly from natural decay processes. They are emitted during spontaneous fissions and (α, n) reactions with light nuclei such as lithium, fluorine and boron, whereas the requisite alphas themselves come from natural decays. Another neutron source are cosmogenic hadron showers as described above.

Such neutrons typically have energies of several MeV, not enough to leave signals near the ROI by elastic scattering processes, as has been explicitly demonstrated in [Tim15]. Much more dangerous in terms of energy deposition are absorption processes, especially the reaction $^{113}\text{Cd}(n, \gamma)^{114}\text{Cd}$. A neutron is captured by a ^{113}Cd nucleus, leaving an excited ^{114}Cd nucleus that within nanoseconds emits around 9 MeV of energy in a γ -cascade. The combination of a high total cross section ($> 10^4$ bn for thermal neutrons) and the high abundance of ^{113}Cd (12 % for natural cadmium) makes it necessary to watch out for such processes. In fact it could be shown that by considering this very reaction the thermal neutron flux inside the COBRA shielding can be measured during operation with the detectors themselves [Reb13].

The surface contamination as a consequence of radon diffusion, as well as the external background by muons and neutrons, and the intrinsic contamination of detector holders, passivation lacquer surrounding the crystals, electronics and shielding in a large-scale COBRA setup are discussed by in [Hei14], based on extensive Monte Carlo simulations. The study shows that the expected background is clearly dominated by 99 % α -particles. The contributions of single particle types to the total background is depicted in figure 3.1. After applying all actual data cuts, the impact of alphas becomes even more apparent.

The alpha domination of the background has also been confirmed from the experimental side. As Fritts *et al.* reported in [FT⁺14], a cut, developed to remove surface events, eliminates 75 % of all signals. As this value matches the reported cut efficiency, one can conclude that surface events make up most of the background. These arise from radon decay products, which in the considered energy ranges emit mainly alphas.

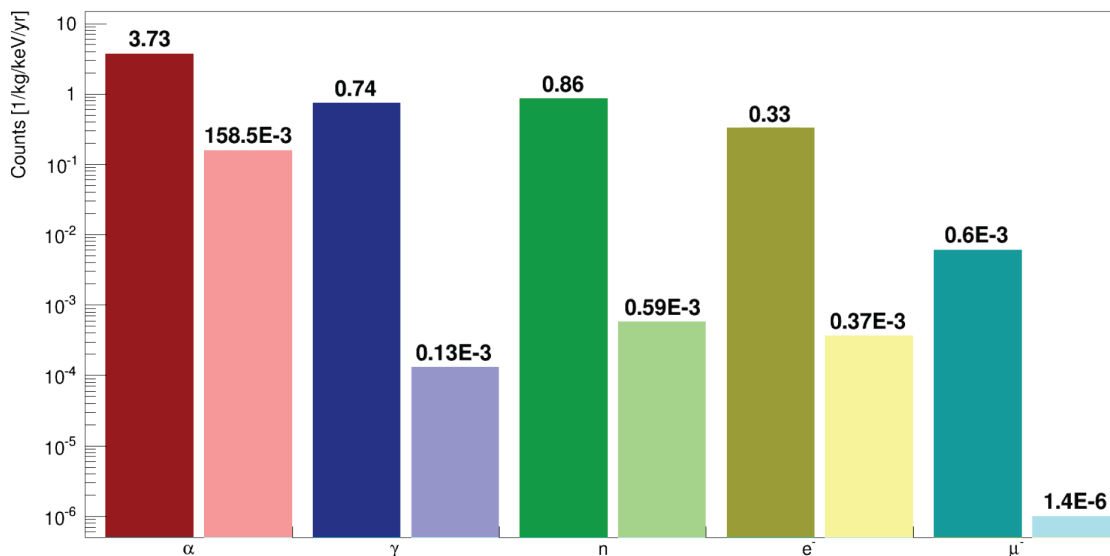


Figure 3.1: Contributions of different particle types to the total background, based on Monte Carlo studies [Hei14]. The darker bars refer to background rates before, the lighter bars to background rates after applied data cuts.

3.2.4 $2\nu\beta\beta$ Decay

As an unavoidable side effect, $0\nu\beta\beta$ decay will naturally be accompanied by the much more frequent $2\nu\beta\beta$ decay. The $0\nu\beta\beta$ peak in the energy spectrum at the Q-value of the decaying isotope will be smeared due to a limited energy resolution of the detector, the same goes for events from the $2\nu\beta\beta$ continuum. Even if all other background can be held at an acceptable low level, the energy resolution is the determining quality to decide whether both spectra might be separated.

3.3 Demonstrator Setup

Currently, a COBRA demonstrator setup is taking data to test both the long term stability of the detectors and the shielding concept and to analyze events under ultra low background conditions. An overview is given here, for further technical details see [T⁺15] and [Sch11].

The demonstrator is situated in the neighborhood of other $0\nu\beta\beta$ experiments like GERDA and CUORE at the LNGS underground facilities in Italy. Since September 2011, four layers with 4×4 CZT crystals each have been installed successively, completing the $4 \times 4 \times 4$ detector array in November 2013. The crystals of each layer are embedded in a holder made of Delrin, see figure 3.2. The 64 CPG detectors each have a volume of $(1 \times 1 \times 1) \text{ cm}^3$ and a mass of 5.8 grams, adding up to ca. 380 grams in total. In order to prevent surface currents, the lateral crystal surfaces are covered with Glyptol lacquer.

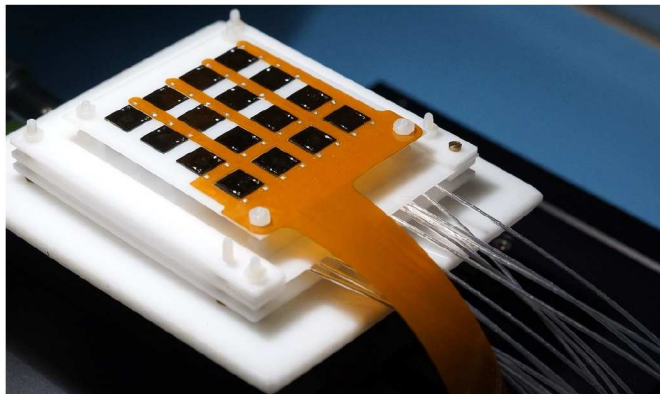


Figure 3.2: Delrin holder with 4×4 CZT crystals [T⁺15]. Four such layers are placed on top of one another at the COBRA demonstrator.

3.3.1 Shielding

The ultra low count rate character of COBRA demands for ultra low background conditions. 1400 meters of rock material cover the location at LNGS and serve as a natural shield against cosmic rays, corresponding to 3200 meters water equivalent. Apart from that, the experiment is coated by a multilayer shielding [Mün07, Hei14].

The shielding inside the laboratory hut is depicted schematically in figure 3.3. Going from outside to inside, the outermost layer is a wall of 7 cm thick boron-loaded polyethylene (PE). The high amount of hydrogen inside the material is suitable for the moderation of fast neutrons. At thermal energies, these are easily captured via $^{10}\text{B}(n,\alpha)^7\text{Li}$ reactions. The emitted alphas are instantly stopped in the PE, gammas from de-excitation will not overcome the inner lead castle.

The subsequent layer is a box of iron plates to shield detectors, cables and preamplifiers from electromagnetic interferences (EMI) which can easily induce physical events or disturb the signals. To feed the cables through the EMI box, they are laid through a chute filled with copper granulate to prevent the cables from importing EMI from outside the box.

The inner shielding complex begins with a radon-tight polycarbonate box. In addition to this, the inside of the box is constantly flushed with nitrogen gas to clean the inner atmosphere from radionuclides, especially radon.

A $(60 \times 60 \times 60)$ cm³ castle of lead bricks and copper surrounds the innermost part of the setup. Due to its high density, lead is a good γ -absorber. The outer standard lead bricks are followed by a layer of low activity lead with an activity of less than 3 Bq per kg w.r.t. ^{210}Pb . As high purity goes along with high costs, a copper layer of very high radiochemical purity follows the lead bricks in order to catch intrinsic radiation arising from the lead. Having a smaller density, its qualities to absorb gammas do not play in the same league as lead but are sufficient, though.

A copper box containing the detectors builds the heart of the experiment.

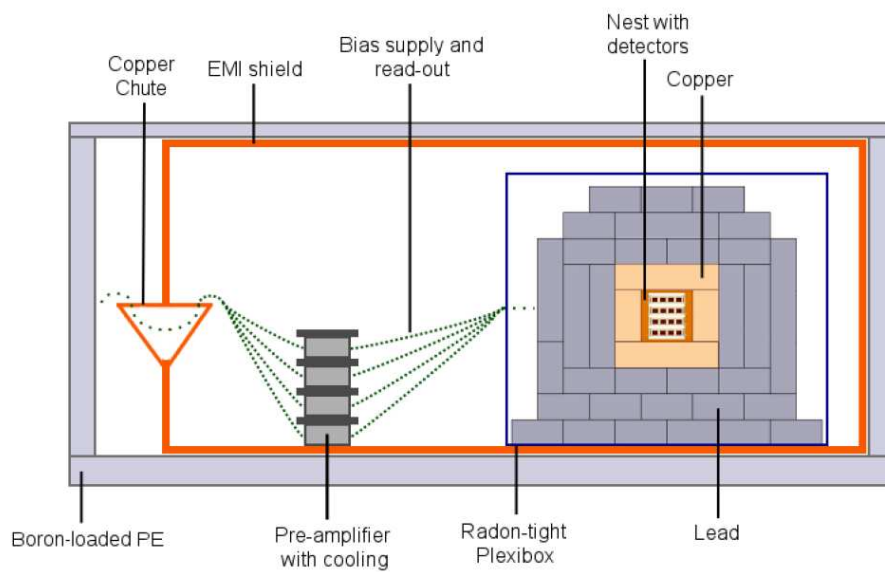


Figure 3.3: Scheme of the current demonstrator shielding at LNGS [Hei14]. Boron-loaded PE serves as a shield against neutrons, followed by iron sheets against EMI. The inner shielding consists of a radon-tight polycarbonate box which is constantly flushed with gaseous nitrogen. Lead and copper protect the detectors from γ -radiation.

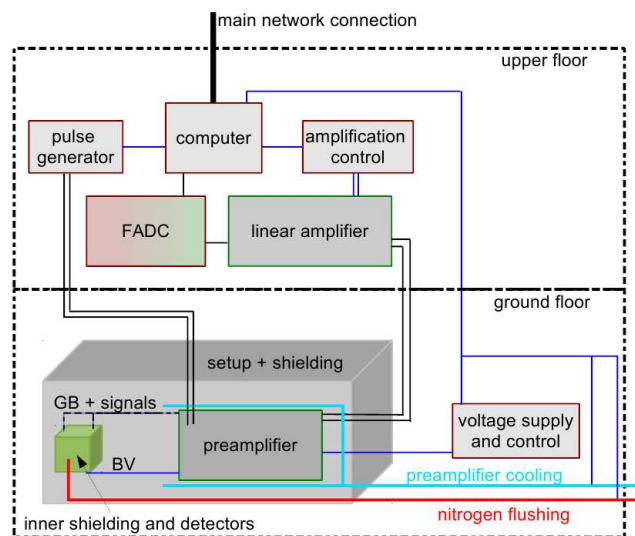


Figure 3.4: DAQ chain of the COBRA demonstrator at LNGS [T⁺15].

3.3.2 DAQ Chain

The data acquisition (DAQ) chain was designed to meet the special needs of the COBRA demonstrator. One objective was to build a fully remotely-controllable readout system. A schematic view of its main components can be found in figure 3.4.

Detector Voltage Supply

To run a CPG detector, the cathode has to be held at high negative potential (typically about -1 kV), while its two anode grids are operated at low potentials with a bias voltage (typically between 50 V and 150 V) between the grids (see section 4.1.2). The ideal high bias voltage (HV or BV) and grid bias (GB) for each CPG detector were determined previously. The individual voltage supply is controlled by a computer and forwarded to the detectors via the preamplifier boxes.

Preamplifier Boxes

The preamplifier boxes are custom-made devices that were incorporated into the multilayer shielding in order to minimize the signal way from the detectors to the preamplifiers and to shield them as good as possible from EMI. The 16 crystals in each of the four detector layers share one preamplifier box. Their signals are delivered to the boxes via Kapton ribbon cables. The conversion from charge signals into voltage signals is done by the charge sensitive preamplifier modules *Cremat CR110* [hp]. Afterwards, they are transformed into differential signals to prevent signal distortions due to electromagnetic interferences, noise and crosstalk on the long way (several m) to the linear amplifiers. In figure 3.4 the differential signal transmission is depicted by a double line.

The preamplifier boxes are being cooled by metal plates that are continuously streamed with water from inside, since the heat produced by the devices would negatively affect the signal quality. A cool detector surrounding also facilitates the energy resolution of events with energies below 100 keV.

Linear Amplifiers

Due to the strong heat emission of certain devices, a part of the readout chain was outsourced to another level of the laboratory hut. For the signal transmission to the main amplifier boxes on the upper floor, standard category 6 network cables are used. The boxes are custom-designed as well, linearly amplifying the differential input in two steps by making use of *AD8369* digitally controlled variable gain amplifiers [httg], followed by an *AD8130* differential receiver [httf]. The latter reconverts the signal to single-ended output. It is possible to vary the gain between 0.5 and 89 to ideally match the FADC input range. One main amplifier box is constructed to process up to 8 signals and therefore capable of covering 4 CPG detectors.

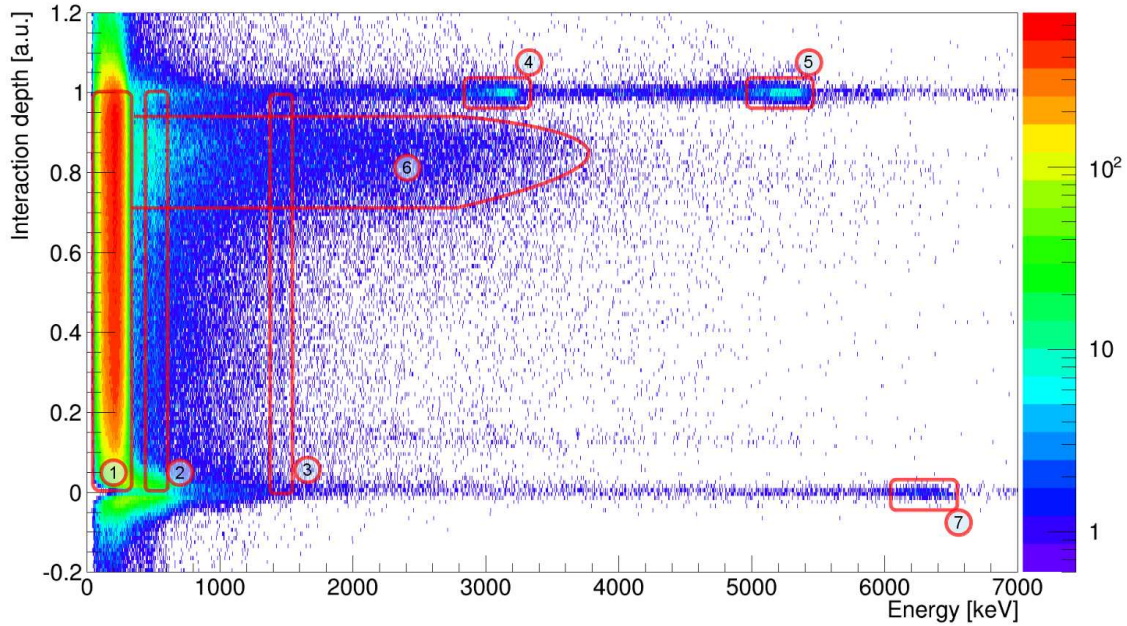


Figure 3.5: Interaction depth plotted against energy deposition for LNGS 2011 - 2014 data [Old15]. Prominent background features are labelled and numbered w.r.t. their origin: (1) β decay of ^{113}Cd , (2) γ -line from e^+e^- -annihilation, (3) γ -line from ^{40}K EDC, (4) α decay of ^{190}Pt , (5) α decay of ^{210}Po , (6) hump region most likely due to radon progenies on the Delrin holder structure.

FADCs

Up to this point, the signal is fully analog. The digitization is done by commercial *Struck SIS330x* fast analog-to-digital converters (FADCs). The 8 output signals of one main amplifier box are fed into the 8 FADC input channels. Here they get sampled with a rate of 100 MHz and 10 bit resolution, delivering $10.24 \mu\text{s}$ long pulses to the computer for storage. As the maximum length of physically induced pulses is approximately $1 \mu\text{s}$, enough pre- and post-baseline information is stored for analytic purposes.

Pulse Generator

For the synchronization of the 16 FADCs and to test the DAQ chain independently of the hard-to-access detectors, a *Berkeley Nucleonics PB-5* pulse generator has been installed. It can directly inject well-defined pulses to each of the 128 preamplifiers, getting there differentially and being transformed into single-ended signals inside the preamplifier box. Pulses from the generator are flagged as such in the data in order to separate them from detector pulses retrospectively.

3.3.3 Current Status

Up to date, the COBRA demonstrator has collected an exposure of roughly 300 kg-days. Regular calibration runs with ^{22}Na and ^{228}Th make a monitoring of the detector performances possible. The average energy resolution of the operating detectors is 1.5 % at the Q-value of ^{116}Cd .

CPG detectors allow also for the reconstruction of the interaction depth z , as will be explained in more detail in section 4.1.3. In figure 3.5 the interaction depth is plotted against the deposited energy for the events collected between 2011 - 2014². The depth is given in relative units, 1 denoting the cathode and 0 the anode level of the detector. For events outside the crystal region the reconstruction algorithm performed incorrectly. In this representation a couple of features are visible that can be linked to background sources discussed beforehand. The most prominent plot domain (1) originates from ^{113}Cd , which is naturally abundant in the detector material and decays into ^{113}In in a β^- process, depositing up to 316 keV of energy. The process is equally distributed throughout the entire detector and therefore appears as a vertical line in the plot. This intrinsic source cannot be shielded, instead it offers a good opportunity to continuously investigate the performance of the detectors. Gehre *et al.* published results of a long-term study in which they report excellent results for CZT operation in terms of detector performance and stability [G⁺15]. They can claim to build on the longest ever performed CZT measurement under low background conditions.

Further vertical lines in the plot arise at 511 keV from e^+e^- -annihilations (2) and at 1460.8 keV from electron capture (EC) of ^{40}K (3). Horizontal structures appear in case of locally dependent contaminations like e.g. radionuclear deposits on the anode and cathode side of the detector. This holds for the long living ^{210}Po , which is part of the uranium series and decays into ^{206}Pb under emission of a 5305 keV α (5). The cathode blob around 3249 keV (4) is due to the α decay of ^{190}Pt into ^{186}Os , since platinum is part of the cathode material. The ^{190}Pt decay is also visible at the anode side (7), here as a reconstruction artefact at twice the Q-value. A wrong energy reconstruction can happen near the anodes, so that data from this region has to be treated carefully in the further course of the analysis. The same applies to the region between 0.7 and 1.0 (6), where many events are located whose origin could not definitely be assigned yet, although radon progenies on the Delrin holder structure are under suspicion.

One way to avoid background from surfaces would be the CZT operation in a liquid scintillator, which would serve as an active veto. This option was successfully tested [Old15].

For the given reasons, neither the region near the anodes ($z < 0.2$) nor events from the highly contaminated cathode ($z > 0.97$) are taken into account in the later analysis. Furthermore it is possible to recognize events from the lateral crystal surfaces by regarding the pulse shapes [FT⁺14], see also section 4.1.2. Another pulse shape analysis allows for the identification of events, in which particles leave energy at several spots in the detector, so-called multi-site events (MSE) that lead to a wrong reconstruction of energy and interaction depth and are therefore unwanted [Zat14]. The impact of the lateral surface event (LSE) cut and the MSE cut are demonstrated in figure 3.6.

In the plot, the green bars mark the interesting energy regions for several $0\nu\beta\beta$ isotopes under investigation. On the basis of the current count rates, lower limits on half-lives for the $0\nu\beta\beta$ decay could be calculated, listed in table 3.3 [Q⁺15]. For ^{114}Cd , the COBRA demonstrator holds

²The plotted data was previously cleaned from unphysical events.

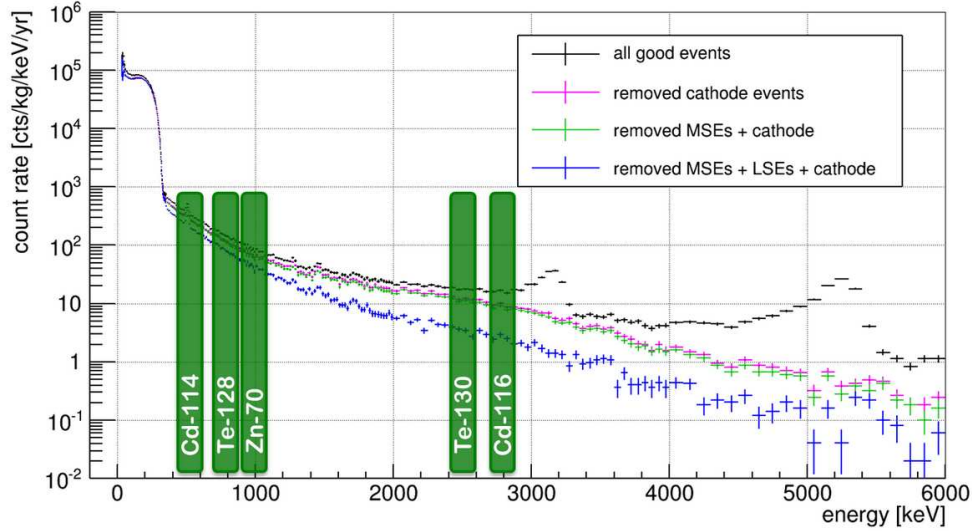


Figure 3.6: Count rate of the demonstrator with 218.9 kg-days exposure [SZ]. The rate is plotted for different combinations of applied cuts to show their impact on the data. Green bars mark the interesting energy regions for several $0\nu\beta\beta$ isotopes under investigation.

Table 3.3: Limits on half-lives $T_{1/2}$ for the $0\nu\beta\beta$ candidate isotopes under investigation, 90 % C.L. [Q⁺15].

| Isotope | $T_{1/2}$ [10^{21} y] |
|-------------------|--------------------------|
| ^{116}Cd | 1.4 |
| ^{114}Cd | 2.4 |
| ^{128}Te | 2.5 |
| ^{130}Te | 8.3 |
| ^{70}Zn | $6.0 \cdot 10^{-3}$ |

the world's best limit with a value of $2.4 \cdot 10^{21}$ years at 90 % confidence level.

3.4 Large-Scale Prospects

The development of a large-scale $0\nu\beta\beta$ experiment is driven by the half-life sensitivity $T_{1/2}^{0\nu}$ which is aimed at. It depends on the abundance a of the decaying isotope, the detection efficiency ϵ , the detector mass M , the runtime t of the experiment, the background index B , typically given in $\frac{\text{counts}}{\text{keV}\cdot\text{kg}\cdot\text{yr}}$, and the width ΔE of the search window, depending itself on the energy resolution of the detector [Sch13]:

$$T_{1/2}^{0\nu} \propto a \cdot \epsilon \sqrt{\frac{M \cdot t}{B \cdot \Delta E}} \quad (3.1)$$

In order to touch the upper bound of the inverse hierarchy band in the $\langle m_{\beta\beta} \rangle$ plot in figure 2.2, an effective Majorana mass bigger than 50 meV must be excluded. According to equation (2.24), this corresponds to a ^{116}Cd half-life of $T_{1/2}^{0\nu} = 2 \cdot 10^{26}$ years, if the required matrix elements are chosen favorably. While a , ϵ and ΔE are limited due to technical reasons, the increase of M causes high costs and a measuring time of more than 10 years is not desirable. The background

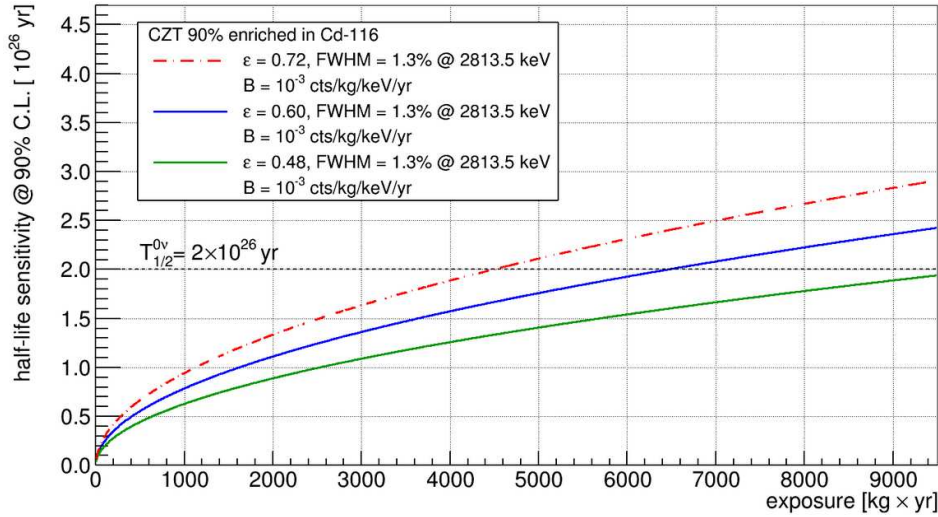


Figure 3.7: Half-life sensitivities of a possible large-scale COBRA experiment. The curves consider sensitivities for three different detection efficiencies, while ε is expected to lie between 0.6 and 0.72. A possible large-scale COBRA setup is planned to have 400 kg of detector mass and could achieve the aim of $T_{1/2}^{0\nu} = 2 \cdot 10^{26}$ years within a few years of runtime.

is the only parameter left and it is therefore worth to put some effort into its reduction. With a 90 % enrichment in ^{116}Cd of the cadmium portion and a realistic energy resolution of 1.3 %, it requires a background index of $10^{-3} \frac{\text{counts}}{\text{keV}\cdot\text{kg}\cdot\text{yr}}$ to reach the half-life sensitivities plotted against exposure in figure 3.7. The curves consider sensitivities for three different detection efficiencies, while a realistic value for ε is to find between 0.6 and 0.72, the blue and the red curve, respectively. A possible large-scale COBRA setup is planned to have 400 kg of detector mass and could achieve the aim of $T_{1/2}^{0\nu} = 2 \cdot 10^{26}$ years within a few years of runtime.

While the detectors installed in the demonstrator have a volume of $(1 \times 1 \times 1) \text{ cm}^3$, detectors of $(2 \times 2 \times 1.5) \text{ cm}^3$ are currently under investigation. Larger crystals are preferable due to their better surface to volume ratio. The tested grid design differs from the LNGS type. The anode surface is divided into four coplanar subgrids which are rotated against each other. See figure 3.8 for a photo of the large quad grid type next to other CPG detectors. Even though the channels for readout and voltage supply quadruple compared to a single CPG, the segmented grid structure opens up a variety of new analytical possibilities and is therefore closely examined in the laboratories at TU Dortmund and TU Dresden.

Current large-scale designs provide for a modular buildup based on 3×3 detector modules, eight of which form a module carrier. Eight such carriers placed next to each other make up one detector layer, and 20 layers would be operated one above the other. In total this makes 11 520 detector units with a mass of 415 kg in less than 1 m^3 volume.

In [Hei14] a multi-layer shielding for the described setup was developed with Monte Carlo methods. The total background due to natural and man-made radioactivity, cosmogenic background and thermal neutrons was conservatively estimated to lie below $54 \cdot 10^{-3} \frac{\text{counts}}{\text{keV}\cdot\text{kg}\cdot\text{yr}}$, already including the data cuts described in the previous section. To meet the required background index of $10^{-3} \frac{\text{counts}}{\text{keV}\cdot\text{kg}\cdot\text{yr}}$, further analysis cuts have to be developed.

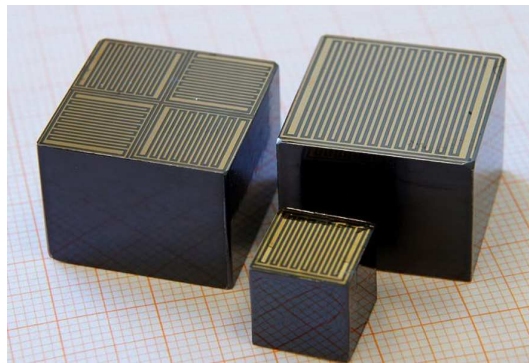


Figure 3.8: Three different types of CPG detectors. The small detector in front is adequate to the model currently used in the COBRA demonstrator at LNGS, behind it a simple upscaled version can be seen. Left in the picture a large detector with so-called quad grid structure is shown. The model is under discussion for a large-scale setup.

Chapter 4

Properties of CdZnTe CPG Detectors

A conventional semiconductor detector in its most simple realization consists of two electrodes with a semiconducting medium in between. As soon as ionizing radiation passes the medium, electron-hole pairs are created and move towards the electrodes. Here, they induce charge proportional to their number, i.e. to the energy deposited in the semiconductor, for the time of their drift. The height of one integrated electrode signal is therefore dependent on the point of primary interaction. To solve this issue, the signals of both anode and cathode are taken into account for energy reconstruction.

It is clear from this perspective that a full and accurate reconstruction of deposited energy and interaction depth is possible only if both electrons and holes head straight towards the respective electrode. But what if charge carriers get lost along their way? This is the case when electrons and holes recombine or get trapped in crystal defects. The carrier lifetime denotes an average value for a drifting period uninterrupted by trapping or recombination. A large outcome for the product of mobility μ and carrier lifetime τ is thus a hint for a good detector performance. $\mu\tau$ products for typical detector materials can be looked up in table 3.2. With $\mu\tau_e$ in the order of $10^{-3} \text{ cm}^2/\text{V}$, the value for electrons in CZT is by far lower than for germanium or silicon ($> 1 \text{ cm}^2/\text{V}$ each). For holes in CZT, the situation looks even worse with $\mu\tau_h \sim 10^{-5} \text{ cm}^2/\text{V}$. Since trapping is a statistical process, the deficit especially in hole statistics cannot be overridden by calibration adaptations and leads to a loss in energy resolution.

In 1994, P.N. Luke proposed a modification of the electrode structure to improve the CZT detector resolution [Luk94]. Similar to the function of a Frisch grid [Fri44], a further electrode is added at the anode side of the detector in order to do without the cathode signal. The two anodes intertwine in a comb-like structure, schematically visible in figure 4.1, giving the coplanar grid (CPG) detector type its name. See figure 3.8 for a realistic impression.

This chapter is dedicated to the functional principle and reconstruction methods of the CPG detectors currently in use for COBRA. Emphasis is put on the drift properties of the generated charge carriers in CZT, including trapping, electrostatic repulsion and thermal diffusion. The behavior of charge clouds is of great importance to the development of a detector simulation, see chapter 5, and particle discrimination based on pulse shape analysis, treated in chapter 6.

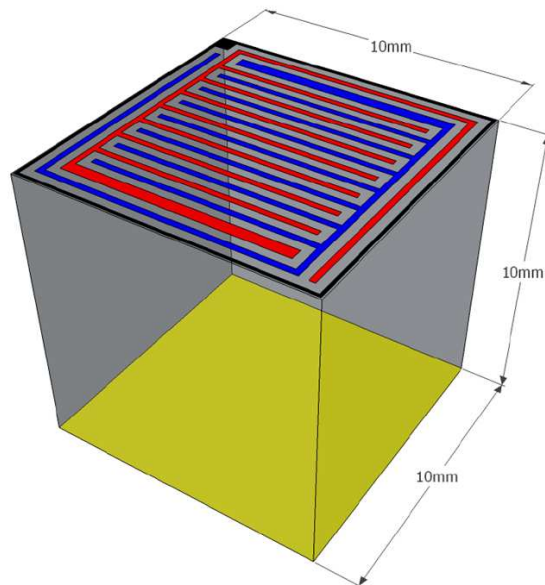


Figure 4.1: CPG detector scheme. On the upper side of the cubic crystal, two intertwining, comb-shaped anodes are mounted (colored blue and red). The cathode plane is at the bottom of the cube (yellow).

4.1 Signal Generation

4.1.1 Shockley-Ramo Theorem

In solids with a crystalline atomic structure, the electronic energy states overlap and form bands with forbidden gaps in between. Charge transport is only possible in bands which are not fully occupied. If the Fermi level lies within a gap, i.e. the total number of electrons in the crystal is adequate to exactly fill up a certain number of energy bands, the crystal is either classified as insulator or as semiconductor, depending on the size E_g of the gap between the uppermost occupied band, called valence band, and the next higher band, called conduction band, and thus on the possibility to reach electrical conductivity by the excitement of electrons¹. Otherwise, when the Fermi level lies inside an energy band, the material is a metal and has high conductivity.

Inside a semiconductor, an electron can easily be lifted from the valence to the conduction band, e.g. by thermal excitation or in scattering processes with ionizing particles. The band gap measures $E_g = 1.6 \text{ eV}$ in $\text{Cd}_{0.9}\text{Zn}_{0.1}\text{Te}$. The average energy needed to create an electron-hole pair is called ionization energy and is a little higher ($E_{ion} = 4.6 \text{ eV}$ for $\text{Cd}_{0.9}\text{Zn}_{0.1}\text{Te}$). The electron in the conduction band and the unoccupied state in the valence band, spoken of as hole, can subsequently migrate through the crystal.

An ionizing particle passing the detector leaves a trace of electron-hole pairs in the material. The number of generated charge carriers is proportional to the deposited energy. In the presence of an electric field \vec{E} , they start moving along the field lines, thus inducing a charge Q on the electrodes. The former method to calculate Q was to integrate the normal component of \vec{E} over

¹The boundary between insulator and semiconductor is not absolute, but typically set around $E_g = 5 \text{ eV}$.

the surface \vec{S} surrounding the electrode – for every point along the trajectory. In the late 1930s, W. Shockley and S. Ramo independently found that in a vacuum tube, Q can be gained much simpler, making use of a dimensionless weighting potential φ_w [Sho38, Ram39]. According to the Shockley-Ramo theorem, the charge Q induced at the electrode by a moving point charge q is proportional to the change in $\varphi_w(\vec{r})$ along the trajectory \vec{r} :

$$Q = -q\Delta\varphi_w(\vec{r}) \quad . \quad (4.1)$$

$\varphi_w(\vec{r})$ is the electric potential that would be present in the detector in case the respective electrode was held at unit potential, with all other electrodes grounded. Once $\varphi_w(\vec{r})$ is calculated for a certain electrode constellation, the signal shape and height can be predicted for every point of interaction and independently of the actual applied electrode potentials. In the later course it was proven that equation (4.1) holds not only for vacuum tubes but for a wide range of detectors, including the CPG type, even in the presence of space charge [Jen41, C⁺71]. A review of the Shockley-Ramo theorem, its proof, and several applications can be found in [He01].

4.1.2 Pulse Shapes

The anode structure in a CPG resembles two intertwining combs, represented in red and blue in figure 4.1. While a high negative potential (HV) of typically -1 kV is applied to the cathode, yellow in figure 4.1, one anode is operated on low negative potential of about -100 V, and the other on ground potential. In consequence, electrons moving in the crystal feel a constant electric field until they reach the region immediately in front of the anodes. The bias between the anode grids (grid bias, GB) causes the electrons to drift towards the grounded anode, which is therefore referred to as collecting anode (CA), in contrast to the biased non-collecting anode (NCA). What does this mean for the signal shapes?

Figure 4.2 shows the calculated weighting potentials for a CPG design across a plane through the center of the detector, perpendicular to the teeth of the anode combs. The coordinates are normalized to the detector dimensions. Along the drift direction z of the electrons, with the cathode placed at $z = 1$ and the anodes at $z = 0$, $\varphi_w(\vec{r})$ rises linearly throughout the bulk of the crystal with a slope of $\frac{1}{2}$, equally for both CA (a) and NCA signal (b). Near the anodes, $\varphi_w(\vec{r})$ splits up, inversely for CA and NCA. Guided by the electric field lines, the electrons will move to a CA strip, corresponding to an upward-bent CA signal and a downward-bent NCA signal.

Figure 4.3 (a) shows a typical CPG pulse. Time is displayed on the x-axis in units of FADC samples. The red and blue signals correspond to the CA and NCA, respectively. They start rising as soon as energy has been deposited in the crystal, around sample #550. Analogous to the electric field, the slope is constant and equal for both signals, just until the first drifting electrons enter the near-anode region, around sample #600, getting affected by the GB here. According to the weighting potential, the CA signal now bends up, and the NCA signal bends down instantly. The charge collection process is completed when the pulses reach the flat post-

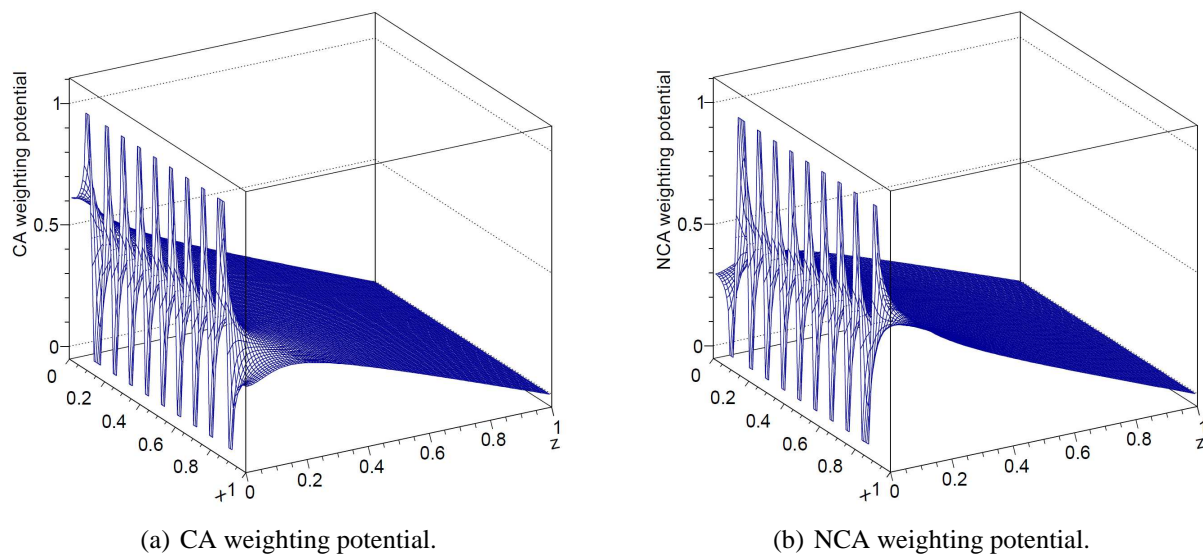


Figure 4.2: Weighting potentials of CA and NCA across a plane through the center of a CPG detector [F⁺13]. In both cases, φ_W rises linearly throughout the crystal bulk, and splits up near the anodes at $z = 0$ to become much steeper.

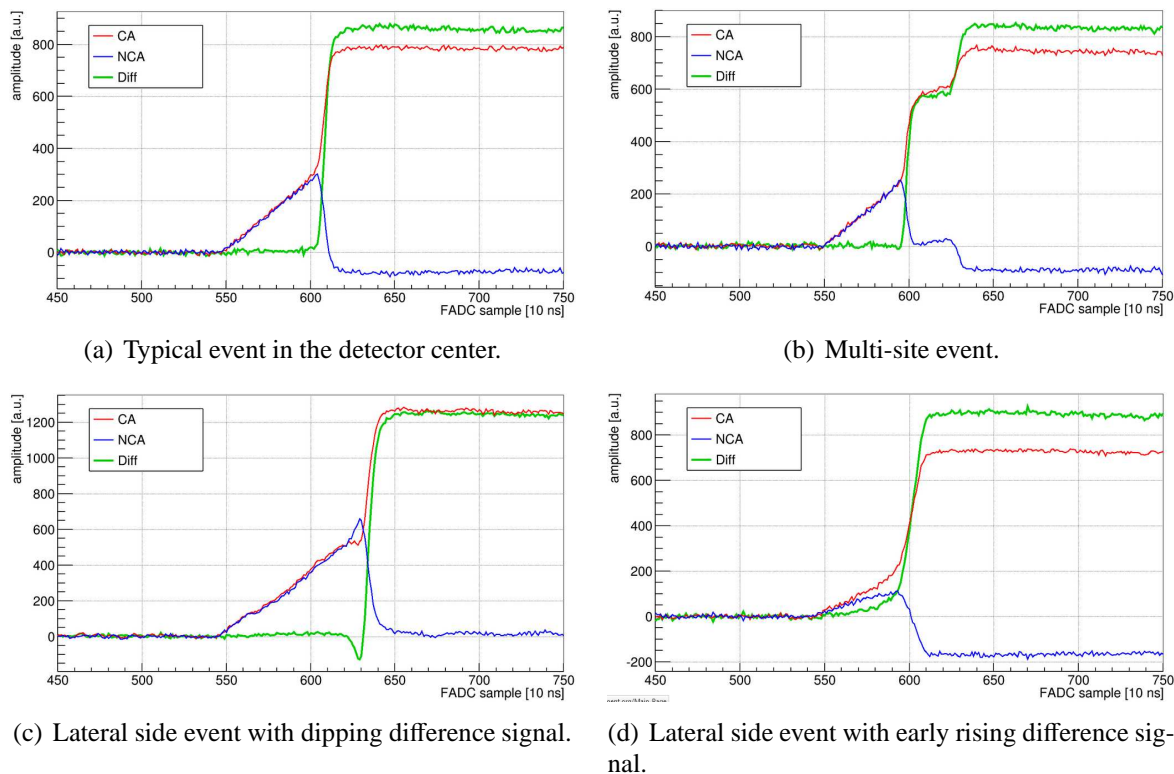


Figure 4.3: A selection of typical CPG signals. The CA signal is colored in red, the NCA signal in blue. The green pulse is the difference of both.

baseline level around sample #620.

As stated in the following section, the energy reconstruction algorithm is strongly related to the difference between CA and NCA signal, plotted green in the sample pulses. For a standard central event such as shown in figure 4.3 (a), the difference pulse is flat until the divergent behavior of CA and NCA signal near the anodes causes a fast rise. But the study of the difference signal also has a meaning beyond the energy determination. It is a tempting candidate for pulse shape analysis since it shows only slight energy dependence, and coincident distortions on CA and NCA signal are cancelled out.

Assuming that a traversing particle leaves energy in distinct detector regions, the signal is a shifted superposition of the discussed properties. This might result in a stepwise signal rise. An example for a so-called multi-site event is shown in figure 4.3 (b). By obtaining more than one peak in the derivative of the difference signal, such events can be classified [Zat14].

Another application is the identification of events from the lateral detector surfaces [FT⁺14]. Due to weighting potential deformations, such events show some characteristic features in the difference signal, depending on the detector side with respect to the anode geometry. In the case that the outermost anode strip belongs to the NCA, the difference signal dips significantly below the pre-baseline before rising to its final baseline level, see figure 4.3 (c). For a CA strip, the signal rise sets in earlier than usual, see figure 4.3 (d).

The identification of multi-site and lateral side events shows how the recording of pulse shapes provides valuable information with respect to background reduction.

4.1.3 Reconstruction of Energy and Interaction Depth

The change Δq in induced charge on the CA and NCA and thus the signal amplitudes can be derived from the Shockley-Ramo theorem:

$$\Delta q_{CA} = \frac{1}{2}Q_0(z + 1), \quad \Delta q_{NCA} = \frac{1}{2}Q_0(z - 1) \quad . \quad (4.2)$$

Q_0 denotes the total amount of generated charge carriers and is directly proportional to the deposited energy E_{dep} . E_{dep} can be obtained by calibration using sources with well-defined energy peaks. By convention, the relative interaction depth z is defined to be 0 at the anode plane and 1 at the cathode, so that the mobile electrons drift in negative z -direction. From the relations in (4.2), it is apparent that the cathode signal becomes obsolete for energy reconstruction, since

$$Q_0 = \Delta q_{CA} - \Delta q_{NCA} \quad , \quad (4.3)$$

and also the interaction depth can be gained using

$$z = \frac{\Delta q_{CA} + \Delta q_{NCA}}{\Delta q_{CA} - \Delta q_{NCA}} \quad . \quad (4.4)$$

As a zeroth-order approximation, equations (4.3) and (4.4) describe an ideal detector, but have to be adjusted to take into account intrinsic carrier trapping effects which are unavoidable in real

detectors and become perceptible especially in CZT. For events with higher interaction depth, i.e. events with longer electron drift, the signal loss due to electron trapping is higher. Δq_{NCA} , basically rising with the interaction depth, is weighted with a factor w in the signal difference to counteract this effect. w is defined to be smaller than 1. Its physical meaning is linked with the mean electron trapping length λ via

$$\lambda = \frac{1+w}{1-w} . \quad (4.5)$$

The weighting factor has to be obtained experimentally for each detector. Since trapping results from crystal defects, see section 4.2.2, w can also be understood as a kind of quality indicator for detectors.

The obtained total charge deposition, now corrected for electron trapping, reads

$$Q_{0,tc} = \Delta q_{CA} - w\Delta q_{NCA} . \quad (4.6)$$

It is possible to consider trapping also in the z reconstruction:

$$z_{tc} = \lambda \ln \left(1 + \frac{1}{\lambda} \frac{\Delta q_{CA} + \Delta q_{NCA}}{\Delta q_{CA} - \Delta q_{NCA}} \right) . \quad (4.7)$$

In the limit of high w , i.e. towards an ideal crystal, this expression becomes the zeroth-order formula from equation (4.4).

Although the cathode signal is not used, there is also a small impact of holes to the reconstruction. Drifting holes add signal to the anode pulses. In the difference signal and therefore in the determination of E these contributions cancel each other. Though, in the z reconstruction, which is based on the sum signal, they add up. The trapping of holes, which is very likely to happen within the signal measuring time, makes things even more complicated and theoretically demands for a treatment like for electron trapping, but unlike λ , the mean hole trapping length ρ is difficult to determine. This results in an overestimation of z of about 10% for events far from the cathode². For events near the cathode there is no overestimation, since the holes get directly collected.

A full description of the analytical model used to derive equations (4.6) and (4.7) can be found in [F⁺13].

4.2 Charge Cloud Dynamics

Ionizing particles that pass the semiconductor detector create not only single electron-hole pairs, but clouds of ten thousands of charge carriers. The behavior of such clouds is driven by a complex interplay of diverse physical effects, some of which will be discussed here. An important

²The overestimation value is obtained from consideration of the $\mu\tau$ products for electrons and holes. For CZT these differ by a factor of 10^{-3} . Typical values for λ are around 10, and therefore ρ is estimated to be at the order of 0.1.

issue for event reconstruction is carrier trapping, as discussed above. Moreover, size and shape of the clouds, as well as deformations throughout the drift play an important role for the analysis and simulation of pulse shapes.

4.2.1 Size and Shape of the Initial Cloud

A semiconductor detector is based on the fact that the number of generated charge carriers is directly proportional to the deposited energy E_{dep} . Once the ionization energy E_{ion} is known, the number N_e of electrons in the charge cloud can easily be calculated as

$$N_e = \frac{E_{dep}}{E_{ion}} . \quad (4.8)$$

E_{ion} is 4.64 eV for CZT. For the observed energies between 100 keV and several MeV this means a total of 10^4 - 10^6 electrons. Their initial distribution is linked to the ionizing processes and depends therefore on the kind of primary particle. Higher energetic, heavy charged particles are slowed down mainly via electronic stopping, i.e. inelastic collisions with bound electrons in the medium. Nuclear stopping, i.e. interactions with the nuclei, only occurs for low energies. A famous formula derived in the 1930s by H. Bethe [Bet30] and F. Bloch [Blo33] states that the energy loss $-dE$ per path length dx due to ionization in matter is given by

$$-\frac{dE}{dx} = \frac{z^2 e^4 n_e}{4\pi \epsilon_0^2 v^2 m_e} \left(\ln \frac{2m_e v^2}{I} - \ln(1 - \beta^2) - \beta^2 \right) . \quad (4.9)$$

Here, the elementary charge e multiplied by an integer z gives the charge of the primary particle, v is its velocity, n_e is the electron density in the absorber, ϵ_0 is the vacuum permittivity, and m_e is the electron mass. I represents the average excitation and ionization potential of the traversed medium. β is the conventionally used notation for $\frac{v}{c}$ with c being the speed of light. The equation, predicting an energy loss, sometimes also called stopping power, which rises with the decrease in particle velocity, holds only for high energies. For low energies, the particle accumulates electrons hence reducing its effective charge. Consequently, $-\frac{dE}{dx}$ falls off again. The maximum energy loss is reached when v is in the range of velocities of orbital electrons inside the absorber medium. The loss plotted against the path length, depicted in figure 4.4 (a), shows a characteristic maximum at the end of the path, called Bragg peak, which can in fact be observed for heavy charged particles including alphas.

For fast electrons and positrons further effects have to be considered. In contrast to heavy particles, betas are as light as their collision partners and thus large scattering angles are possible. Furthermore, the calculation of energy loss has to account for the fact that the interacting particles are indistinguishable [Leo94a]. According to Bethe, the collision losses are given by

$$-\frac{dE}{dx} = \frac{e^2 n_e}{8\pi \epsilon_0^2 v^2 m_e} \left(\ln \frac{m_e v^2 E_e}{2I^2(1 - \beta^2)} + (1 - \beta^2) - \frac{2\gamma - 1}{\gamma^2} \ln 2 + \frac{1}{8} \left(\frac{\gamma - 1}{\gamma} \right)^2 \right) , \quad (4.10)$$

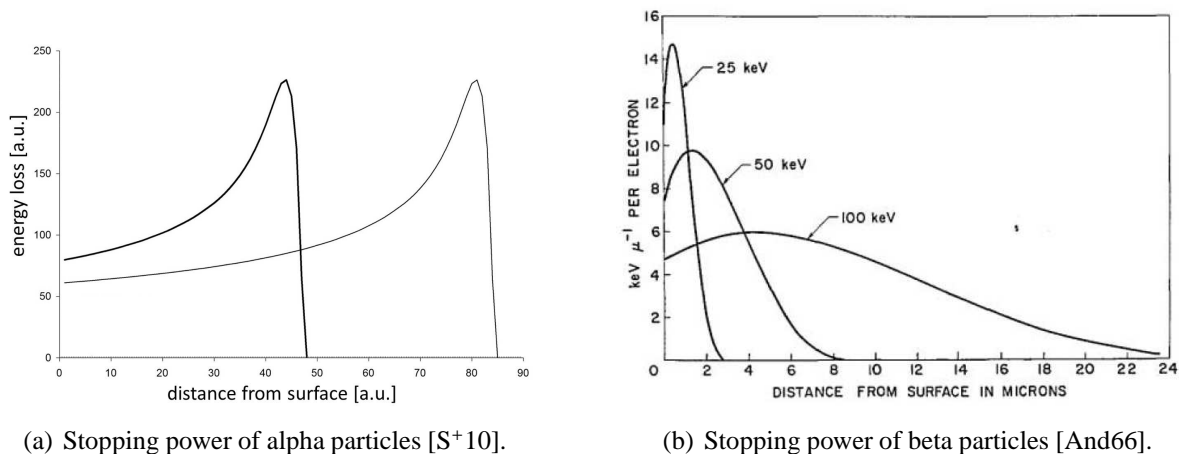


Figure 4.4: Energy loss as a function of travelling distance for alpha and beta particles. In case of the alphas, most of the energy is deposited at the end of the track at the so-called Bragg peak. For betas the curve is much more continuous.

with E_e being the relativistic kinetic energy of the beta particle and the relation $\gamma = \frac{1}{\sqrt{1-\beta^2}}$. Additionally, radiative losses can occur e.g. due to bremsstrahlung, but these are hardly relevant for the energies of interest. The shape of the energy loss plotted against the path length is shown in figure 4.4 (b). The curve is much more continuous for betas than for alphas.

Gamma rays interact with matter in different ways. Depending on their energy, either photoelectric absorption, Compton scattering or pair production occurs. In each case, a free electron (and an additional positron in the latter case) is produced for which equation (4.10) is valid.

Equations (4.9) and (4.10) both state $-\frac{dE}{dx}$ to be roughly proportional to $\frac{z^2}{v^2}$. Since alphas are much heavier and carry the double amount of charge, they lose their energy straight away and penetrate the material much less than betas of comparable energy. Neglecting statistical energy loss fluctuations, an average path length Δr can be calculated for ionizing particles in matter by integrating the inverse of the energy loss with respect to energy:

$$\Delta r_{CSDA} = \int_0^{E_{dep}} \left(-\frac{dE}{dx} \right)^{-1} dE \quad . \quad (4.11)$$

Δr_{CSDA} is called continuous slowing down approximation (CSDA) range. Figure 4.5 shows the CSDA range for alphas and betas in Sn and CdTe, respectively, plotted against the incident particle energy. The data was calculated with the programs ASTAR³ and ESTAR⁴, which are distributed by the NIST⁵. Since no CZT data was available, the materials were chosen with regard to similar atomic and proton numbers. Δr_{CSDA} is given for the COBRA relevant energy range below 3 MeV. While for alphas Δr_{CSDA} is at the order of μm , the betas cover up to mm distances. Nevertheless, the CSDA range must not be understood as the extension of the charge

³Stopping Powers and Ranges for Alphas, [htta].

⁴Stopping Powers and Ranges for Electrons, [httb].

⁵National Institute of Standards and Technology.

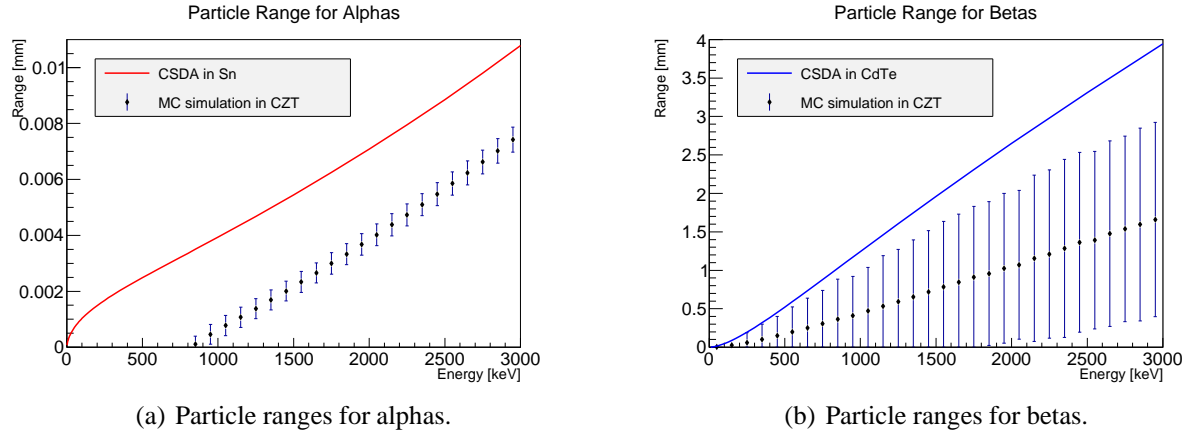


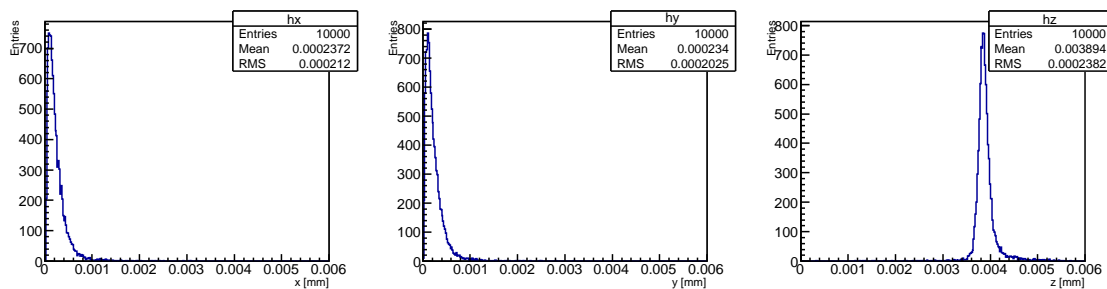
Figure 4.5: Particle ranges plotted against particle energy for alphas and betas in CZT or comparable materials in terms of atomic and proton number. The CSDA data was obtained from the NIST programs ASTAR and ESTAR, respectively. Δr_{cloud} is defined as the distance between the outermost created charges w.r.t. the initial momentum direction of the primary particle. It was obtained from MC simulations in CZT. Δr_{CSDA} and Δr_{cloud} are given for the COBRA relevant energy range below 3 MeV. While for alphas the ranges are at the order of μm , the betas cover up to mm distances.

cloud in the direction of the initial particle momentum. Although it is a first hint on it, the actual longitudinal cloud size Δr_{cloud} is smaller since neither alphas nor betas travel straight ahead through the material.

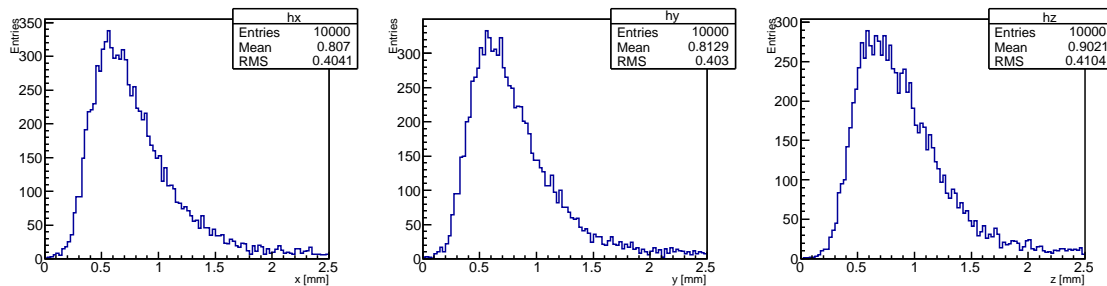
Figure 4.5 gives also an impression of Δr_{cloud} , defined as the distance between the outermost created charges with respect to the initial momentum direction of the primary particle. The values were obtained from Monte Carlo (MC) simulations of alphas and betas in CZT⁶. Each data point represents the mean value of Δr_{cloud} from 10 000 simulated particle tracks. For alphas below 800 keV, Δr_{cloud} is reconstructed as 0 since in this case Geant4 does not deposit energy at more than one spot. The error bars were set w.r.t. the root mean square (RMS) of the Δr_{cloud} distributions and therefore reflect the degree of particle scattering. Although smaller, the actual cloud sizes are at the same scale as the respective CSDA ranges. Because electrons are deflected harder, the deviations here are higher than for alphas. The deflection also accounts for the lateral extension of the charge clouds, as can be seen in figure 4.6 using the example of 1.7 MeV particles from the MC simulations. The alpha momenta after each collision are mainly forward directed (meaning here: in z -direction), resulting in small lateral cloud sizes. For betas on the other hand, it is not unlikely that the lateral cloud extension even exceeds the longitudinal size. Furthermore it can be concluded from the stopping power profiles in figure 4.4 that the charge carriers generated by an alpha are highly concentrated at the end of the particle track, leaving the cloud even more compressed than already done by the short particle path. For an incident beta however the distribution is expected to be a little more uniform.

Figure 4.7 shows the simulated locations of energy deposition in the crystal from both a randomly chosen 1.7 MeV alpha and beta. The particles were shot in z -direction, the starting point is marked with a red arrow. The projection of the particle path on the depicted plane becomes

⁶All MC simulations described in this thesis were performed with the simulation package VENOM, which is based on the software toolkit Geant4. The used software is described in appendix B.



(a) Cloud extensions for alphas.



(b) Cloud extensions for betas.

Figure 4.6: Charge cloud extensions for 1.7 MeV alphas and betas in CZT as obtained from the MC simulation. The particles were shot in z -direction. For betas the large scattering angles cause a high lateral extension.

visible and also do the discussed properties of alpha and beta clouds. The alpha track is straight, with only small lateral components, while the beta is hard scattered frequently, causing the lateral cloud extension to be as large as the longitudinal one.

4.2.2 Trapping

In high-resistivity semiconductors such as CZT the trapping of charge carriers plays an important role for the charge transport. Traps are localized energy states within the otherwise forbidden gaps between energy bands. Other than shallow impurities, which lie near the band edges and are used for material doping, those states are located in the middle of the gap and therefore called deep impurities. A passing charge carrier can fall into a trap and be immobilized for a while. The time until the carrier is detrapped and released into the band from which it came can be longer than the signal collecting time of the detector, so that the charge is lost for the rest of the signal. There are deep impurities that are capable of capturing both a hole and an electron which subsequently recombine and will not be collected at all. In most crystals, recombination through such centers is more common than direct recombination across the full band gap [Kno10].

The main contribution to trapping comes from impurities that arise from noble metal contaminations. These can be reduced during manufacturing by the use of high-purity basic elements and an appropriate production process. Structural defects within the crystal lattice such as Cd vacancies or interstitial Te atoms behave as acceptors and donors, respectively, and are much more difficult to avoid.

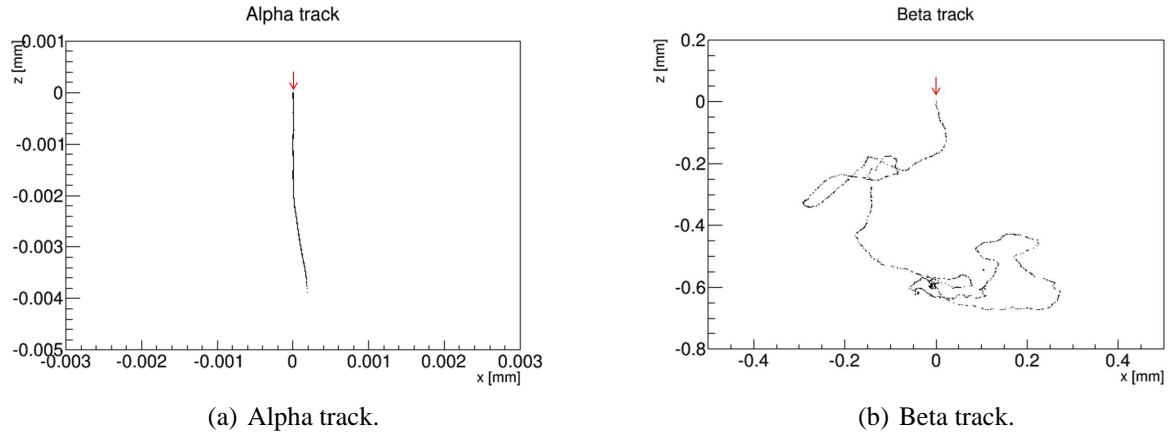


Figure 4.7: Locations of energy deposition for MC simulated events in two dimensions. The projection of the particle path on the depicted plane becomes visible. The particles were both shot in y -direction. The starting point is marked with a red arrow.

During the cutting process of the crystal, irreversible damage is done to the surfaces. Although the outermost crystal layer is removed after the mechanical cutting by mechanical polishing and chemical etching, the trap density towards the surfaces is typically still much higher than in the bulk of the crystal. The surface quality of CZT crystals was investigated e.g. by Tepper *et al.* [Tep01].

The average time that a carrier is trapped before being released is called detrapping time τ_d , as opposed to the trapping time τ that a carrier can move on average in the medium before being trapped. Both times depend on the purity and manufacturing process of the individual crystal. Typical CZT values for τ are at the order of 100 ns for both electrons and holes [Bal09, eV 13]. While recent studies suggest that τ_d can be of the same order or even smaller [RR⁺15], the common opinion is that τ_d is one or two magnitudes higher than τ [Bal09].

In the limit of a large number of mobile charge carriers, a rate equation can be formulated for the total amount of moving charge Q after drift time t in the detector with respect to the initially deposited charge Q_0 :

$$\frac{dQ}{dt} = -\frac{Q}{\tau} + \frac{Q_0 - Q}{\tau_d}, \quad (4.12)$$

The solution of this differential equation is

$$\frac{Q(t)}{Q_0} = \frac{1}{\frac{\tau_d}{\tau} + 1} + \frac{1}{\frac{\tau}{\tau_d} + 1} \exp\left(-\frac{t}{\tau} - \frac{t}{\tau_d}\right), \quad (4.13)$$

which in the limit of a high detrapping time τ_d becomes

$$\frac{Q(t)}{Q_0} = \exp\left(-\frac{t}{\tau}\right). \quad (4.14)$$

Statistical fluctuations are neglected here.

4.2.3 Thermal Diffusion

The charge cloud represents a region of high carrier concentration compared to the residual environment. Subsequently the carriers migrate over time from the region of high concentration to regions of low concentration in order to drive the system toward a state of uniformity [Sze07]. According to Fick's laws of diffusion from 1855 [Fic55], which follow from the continuity equation, the distribution of a charge density ρ as a function of time t is determined by

$$\left(\frac{\partial \rho}{\partial t}\right)_{diff} = D \nabla^2 \rho, \quad \text{with } D = \frac{k_B T}{e} \mu . \quad (4.15)$$

Here, all other impacts on the charge movement are neglected. k_B is the Boltzmann constant, T is the temperature, e is the elementary charge and μ_e denotes the carrier mobility. D is called the diffusion coefficient. For electrons in CZT, D is approximately $25 \frac{\text{cm}^2}{\text{s}}$. Assuming the total amount of charge to be initially concentrated at one single spot, the broadening due to diffusion would make the cross section through the distribution at a later time t resemble a Gaussian function [Kno10]. A spherically symmetric Gaussian charge density is described by

$$\rho(r, t) = \frac{Ne}{(2\pi\sigma(t)^2)^{3/2}} \exp\left(-\frac{r^2}{2\sigma(t)^2}\right) , \quad (4.16)$$

where σ is the standard deviation and N the number of charge carriers of the respective type. This is inserted into equation (4.15). Multiplying by r^2 and integrating over the volume yields

$$\frac{\partial \sigma_{diff}(t)^2}{\partial t} = 2D \quad (4.17)$$

[B⁺09], leading then to the solution

$$\sigma_{diff}(t) = \sqrt{2Dt} . \quad (4.18)$$

Another way to see this is the picture of single charge carriers instead of a charge density. Here, equation (4.18) has the meaning that after a time step dt each carrier will have travelled the distance dr , where dr is Gaussian distributed with $\sigma_{diff}(t) = \sqrt{2Ddt}$.

To calculate the total cloud radius R_{diff} after the diffusion time t for a realistic initial cloud size R_i , which should reasonably be larger than 0, R_0 and $\sigma_{diff}(t)$ have to be summed quadratically [D⁺05], thus

$$R_{diff}(t) = \sqrt{R_0^2 + \sigma_{diff}(t)^2} = \sqrt{R_0^2 + 2Dt} . \quad (4.19)$$

4.2.4 Electrostatic Repulsion

Within the cloud, repulsive forces act on the charge carriers due to the presence of their mutual Coulomb potentials. These forces are stronger the more carriers are present and the closer they are sited. With the relation

$$\vec{j} = \rho\mu\vec{E} \quad (4.20)$$

for the current density \vec{j} , the charge density ρ , the carrier mobility μ and the electric field \vec{E} of the distributed charge one can devise the continuity equation for electrostatic carrier repulsion

$$\left(\frac{\partial\rho}{\partial t}\right)_{rep} = -\nabla\cdot\vec{j} = -\mu\nabla\cdot(\rho\vec{E}) \quad (4.21)$$

Thermal diffusion and external electric fields are being neglected. Analogous to the proceeding in case of diffusion, a differential equation for the standard deviation σ_{rep} of a Gaussian distributed charge cloud can be derived:

$$\frac{\partial\sigma_{rep}(t)^2}{\partial t} = \frac{\mu Ne}{12\pi^{3/2}\epsilon_0\epsilon_r\sigma_{rep}(t)} \quad (4.22)$$

where ϵ_r is the relative permittivity and all other notations are the same as before. There is no analytical solution to equation (4.22), but E. Gatti *et al.* [G⁺87] showed that for a uniform spherical charge distribution with initial radius R_0 the radius ΔR_{rep} after drift time t is given by

$$\Delta R_{rep}(t) = \sqrt[3]{\frac{3\mu Net}{4\pi\epsilon_0\epsilon_r}} \quad (4.23)$$

Since $\Delta R_{rep}(t)$ goes with the cube root of t , the total radius $R_{rep}(t)$ is obtained by building the cubic sum of R_0 and ΔR_{rep} :

$$R_{rep}(t) = \sqrt[3]{R_0^3 + \Delta R_{rep}(t)^3} = \sqrt[3]{R_0^3 + \frac{3\mu Net}{4\pi\epsilon_0\epsilon_r}} \quad (4.24)$$

So far, thermal diffusion and electrostatic diffusion were considered isolated from any other effects. In a real crystal, the actual expansion of the charge cloud would always be due to both effects. If they were two independent processes, one could simply add their contributions to the cloud size quadratically, such as proposed by Dönmez *et al.* [D⁺05]. Benoit *et al.* [B⁺09] modelled the migration of single electrons in large charge clouds in CZT using iterative Geant4 simulations. They found that the cloud radius resulting from the quadratic sum slightly overestimates the actual cloud size. The reason is the coupling between both effects, since after a time step dt the impact of repulsion decreases due to the simultaneous expansion from thermal diffusion, so that theoretically equation (4.24) – or its equivalent with the numerical solution of equation (4.22) – would have to be recalculated after each time step.

Anyhow it is possible to reflect equations (4.19) and (4.24) in order to make a general statement about their contributions to the total cloud expansion. σ_{diff} and ΔR_{rep} expand as the square root and as the cubic root of time, respectively, and so repulsion may become the dominant effect for short drift times in a detector. The impact is also dependent on the number of charge carriers and therefore on the amount of deposited energy. Since semiconductor detectors are often used for spectroscopic purposes where gamma radiation in the range of several tens of keV is

detected, electrostatic repulsion is hardly discussed in the literature concerning carrier drift. For high energies in the range of MeV, it definitely has to be taken into account.

Generally one might argue that the carriers in the charge cloud are far from being Gaussian distributed and the analytic models both in this and in the previous section are not suitable for realistic statements. But as could be shown by Benoit *et al.* the time evolution of the RMS values is not too dependent on the details of the distribution. Deviations are reported to be around 5 %.

4.3 Electric Field Studies

While the drifting electrons induce a signal which follows the weighting potential introduced in section 4.1.1, their actual movement is mainly determined by the distribution of the electric potential. The generated charge carriers follow the electric field lines until they finally get collected by an electrode. The above explained diffusive and repulsive effects are superimposed on the drift.

The internal electric field is dominated by the biases applied to the electrodes. Further contributions arise from surfaces and metal-semiconductor junctions at the electrodes, all discussed in the course of this section.

4.3.1 Electrode Biases

A simulation of the electric potential inside an ideal 1 cm^3 CZT detector was carried out by using the finite element modeling software COMSOL Multiphysics⁷, at first disregarding possible effects due to surfaces and junctions. The underlying anode geometry is depicted in figure 4.8. It was adopted from the detectors currently used at the COBRA demonstrator. The scheme also shows the guard ring which is surrounding the anode grids to prevent leakage currents to flow between cathode and anodes. The HV was set to -1 kV and the anode potentials were -100 V and 0 V . The guard ring was set to floating potential. The relative permittivity in CZT was assumed to be 10.9.

Figure 4.9 shows results from the simulation in the form of color plots. The electric potential in (a) is plotted on multiple slices through the detector center. For the plane perpendicular to the anode stripes, in (b) also the electric field is indicated by lines following the potential gradient. The simulation is consistent with the assumptions previously made, saying that the field is constant throughout most of the crystal. The field lines are not getting remarkably bent until the last eighth of the way toward the anodes at $z = 0$. In a closer look at the field lines landing on the anodes it can be observed that they do not all end at a CA strip, colored in red. Some lines lead to the outermost NCA, colored in blue. In practice this could result in charge

⁷The software is briefly described in appendix B.

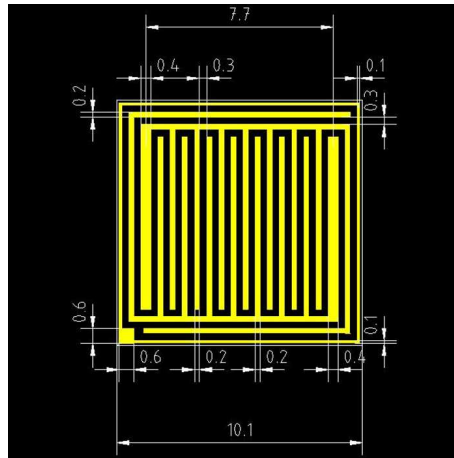
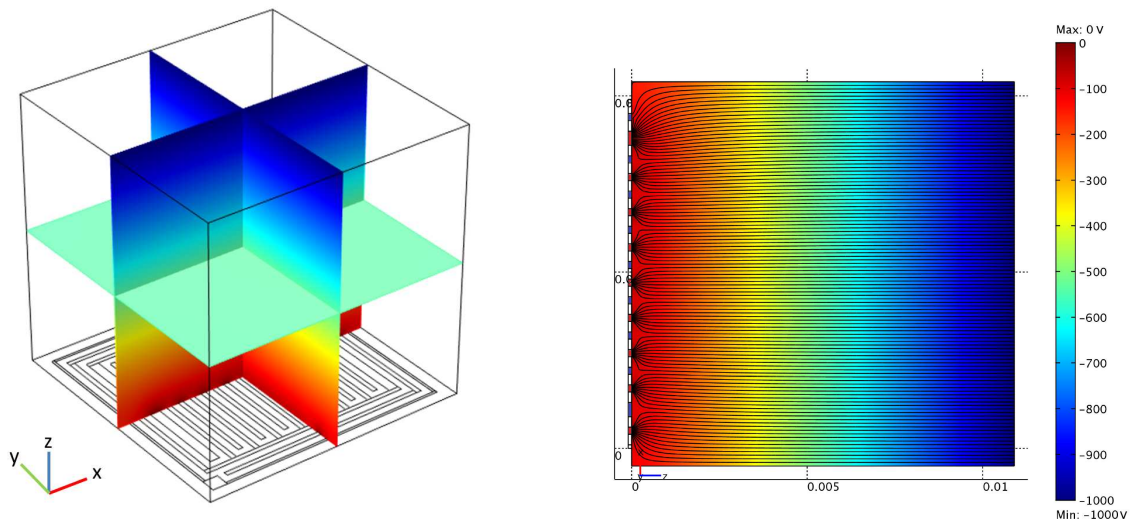


Figure 4.8: Scheme of anode geometry used in electric field simulations [JD]. The measurements were set with respect to the detectors currently used at the COBRA demonstrator. Numbers are given in mm.



(a) Multislice plot of the electric potential.

(b) 2D plot of the electric potential. The CA is colored in red, the NCA in blue.

Figure 4.9: Simulation of the electric potential of a 1 cm^3 CPG detector. The applied voltages were $HV = -1 \text{ kV}$ and $GB = 100 \text{ V}$. The 2D plot in (b) shows the potential and corresponding field lines on a plane through the detector center perpendicular to the anode strips.

sharing, meaning that for events near the adjacent surface not all charge carriers are collected by the CA. The energy for such events would be underestimated in the reconstruction.

4.3.2 Space Charge Regions

As mentioned in the context of trapping centers in section 4.2.2, the density of states inside the forbidden energy gaps is very high near surfaces. This is mainly due to the mechanical cutting of the crystals during manufacturing, which causes structural lattice defects. But even with an ideal surface with atoms at bulk-like positions, new electronic levels and modified many-body effects are formed due to the change in chemical bonding – a case that is conclusively given at a surface. Mobile carriers can occupy the surface states and will represent a perturbation to the local charge balance. Consequently, neighboring carriers of the opposite charge will rearrange to compensate for the additional charge. Since the density of free charge carriers is low in semiconductors, the screening lengths are high compared to metals. In semiconductors, these are at the order of hundreds of ångströms instead of atomic distances in metals. Such spatial regions of redistributed screening charges are called space charge regions [Lüt15]. Depending on the concentration and the type of surface states, these can lead either to an increase or a decrease in conductivity. In CZT, surface regions are usually more conductive than the bulk of the material.

In addition to surface states, fixed interfacial charge can be present, when an oxide is deposited on the semiconductor surface [P⁺01]. High surface conductivity and fixed interface charge have an impact on the electric field that can reach up to several hundreds of microns deep into the bulk of the material [P⁺01].

Space charge regions can also form inside the bulk of the crystal, e.g. at grain boundaries. Furthermore, inclusions and precipitates of Te form regions of higher conductivity due to the narrow band gap of Te (~ 0.3 eV). These may distort the electric field distribution and the carrier transport [Car06]. In an undisturbed, constant electric field, the detector signals should rise linearly. This is the ideal case for drifting charge clouds that have not yet reached the near anode region. Field perturbations in the bulk should therefore be visible in the pulse shapes. All of the operated detectors at LNGS, however, show a behavior as depicted in figure 4.3. The linear part of the slopes do not show any sign of systematic curvature. If space charges are present in the bulk, they are not strong enough to visibly affect the signals. The same goes for the impact of Te inclusions and Te precipitates.

4.3.3 Metal-Semiconductor Junctions

The electrode contacts on the crystal form metal-semiconductor junctions. To understand the electronic behavior inside the CZT, it is helpful to once again consider the band schemes of the involved materials. Figure 4.10 shows the energy bands before (a) and after (b) connecting a

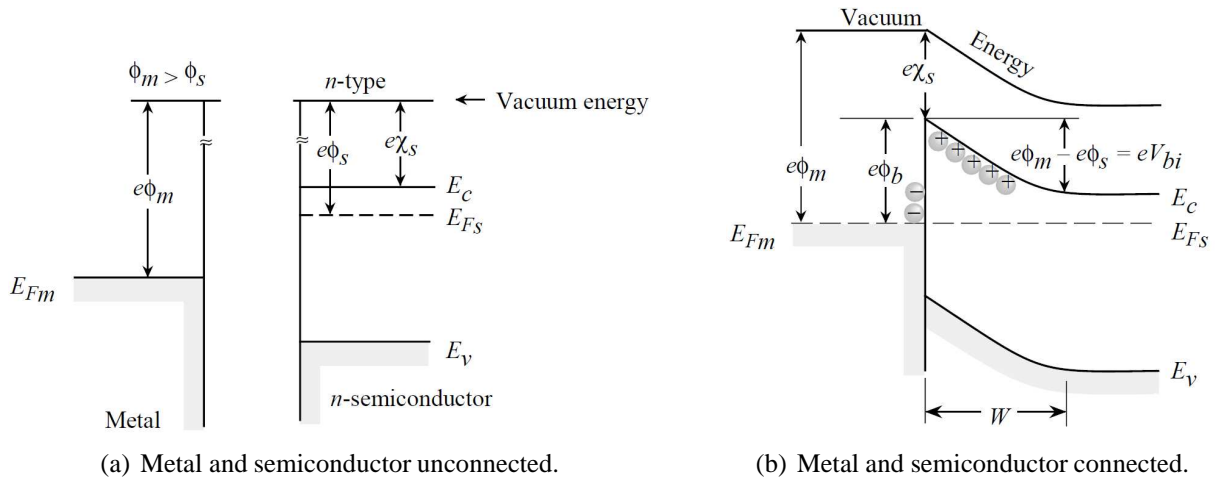


Figure 4.10: Formation of a Schottky junction using the example of an n-type semiconductor [Sin00]. The work function of the metal $e\Phi_m$ is higher than for the semiconductor, i.e. $e\Phi_s$. Subsequently, the Fermi levels E_{Fm} and E_{Fs} are different. When both materials are brought into contact, thermal equilibrium requires the Fermi levels on both sides of the interface to be equal. Electrons from the conduction band will flow into the metal, causing both conduction and valence band to bend up. The electron affinity $e\chi_s$ remains the same before and after the connection. The resulting potential barrier, given as the difference between $e\Phi_m$ and $e\chi_s$, prevents electrons to flow from the metal into the semiconductor and is known as the Schottky barrier $e\Phi_b$. W is the width of the arising depletion layer.

metal and a semiconductor. The work function $e\Phi$ is defined as the minimum thermodynamic work needed to release an electron from the material into an outside vacuum. In the depicted case, it is higher for the metal than for the semiconductor, i.e. $\Phi_m > \Phi_s$. Subsequently, the Fermi levels E_{Fm} and E_{Fs} for the metal and the semiconductor, respectively, are different. In the example, this difference is further enlarged due to an n-type doping of the semiconductor, lifting up E_{Fs} a little. When both materials are brought into contact, thermal equilibrium requires the Fermi levels on both sides of the interface to be equal. The lower edge of the conduction band is marked as E_C , the upper edge of the valence band as E_V . Electrons from the conduction band will flow into the metal, causing both conduction and valence band to bend up until the equilibrium is reached. The electron affinity $e\chi_s$, defined as the difference between vacuum energy and E_C , remains the same before and after the connection. The resulting potential barrier, given as the difference between $e\Phi_m$ and $e\chi_s$, prevents electrons to flow from the metal into the semiconductor and is known as the Schottky barrier $e\Phi_b$. The width of the arising depletion layer is labelled as W in the scheme.

If a voltage V is applied to the system, this has an immediate impact on the band structure, as depicted in figure 4.11. The positions of the Fermi levels get shifted against each other, while the direction of the shift depends on the bias. A forward bias, see figure 4.11 (a), implies an upward shift of eV for E_{Fs} , while a reverse bias, see figure 4.11 (b), has a contrary effect. As can be seen, this has a large impact on the semiconductor-to-metal barrier, which keeps electrons from flowing from the semiconductor into the metal. The depletion zone is compressed in case of a forward bias and stretched in case of a reverse bias. The Schottky barrier, on the other hand, remains unchanged.

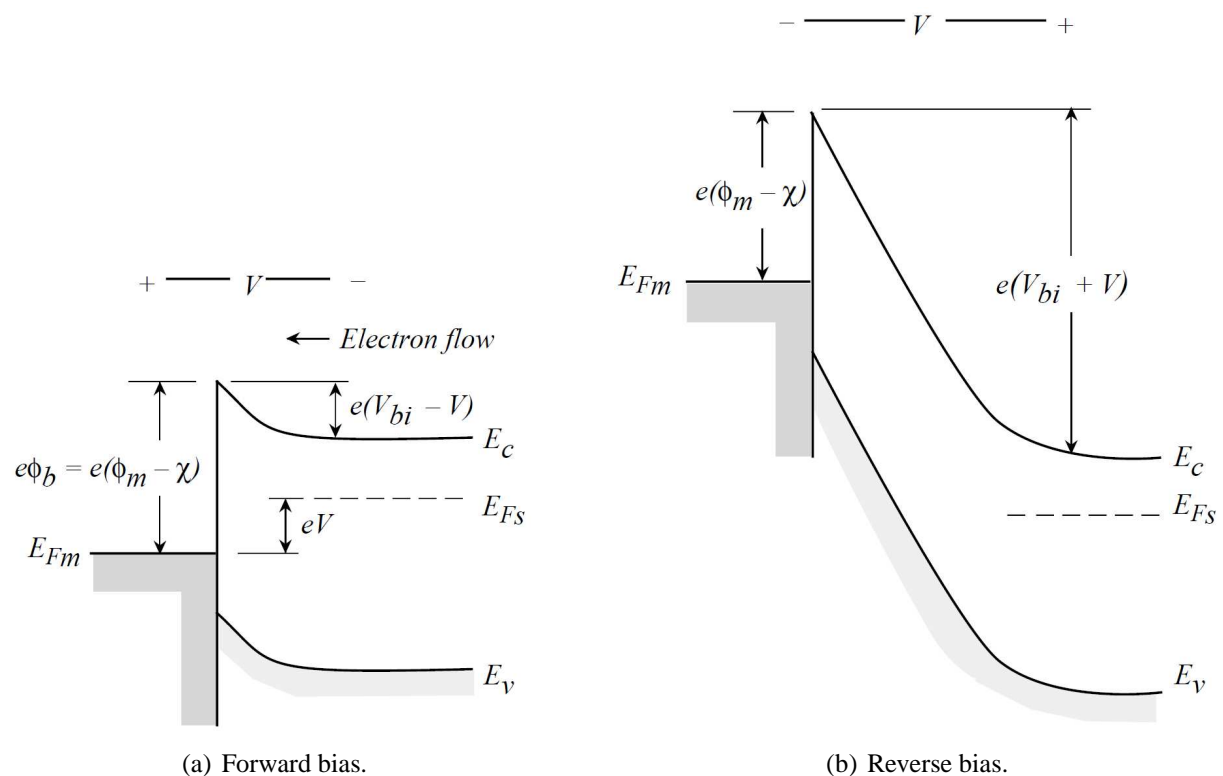


Figure 4.11: A bias is applied to a metal-semiconductor junction [Sin00]. Depending on whether the bias is forward or reverse, the semiconductor-to-metal barrier, and also the width of the depletion zone, is decreased or increased. The Schottky barrier, on the other hand, remains unchanged.

The Schottky contact was explained on the basis of the electron behavior. For holes, the definitions and processes work analogously.

Another electric field study was carried out with COMOSL Multiphysics. Due to the complexity of the anode geometry, it was necessary to reduce the problem to two dimensions in order to implement the Schottky contacts. The simulated detector was a $200\ \mu\text{m} \times 1.09\ \text{cm}$ CZT strip with two back-to-back Schottky contacts at the ends. The width of the strip was chosen w.r.t. an anode pin, its length corresponds to the actual detector depth. All used material properties are listed in table 4.1.

First, a simulation was done without any bias applied to the electrodes. It delivered the con-

Table 4.1: Material properties used in the COMSOL simulation.

| Property | CZT | Cathode | Anodes |
|---|-------|---------|--------|
| Density ρ [g/cm ³] | 5.78 | | |
| Relative permittivity ϵ_r | 10.9 | | |
| Electron mobility μ_e [cm ² /(Vs)] | 1 000 | | |
| Hole mobility μ_h [cm ² /(Vs)] | 70 | | |
| Band gap E_g [eV] | 1.64 | | |
| Electron affinity $e\chi$ [eV] | 4.4 | | |
| Work function $e\Phi_m$ [eV] | | 5.0 | 5.3 |
| Schottky barrier $e\Phi_b$ [eV] | | 0.6 | 0.9 |

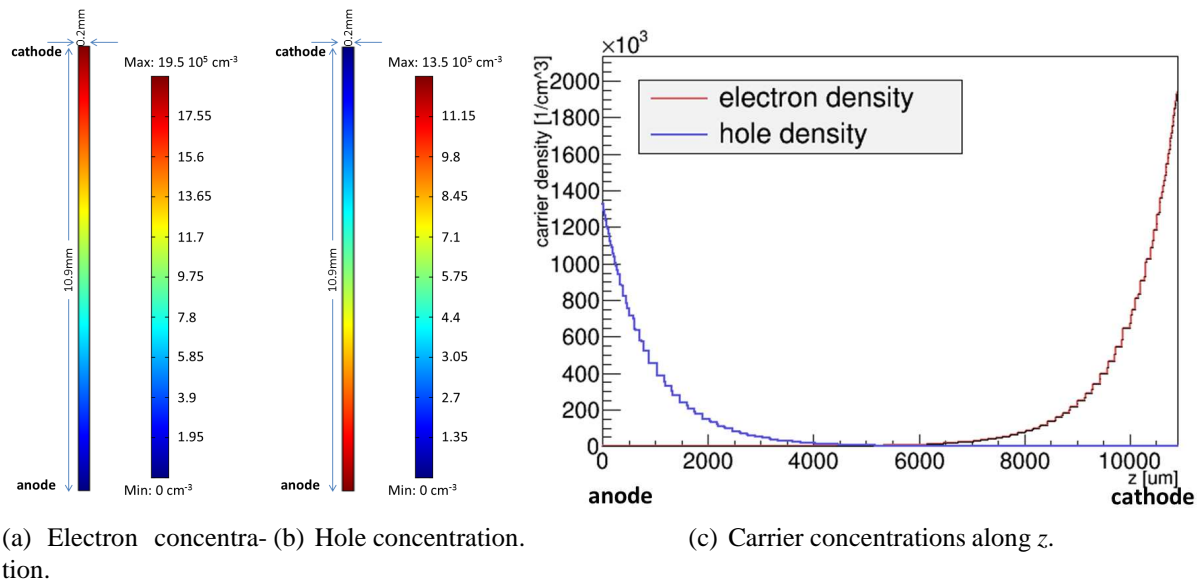


Figure 4.12: Simulated charge carrier concentrations at Schottky contact. No bias is applied between anode and cathode. The electron density is reduced near the anode and rises towards the cathode. For the hole density it is vice versa. The Schottky contacts are noticeable through the hole detector.

centration of charge carriers depicted in figure 4.12. The two color plots in (a) and (b) show the spatial distribution of electron and whole density throughout the detector strip. Figure 4.12 shows both carrier concentrations along the detector depth across the middle of the strip. Due to the assumed semiconductor electron affinity and metal work functions, the electron density is very much reduced near the anode and rises towards the cathode. For the hole density it is vice versa. The Schottky contacts have an effect that is noticeable through the hole detector.

In the next step, the bias between anode and cathode was set to 1 000 V. The analog results can be seen in figure 4.13. The space charge regions are most widely forced back so that the carrier densities are constant along the bulk. In order to see any effect of the junctions at all, the color plots had to be zoomed in massively. A density gradient is present only immediately near the electrodes. The density drops within $10\ \mu\text{m}$ in front of the anode in case of the electrons and within $10\ \mu\text{m}$ in front of the cathode in case of the holes. In terms of absolute values, the electric field would be increased minimally due to the space charges, whereas a deformation of the field would be spatially confined to a couple of μm . Assuming a drift velocity for of $10^4\ \frac{\text{m}}{\text{s}}$, see section 5.1.2, the carriers would pass the region in less than a nanosecond. Given the sampling rate of one per 10 ns, the temporal shaping of the detector signals would not be affected.

To summarize the preceding results, the simulations confirm that the internal electric field in the bulk of the material is clearly dominated by the applied voltages. Towards the surfaces, deep energy states and fixed interfacial charges can modify the field. The reach of such effects is expected to be limited to some hundreds of μm . Space charge regions within the bulk do in general not distort the pulses. The Schottky contacts at the anodes should not have a measurable effect on the observed pulse shapes either.

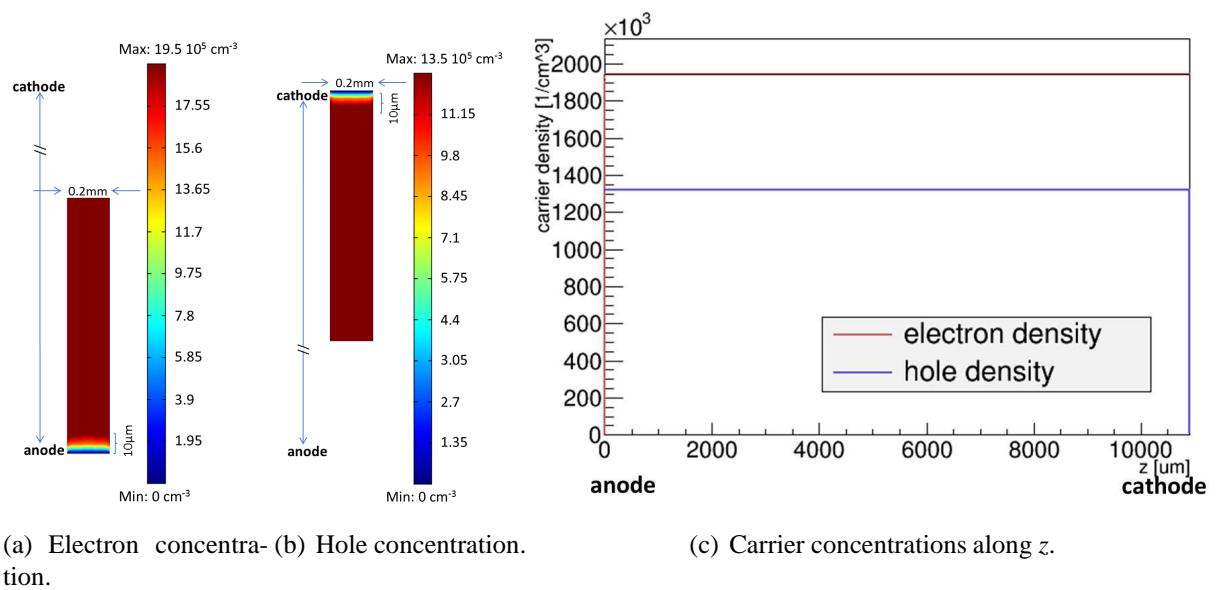


Figure 4.13: Simulated charge carrier concentrations at Schottky contact. A 1000 V bias is applied between anode and cathode. A density gradient is present only immediately in front of the electrodes.

It was formerly observed that the fraction of collected electrons at the CA and NCA is higher than predicted by electric field studies, i.e. charge sharing happens less frequently than expected [P⁺02]. This welcome effect might be due to layers of higher conductivity, which in turn can result from surface states or metal-semiconductor junctions.

A method to experimentally obtain the internal electric field of a CZT detector is to make use of the Pockels effect⁸. Studies can be found in [Y⁺99,Z⁺99].

⁸CZT is transparent to light from the infrared (IR). The crystal becomes birefringent when a voltage is applied. When exposed to IR radiation, the electric and magnetic vectors of the light are rotated with the intensity of the electric field. Since the birefringence changes linearly with the field, the Pockels effect is also called linear electro-optical effect.

Chapter 5

Development of a Detector Simulation

Event simulations for COBRA are generally carried out by Geant4-based MC simulations. For the passage of a particle through matter, these methods consider complex cascades of particle interactions and processes. As a result, they predict the amount of energy finally deposited in a specified volume, e.g. the detector. The MC simulation terminates at this stage, leaving all further aspects such as charge transport inside the detector or signal transport in the DAQ chain untouched. In order to consider electronic and detector response, the MC data has to be convolved with experimentally obtained detector uncertainties. The obtained MC energies have to be smeared retrospectively to consider the technically limited energy resolution in order to produce realistic spectra.

This procedure is justified when considering well-understood aspects of the detector behavior. Or in other words: When the detector response to a certain treatment is known, it is easy to artificially reproduce the effect in retrospect. When on the other hand the detector behavior itself is the field of interest, the above methods are not suitable any more, obviously. Problems arise for example when detection efficiencies for rare events such as double beta decays shall be determined. Since the experimental way is barred, a method has to be found to simulate the actual particle detection, including transport and collection of charges, leading to the generation of signal shapes. In principle, a detector simulation is always required when certain experimental data is hard to get, either because the studied process cannot be induced or because the detector region of interest is experimentally hard to access. This is the case for efficiency calculations for all kind of data cuts that apply to bulk events. In this sense, the detector simulation is essential for the efficiency determination of the alpha discrimination in chapter 6. Another example for a possible application is the investigation of signal loss in certain detector regions. The common MC simulations will not yield any enlightening information on the so-called dead layers, but a detector simulation can help to support or discard a hypothesis.

As a rule, the simulated results are the more accurate and revealing the more appropriate and detailed the underlying processes are implemented. This chapter describes the development of a detector simulation and presents simulated pulse shapes as a result. These are compared to real pulses and used to determine detector resolutions before conclusively discussing the

applicability of the presented method.

5.1 Process

The detector simulation presented here is based on a former version developed for the COBRA experiment by M. Fritts (University of Minnesota) which, within the scope of this thesis, was complemented with certain aspects of charge transport and electronics impact. Furthermore, the process was restructured in order to match current needs of the application.

The diagram in figure 5.1 shows the basic course of the simulation. All adjustable input parameters are listed in a column on the left. Broad arrows indicate at which point these enter the simulation. Framed rectangular boxes in the right-hand column represent the main processing stages. Their sequence is pointed out by thin arrows, leading finally to the output domain in the bottom right-hand corner. Boxes with rounded corners show intermediate results.

The detector simulation calculates a pulse for a specific detector event. In a first step, the desired event needs to be simulated with VENOM. The type of primary particle, its initial energy and direction and also the starting point have to be specified. VENOM returns a ROOT file, in which single points of energy deposition along the track of the primary particle are stored. The file is now passed to the actual detector simulation script which can be run with ROOT. The program starts with a loop over every single spot of energy deposition, marked in the diagram by a black rectangular frame. The charge movement of holes and electrons is simulated, taking into account the electrostatic repulsion between the electrons. Here, all spots are considered isolated: The exact constellation to neighboring spots has no impact on the movement. The charge carrier tracks are determined by the detector geometry. Their speed is influenced by the HV between cathode and CA, by the GB between CA and NCA, and by the electron and hole mobilities μ_e and μ_h in CZT. To calculate the corresponding signal, the knowledge of the weighting potential is required. It is obtained from a COMSOL simulation, which in turn has to be fed with the detector geometry. The weighting potential along the carrier tracks delivers the electron and hole contribution to the signal. In this step, trapping is considered in form of a continuous signal reduction, driven by the parameters w and ρ (see section 5.1.3). The two obtained signal contributions are added. The result can be understood as a signal from a dot-like energy deposition. In order to take into account the whole energy distribution in the crystal, the signals from the entire loop are summed up w.r.t. the amount of energy deposited at each spot. The energy weighted sum signal comes already very close to the response expected from the plain detector. But since in a real system the additional electronics do not leave a signal unaffected, the simulation has to undergo further treatment to make it resemble a realistic pulse. Therefore, a digital RC-CR filter is applied, demanding for the time constants τ_{rise} and τ_{fall} . Finally, noise is added, whereas the intensity is controlled by an adjustable noise level.

The final signal is saved in the same ROOT format as the experimental data. The sample rate is also identical. The pulse height is stored in arbitrary units, but since the shaping and noise

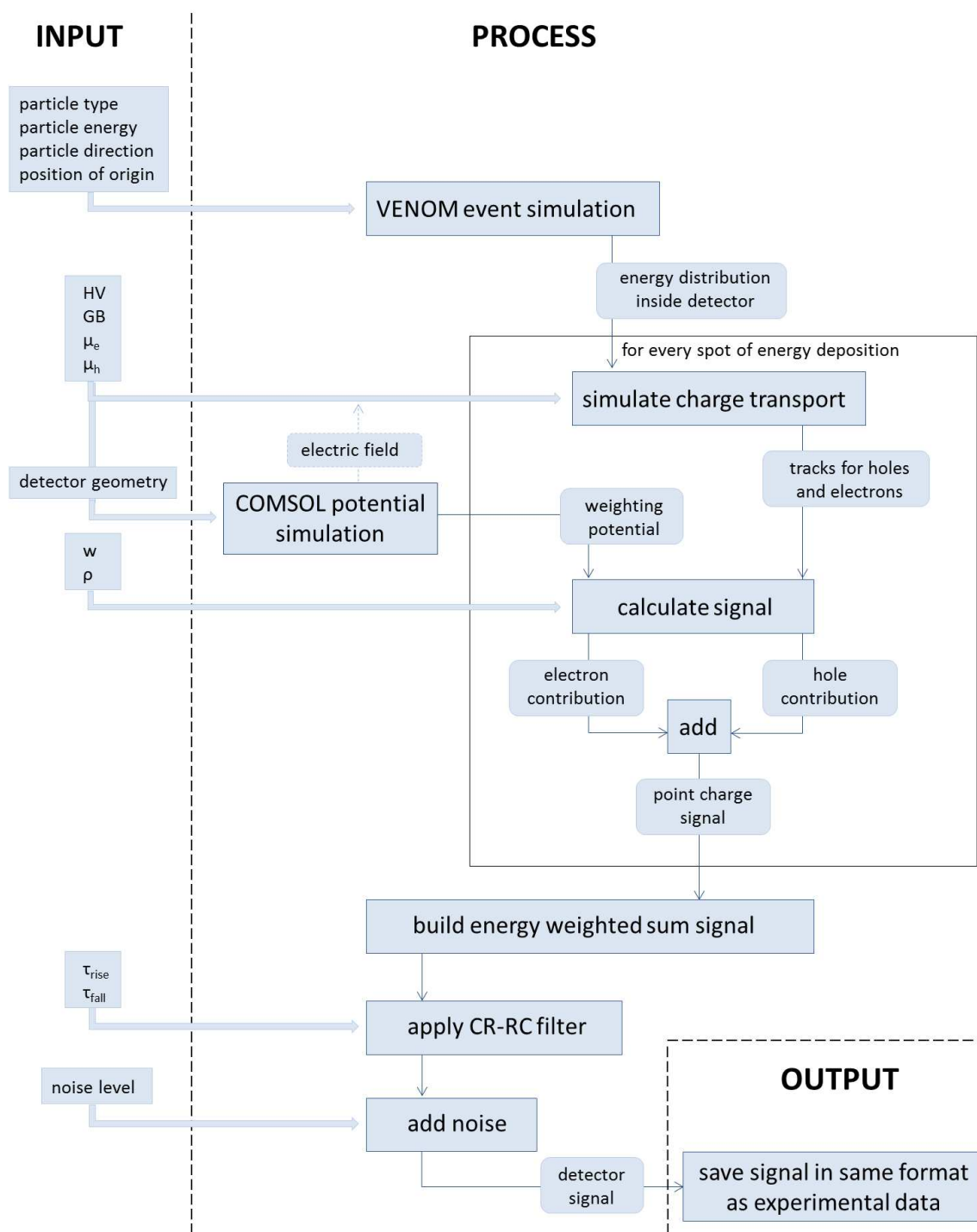


Figure 5.1: Schematic course of the detector simulation. All adjustable input parameters are listed in a column on the left. Broad arrows indicate at which point of the simulation these enter the simulation. Framed rectangular boxes in the right-hand column represent the main processing stages. Their sequence is pointed out by thin arrows, finally leading to the output domain in the bottom right-hand corner. Boxes with rounded corners show intermediate results.

features were implemented relatively w.r.t. the total pulse height, the simulated signals can be scaled easily to compare them to experimentally gained ones. The signal length is 300 samples, corresponding to $3\ \mu\text{s}$. The difference to the experimental signals with a length of 1024 samples is due to the absence of a pre-baseline and a shortened post-baseline. Additionally to the signal, information like the total deposited energy and coordinates for the energy weighted mean position of the interaction are stored.

A more detailed description of the different simulation stages will be given in the following sections.

5.1.1 VENOM Event Simulation

A VENOM event simulation is needed as input for the detector simulation. The particle type, particle energy, initial flight direction and the point of origin can be specified. The simulated distribution of energy deposition in the detector serves as basis for the initial charge cloud. Since for one detector event VENOM returns by default only the sum of all individual energy depositions and the mean position of the interaction, the source code has to be modified slightly. Basically, the lines

```

1 if(htIter != fHitTable.end()) {
2     (*fEdep)[(*htIter).second] += edep;
3     return ;
4 }
```

in the script `array64SensitiveCrystalData.cc` have to be commented out.

Care has to be taken in the choice of the Geant4 physics list. For underground physics, the lists `Shielding` and `DMXPhysicsList` are provided. Although the `Shielding` list proves more suitable for COBRA [Hei14], only very few spots of energy distribution are determined. By means of these spots, the track of the incident particle is not recognizable. Although depending on the total deposited energy, their number is up to several thousand with the `DMXPhysicsList`, instead. Tracks are identifiable and can be used as indications for cloud sizes. Therefore, the latter is the list of choice for the detector simulation.

5.1.2 Calculating Tracks

Charge Carrier Pathways

For every spot of energy deposition, the movement of both holes and electrons is being calculated. At the spot of energy deposition, electrons and holes are generated, treated here as an inseparable package of negative or positive charge, respectively. The pathway follows a very simple scheme. The holes are assumed to drift straight from their point of origin to the cathode. They follow a path which is parallel to the z direction, i.e. perpendicular to the electrode planes. This should in general approximate the orientation of electric field lines in the bulk of the crystal very well. The electrons on the other hand drift towards the anodes where they meet

a much more complex field distribution. In the simulation, they are assumed to drift along the z axis up to a distance of $700\ \mu\text{m}$ toward the anode plane. So far the electric field is assumed to be unaffected by the GB. From there on, the electrons head directly to the nearest CA strip. The approximate value of $700\ \mu\text{m}$ was chosen with regard to the field line simulations presented in section 4.3.1. However, a fluctuation of $\pm 300\ \mu\text{m}$ would not have perceptible impact on the final pulses.

The average speed v_0 of the charge carriers depends on the applied HV and GB. Using the relation

$$\vec{v}(r) = \mu(\vec{r})\vec{E}(\vec{r}) \quad , \quad (5.1)$$

stating that the instantaneous speed at a position \vec{r} is given as the product of mobility $\mu(\vec{r})$ and electric field $\vec{E}(\vec{r})$, the average velocity is estimated with an overall mobility μ and the detector length L to be

$$v_0 = \mu \left| \vec{E}(\vec{r}) \right| \approx \mu \cdot \frac{\text{HV} - \text{GB}/2}{L} \quad . \quad (5.2)$$

Obviously, this is a simplification of both the path and the drift velocity of carriers. Depending on the requirements concerning the accuracy of the pathway, it is also possible to calculate both parameters directly from an electric field simulation. Same as the weighting potential, the field can be calculated with COMSOL Multiphysics. The disadvantage of this method is that the field would have to be recalculated completely for every new combination of HV and GB, whereas the biases can easily be adjusted using the simplified approach. The significance for the generated pulse shapes however is marginal.

Effect of Thermal Diffusion and Electrostatic Repulsion

For an appropriate consideration of the charge cloud behavior, dynamic effects such as thermal diffusion and electrostatic repulsion have to be taken into account. General aspects concerning their nature and impact have been described in chapter 4. Now, it is important to know how they act on specific charge clouds in the fixed detector volume. Equation (4.18) implies that the change in cloud radius depends on the drift time t and carrier mobility. When $\mu = 1000 \frac{\text{cm}^2}{\text{Vs}}$, HV = 1000 V and GB = 100 V are inserted into equation (5.2), a drift velocity of approximately $10^4 \frac{\text{m}}{\text{s}}$ is obtained. The maximum electron drift distance of 1 cm is covered for events near the cathode. This leads to an approximate maximum drift time $t_{\text{max}} \approx 1\ \mu\text{s}$. For these values, equation (4.18) returns an expansion coefficient of $\sigma_{\text{diff}} \approx 70\ \mu\text{m}$, which has to be added quadratically to the initial cloud size to obtain the cloud radius at the end of the drift, see equation (4.19).

For electrostatic repulsion, the expansion is determined by the coefficient ΔR_{Rep} given by equation (4.23). Besides the drift time, it depends also on the number of charge carriers and therefore on the amount of deposited energy E_{dep} . Assuming the maximum drift time, ΔR_{Rep} is $295\ \mu\text{m}$

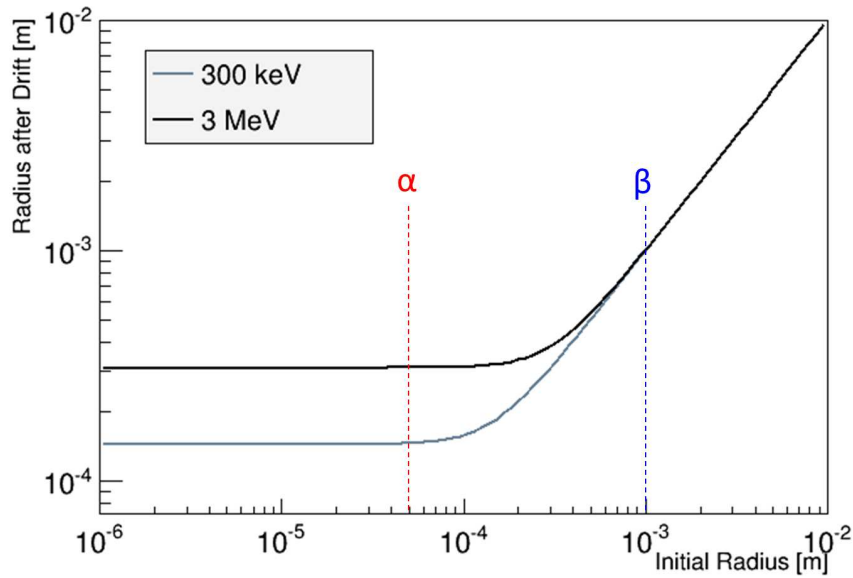


Figure 5.2: Charge cloud radius $R_{rep}(t_{max})$ for maximum drift time plotted against the initial radius R_0 considering electrostatic repulsion in a double logarithmic representation. Dashed lines mark typical initial radii for alphas and betas.

for $E_{dep} = 300$ keV and $635 \mu\text{m}$ for $E_{dep} = 3$ MeV. These values have to be added cubically to the initial cloud size to obtain the cloud radius $R_{rep}(t_{max})$ at the end of the drift, see equation (4.24). In figure 5.2, $R_{rep}(t_{max})$ was plotted as a function of the initial cloud radius R_0 for both energies. Dashed lines mark typical initial radii for alphas and betas. The repulsive effect is most pronounced for small clouds such as for alphas, enhancing the radii more than one order of magnitude. For the wide-spread beta distribution, the relative effect is hardly noticeable.

So far, thermal diffusion and electrostatic repulsion have been considered independently of each other. But since both effects are coupled, see section 4.2.4, they should in principle be combined. Although no analytic solution is available, the following thoughts allow some statement about their relative impact. The sought-for radius after the drift, having been influenced by diffusion and repulsion, is now called the real radius $R_{diff,rep}(t)$. Since diffusion has an enlarging effect on the cloud, it is clear that the cloud radius R_{rep} without diffusion is smaller than the real radius. To define an upper limit for $R_{diff,rep}(t)$, one can conclude that the real radius is smaller than the radius that one obtains when assuming that both effects happen one after another, i.e. first the repulsion radius $R_{rep}(t)$ is calculated and then inserted as initial radius into $R_{diff}(t)$ ¹. By using equations (4.24) and (4.19), this can be formulated as

$$\underbrace{\sqrt[3]{R_0^3 + \Delta R_{rep}(t)^3}}_{:=R_{low}(t)} < R_{diff,rep}(t) < \underbrace{\sqrt{(R_0^3 + \Delta R_{rep}(t)^3)^{\frac{2}{3}} + \sigma_{diff}(t)^2}}_{:=R_{up}(t)} . \quad (5.3)$$

The lower and upper limit for the real radius are defined as $R_{low}(t)$ and $R_{up}(t)$, respectively. They were plotted in figure 5.3 for alphas and betas of both 300 keV and 3 MeV. The colored lines

¹The order in which repulsion and diffusion are applied to the radius is not indifferent. The described order was used for the upper limit since it returns (slightly) higher values.

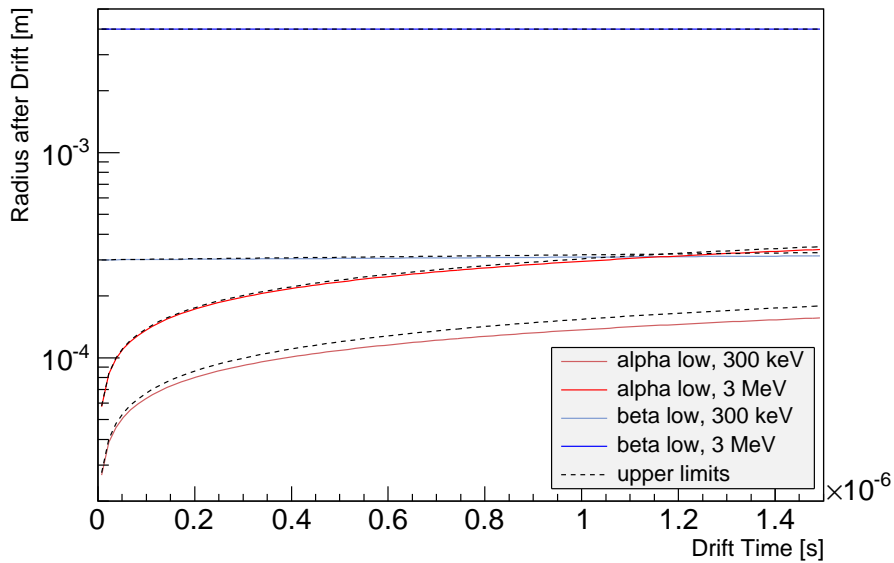


Figure 5.3: Lower and upper limit for the cloud radius plotted against the drift time. The graph shows $R_{low}(t)$ and $R_{up}(t)$ for alphas and betas of both 300 keV and 3 MeV on a logarithmic scale. The colored lines represent $R_{low}(t)$. For reasons of clarity, $R_{up}(t)$ is plotted as a black dashed line in each of the four cases, but can intuitively be assigned to a colored line.

represent $R_{low}(t)$. For reasons of clarity, $R_{up}(t)$ is plotted as a black dashed line in each of the four cases, but can intuitively be assigned to a colored line. The real radius, which should in each case lie somewhere between $R_{low}(t)$ and $R_{up}(t)$, does obviously not differ too much from $R_{low}(t)$. It can be concluded that for the considered drift times, particles and energy ranges the effect of thermal diffusion is practically negligible. In order to find a good balance between convenience and accuracy, it was therefore decided to implement the effect of electrostatic repulsion but to neglect thermal diffusion in the detector simulation.

The detector signal is dominated by the electron drift. With a view to the signal shaping, the most important aspect of repulsion is then the extension of the electron cloud in drift direction, i.e. parallel to z . The lateral extension has only minor contribution to the signal and is therefore not considered, neither is the hole repulsion. The enlargement in z is induced by a variation of the drift velocity of electron packages from different spots of energy deposition. The process is schematically illustrated in figure 5.4. First, the initial cloud radius R_0 is determined as half of the distance between the two outermost spots of energy deposition with regard to z . By doing so, the density profile of the cloud is not considered. A more precise approach could be e.g. the assumption of a Gaussian distributed cloud as basis of the size determination. However, the results of the used method give satisfying results, as can be seen in section 6.4.

Next, the mean drift time t is calculated from the average velocity v_0 given by equation (5.2) and the mean z position which is adequate to the mean distance to the anode plane. The number N of electrons is derived from the total deposited energy by means of equation (4.8). With the electron mobility μ_e , the vacuum permittivity ϵ_0 and the relative permittivity ϵ_r , the expected change in radius $\Delta R(t)$ can now be calculated as

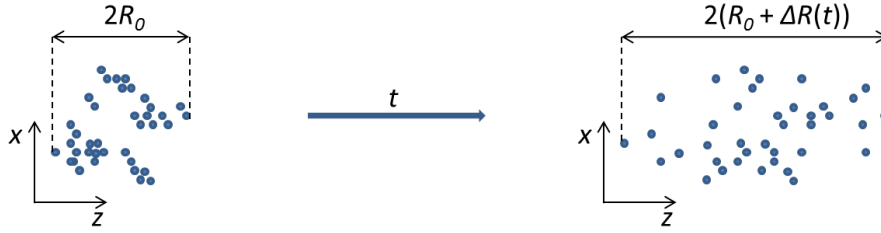


Figure 5.4: Illustration of the effective cloud enlargement. Blue dots represent electron packages. R_0 is determined as half of the distance between the two outermost spots of energy deposition with regard to z . t is calculated from the average velocity v_0 and the mean z position. These are used to determine the change in radius ΔR , which is realized by a variation of the velocity of electron packages from different spots of energy deposition.

$$\Delta R(t) = R_{rep}(t) - R_0 = \sqrt[3]{R_0^3 + \frac{3\mu_e N e t}{4\pi\epsilon_0\epsilon_r}} - R_0 \quad . \quad (5.4)$$

The drift velocities v_i of the individual electron packages are now set to be uniformly distributed within the interval

$$v_0 - \Delta v \leq v_i \leq v_0 + \Delta v \quad \text{with} \quad \Delta v = \frac{\Delta R}{t} \quad . \quad (5.5)$$

The result, as depicted in the scheme, is an effective stretching of the cloud in drift direction. By doing so, the fact that during the drift the enlargement follows the cube root of t , and not linearity, is ignored. After the full drift, the enlargement proportional to t results by definition in the same cloud size as an enlargement proportional to $\sqrt[3]{t}$. Before the end of the drift, the simulated cloud size is underestimated. Actually, this has no meaning at all for the signal. Since all single pulses from the individual carrier packages are summed up in the end, the important entity is the average velocity which does not change during the cloud enlargement. The crucial point is the end of the signal rise, which will get more smeared for a larger extension in z , independently of the former drift behavior.

If in the VENOM simulation all energy was deposited at one single spot, the drift velocity is set to v_0 without variation. At least some tens of energy spots have to be simulated to let the effect of cloud enlargement on the signal appear smooth. The threshold energy for an appropriate treatment of repulsion depends on the particle type. For alphas, enough spots of energy deposition are reached above 800 keV, for betas already at 100 keV.

On the basis of the predicted carrier track and drift velocity, the carrier position is calculated in drift time steps of $dt = 10$ ns and written to a vector. dt corresponds to the FADC sampling rate of 100 MHz.

5.1.3 Generating Signals

To calculate a signal, the weighting potential $\phi_w(\vec{r})$ for the corresponding electrode has to be known, see section 4.1.1. Therefore, a simulation with COMSOL Multiphysics was done for the

CA and NCA. The electric field in the detector was calculated with the respective anode set to 1 V while all other electrodes were grounded. The result was then stored in a three-dimensional ROOT histogram H_{ϕ_w} and can be used dimensionless as the weighting potential of this anode. $\phi_w(\vec{r})$ is independent of the actually applied voltages and accordingly it is sufficient to simulate it only once per anode for a given detector geometry.

The signal itself is generated as follows. For each carrier package i , the track is simulated and written to a vector $V_{track,i}$ as described above. The number of entries in $V_{track,i}$ is equal to the desired pulse duration times the sampling rate. For every position in $V_{track,i}$, the weighting potential is requested from H_{ϕ_w} and in turn written to a vector $V_{\phi_w,i}$. According to section 4.1.1, the amount of charge Q induced by a moving charge q is now given as the change in weighting potential along the track:

$$Q = -q\Delta\phi_w(\vec{r}) \quad . \quad (5.6)$$

To consider carrier trapping, the amount of charge in the package is reduced by a relative amount appropriate to the trapping time τ . The reduction of the initial charge q_0 after drift time t was introduced in section 4.2.2. For small time steps dt the approximation

$$\frac{q(dt)}{q_0} = \exp\left(\frac{-dt}{\tau}\right) \approx \left(1 - \frac{dt}{\tau}\right) \quad (5.7)$$

is valid. In this approach, charges are not considered as discrete but as a continuous quantity. This treatment is justified with the high number of carriers that account for the signal.

In section 4.1.3, it was explained how the mean electron trapping length λ is linked to the experimentally gained weighting factor w . λ is a dimensionless quantity which is relative to the detector length L . With the average carrier velocity v_0 given by equation (5.2) and the electron mobility μ_e , the trapping time for electrons can be approximated to be

$$\tau_e \approx \frac{\lambda L}{v_0} = \frac{\lambda L^2}{\mu_e(HV - GB/2)} \quad . \quad (5.8)$$

To obtain the trapping time for holes, accordingly the hole mobility μ_h and the mean trapping length ρ for holes need to be inserted.

With equation (5.6), the signal for a moving charge q can now be calculated, while q itself is a function of drift time, see equation (5.7). The initial amount of charge q_0 is set to be an arbitrary constant. The trapping time for electrons and holes can be controlled by the experimentally obtained values w and ρ , respectively. The calculated values for Q w.r.t. $V_{\phi_w,i}$ are written to a vector $V_{esig,i}$ or $V_{hsig,i}$ for electron or hole packages, respectively. Both signals are summed up to obtain the contribution of energy deposition E_i to the total signal, i.e. $V_{sig,i} = V_{esig,i} + V_{hsig,i}$. The total signal $V_{sig,tot}$ can then be built by adding up all contributions $V_{sig,i}$. The $V_{sig,i}$ are weighted by the energy E_i that was deposited at position i . This can be formulated as

$$V_{sig,tot} = \sum_i E_i V_{sig,i} \quad . \quad (5.9)$$

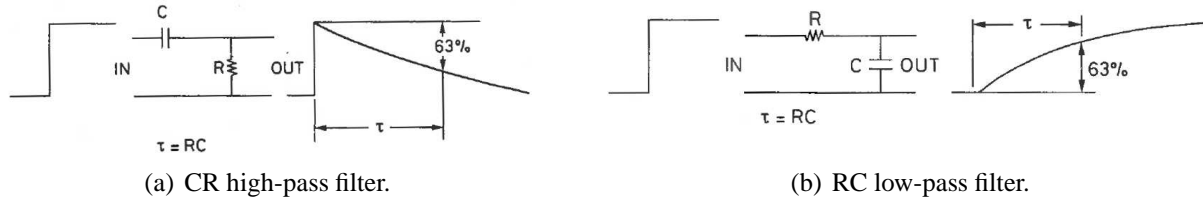


Figure 5.5: Analog frequency filters [Leo94b]. The basic circuits of a high-pass and a low-pass filter are shown as well as their effect on a step function input pulse.

$V_{sig,tot}$ is written to a vector with the same sampling rate as before.

5.1.4 Adding Impact of Electronics

Frequency Filters

Electric circuits consisting of resistors and capacitors can act as frequency filters. A signal is naturally composed of numerous sinusoidal components. By filtering out certain frequency ranges, the signal shape changes. Figure 5.5 (a) shows the basic connection of resistance R and capacitance C that leads to a high-pass filter. For a dot-like energy deposition in the crystal, the detector signal would ideally resemble a step function. The effect on such a curve is also illustrated. As can be seen, the filter acts only on the flat part of the pulse which is attenuated, whereas the signal rise remains unaffected. The fall-off of the post-baseline happens corresponding to the product of R and C which is referred to as fall time $\tau_{fall} = RC$. The attenuated frequencies f are below

$$f \leq \frac{1}{2\pi\tau_{fall}} . \quad (5.10)$$

Since the effect on the pulse is the electrical analog to a mathematical differentiation, the circuit is also called CR differentiator.

A low-pass filter is realized when in the circuit capacitance and resistance change places, see figure 5.5 (b). The effect on a step function is complementary: Now the signal rise is delayed while the flat level of the prior pulse is approached. Here, the characteristic time constant is called rise time $\tau_{rise} = RC$. The cut-off threshold for frequencies is

$$f \geq \frac{1}{2\pi\tau_{rise}} . \quad (5.11)$$

Due to the similarity to a mathematical integration, the filter is often called RC integrator. More on this can be found e.g. in [Leo94b].

In particle detection, frequency filters are consciously used to limit the bandwidth and to thereby reduce noise. Apart from that, the whole DAQ chain features numerous devices and wires, all of which carry intrinsic resistances and capacitances that can form RC and CR filters. At COBRA, an RC integrating circuit with $\tau_{rise} = 7$ ns is part of the preamplifiers. The contained feedback capacitor is discharged through a further resistor, leading to a preferably slow signal fall with

$\tau_{fall} = 140 \mu\text{s}$ [hp]. The commercial devices in the main amplifiers are reported to have a rise time of a few ns each [http, http]. The input stage of the FADC contains a 50 MHz low-pass filter in order to prevent aliasing² [Sch11]. According to equation (5.11) this corresponds to a rise time of 3.2 ns.

To implement a digital frequency filter, a discretized description of the related circuit has to be found. For the high-pass circuit, Kirchhoff's Laws and the definition of capacitance lead to

$$V_{out}(t) = I(t)R \quad , \quad (5.12)$$

and

$$I(t) = \frac{dQ}{dt} \quad , \quad \text{with} \quad Q(t) = C(V_{in}(t) - V_{out}(t)) \quad , \quad (5.13)$$

where V_{in} and V_{out} are the in- and outgoing voltage signals, respectively, I is the current and Q is the charge stored in the capacitor. Insertion of the relations from equation (5.13) into equation (5.12) yields

$$V_{out}(t) = RC \left(\frac{dV_{in}}{dt} - \frac{dV_{out}}{dt} \right) \quad . \quad (5.14)$$

In terms of discrete sequences (x_1, x_2, \dots, x_n) and (y_1, y_2, \dots, y_n) for the input and the output signal values, respectively, equation (5.14) reads

$$y_i = \tau_{fall} \left(\frac{x_i - x_{i-1}}{dt} - \frac{y_i - y_{i-1}}{dt} \right) = \alpha_{high} y_{i-1} + \alpha_{high} (x_i - x_{i-1}) \quad , \quad \text{with} \quad \alpha_{high} = \frac{\frac{\tau_{fall}}{dt}}{\frac{\tau_{fall}}{dt} + 1} \quad . \quad (5.15)$$

In case of the low-pass circuit, equations (5.12) and (5.13) have to be replaced by

$$V_{in}(t) - V_{out}(t) = I(t)R \quad , \quad (5.16)$$

and

$$I(t) = \frac{dQ}{dt} \quad , \quad \text{with} \quad Q(t) = CV_{out}(t) \quad , \quad (5.17)$$

which can conclusively be rearranged to give

$$V_{out}(t) = V_{in} - RC \frac{dV_{out}}{dt} \quad . \quad (5.18)$$

The equivalent for discrete samples is

²For signals sampled in time with frequency f , aliasing has the meaning that signals of frequency ν cannot be distinguished from signals with frequency $\nu + nf$ due to the Nyquist-Shannon sampling theorem, see e.g. [Wat00]. Therefore, the input signal needs to be limited to frequencies lower than $\frac{1}{2f}$.

Table 5.1: Detector input parameters for the depicted pulses, unless stated otherwise.

| Parameter | Value |
|---------------------------------|-------|
| HV [V] | 1000 |
| GB [V] | 50 |
| μ_e [cm ² /(Vs)] | 1000 |
| μ_h [cm ² /(Vs)] | 70 |
| w | 0.71 |
| ρ | 0.12 |
| τ_{rise} [ns] | 35 |
| τ_{fall} [μ s] | 140 |

$$y_i = x_i - \tau_{rise} \frac{y_i - y_{i-1}}{dt} = \alpha_{low} x_i + (1 - \alpha_{low}) y_{i-1}, \text{ with } \alpha_{low} = \frac{1}{\frac{\tau_{rise}}{dt} + 1}. \quad (5.19)$$

Equations (5.15) and (5.19) are used successively to apply a digital filtering process to the signals given by the incoming signal vector $V_{sig,tot}$. The time constants τ_{rise} and τ_{fall} have to be specified for that. The filtered signal is written to another vector $V_{sig,CR-RC}$.

Noise

Electronic noise can optionally be added as a fluctuation superimposed on the signal. The input noise level σ has to be set. For each entry of the filtered signal vector $V_{sig,CR-RC}$, the signal value x_i is recalculated as a random number from a Gaussian distribution around x_i with standard deviation σ . σ can be obtained e.g. by considering a real detector signal and determining the standard deviation of the residual distribution around the pre-baseline. Since the x_i have arbitrary units, σ has to be scaled internally w.r.t. a reference pulse height of the detector in question. The new signal values are again written to a vector $V_{sig,noise}$. If the noise option was chosen, $V_{sig,noise}$ is the final output signal of the detector simulation. Otherwise, $V_{sig,CR-RC}$ is returned.

5.2 Results

5.2.1 Pulse Samples

Several sample pulses were generated with the detector simulation to give an impression of its functionality. Unless stated otherwise, the used input parameters are those stated in table 5.1. Figure 5.6 (a) shows a simulated signal with (thin black line) and without (bold grey line) applied frequency filters. The slight attenuation of the post-baseline due to the high-pass filter becomes visible. The high time constant $\tau_{fall} = 140 \mu$ s was chosen in accordance with the declaration of the preamplifier chip.

The unfiltered signals show sharp bends between the different signal stages, namely at the point of divergence between CA and NCA signal and at the transitions into the post-baselines. Espe-

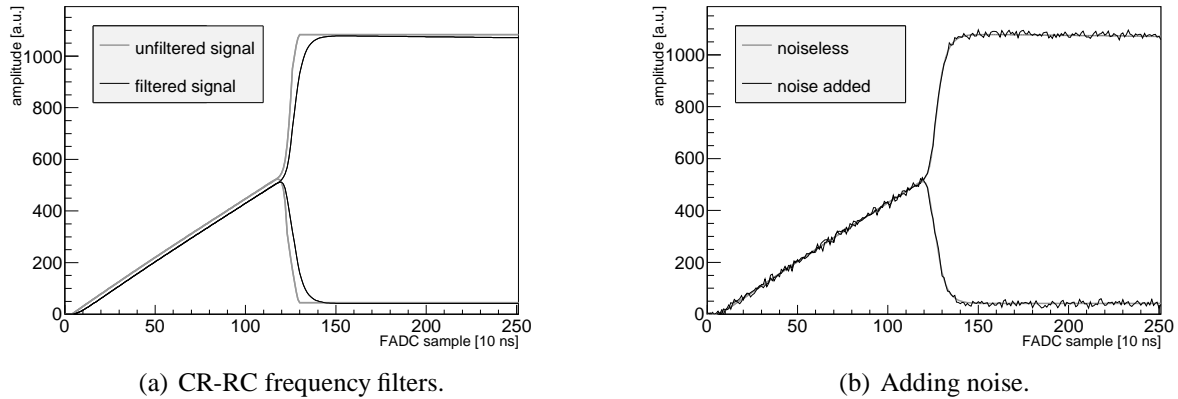


Figure 5.6: Impact of electronics on simulated pulses. Panel (a) shows a signal with and without applied frequency filter. Panel (b) shows the same signal with noise added.

cially the latter smooth out by applying the low-pass filter. The experimental pulses all show this retarded signal rise. In the course of the simulation development it was carefully inspected if the symptom actually arises from electronic signal transmission or already from charge transport in the crystal. Imaginable reasons for the latter case include deformations of the local electron mobility or the electric field in the near anode region. These might be due to surface effects or to the metal-semiconductor junctions. The results from field simulations show that such effects are far too short-ranged to possibly affect the pulse shapes, see section 4.3 in the previous chapter. Furthermore, pulses from the COBRA demonstrator were considered which were injected by the pulse generator. Like real detector signals, the injected pulses pass all elements of the readout chain. The same smooth transition to the post-baseline was observed, so the theory of an intrinsic crystal effect is most widely ruled out. Thus the reason for the slow rise originates from the electronic signal transmission and is most likely due to internal resistances and capacitances, see section 5.1.4. The chosen rise time of 35 ns was observed to be at the typical order of τ_{rise} values to fit experimental signals.

As explained above, it is possible to add noise to the simulated signal. Figure 5.6 (b) shows the filtered signal from panel (a) with the noise option chosen. The result resembles pretty much the experimental pulses.

To see how accurate the simulation actually is, real events from the COBRA demonstrator were picked and imitated by the detector simulation. No noise was added in order to clarify the guideline of the pulse. The simulated and the original pulses were plotted in the same frame. Figure 5.7 shows a typical result. The colored curves represent the experimental signals. The simulated counterparts are depicted with black lines. The chosen event was reconstructed to be a near cathode event with 2783 keV of deposited energy E_{dep} . The detector parameters match those in table 5.1. Since the output amplitude has arbitrary units, all simulated pulses were scaled w.r.t. the height of the CA signals.

The outcome has high agreement with the original pulses, especially from the point of CA and NCA signal divergence at sample #120 onwards. Striking features are the relative signal

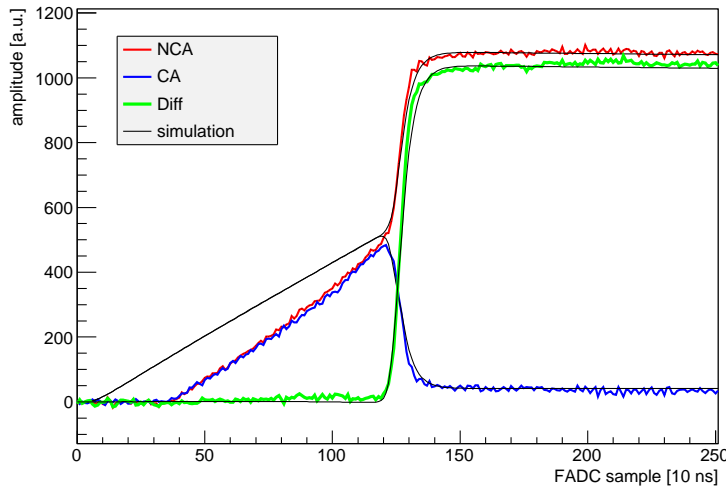


Figure 5.7: Simulated compared to experimental pulses with $E_{dep} = 2783$ keV. No noise was added for the sake of clarity. The colored curves represent the experimental signals. The simulated counterparts are depicted in black lines. All simulated pulses were scaled w.r.t. the pulse height of the CA signals. The straight slopes diverge between simulated and experimental signals.

height at this point, the subsequent curve bending and the fact that both NCA signals end up on the same post-baseline. A deviation occurs however in the steepness of the slope in the first part of the pulse and thus also in its length. The slow rise of the simulated signals can have several reasons, and most probably a mixture of those is applicable. It might for instance be that the assumed electron mobility is too low. It was presumed that the CZT composition is $\text{Cd}_{0.9}\text{Zn}_{0.1}\text{Te}$, but as can be concluded from the comparison of CZT and CdTe in table 3.2, μ_e is affected by the admixture of Zn. The actual Zn content in a detector is only vaguely known and can differ by up to 50 %. Another reason is the implemented detector size of $(1.09 \times 1.09 \times 1.09) \text{ cm}^3$. It is very likely that the detector in question is smaller and shows a steeper slope in the weighting potential.

An easy way to account for this mismatch was to artificially increment μ_e . A new simulation for the same event was carried out, now with an adapted electron mobility of $1.4 \cdot \mu_e$. The factor of 1.4 was only used to demonstrate which aspect of the simulation is responsible for the mismatch between simulated and measured pulse. In the later analyses, no adjustments of the mobility were made. The adaptation results in the pulses depicted in figure 5.8. Besides a large scale view in panel (a), a close-up of the region around CA and NCA signal divergence is shown in panel (b). Simulated and experimental signals are in very good agreement now and when noise was added to the simulation it would in fact be hard to tell them apart by eye.

The simulation was repeated for different events. The results all proved satisfactory, one of which is shown in figure 5.9. Although at a highly different energy of $E_{dep} = 255$ keV, the curves are still in accordance. Two things can be learned from that. First and foremost, the detector simulation returns pulses of great accuracy throughout the important energy range between 0 and 3 MeV. Furthermore, the adapted parameters τ_{rise} , τ_{fall} and the counterbalancing incremented electron mobility appear to be invariant for different energies and interaction depths

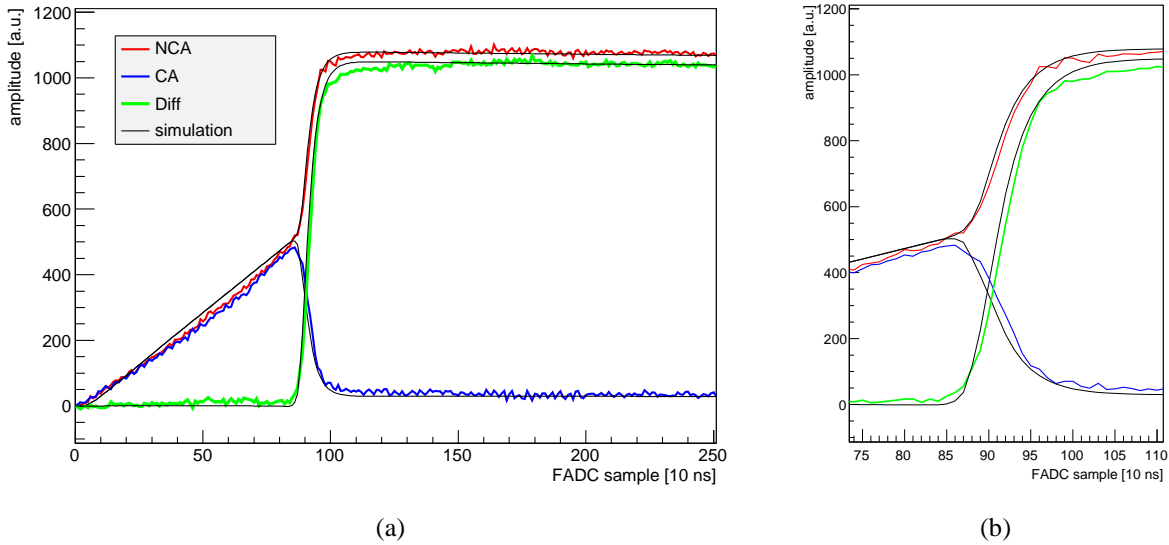


Figure 5.8: Simulated compared to experimental pulses with $E_{dep} = 2783$ keV. μ_e was multiplied by a factor of 1.4 to reach an optimal fit. A close-up of the divergent region is shown in panel (b).

in one particular detector. For the discussed long slope this means that it can be assumed to be a systematic but constant error. It should be mentioned that pulses with a manipulated μ_e can be used for pulse shape analysis only to a limited extent, since features like e.g. the rise of the difference signal might be distorted. If the slope itself for a specific detector should be the feature of interest, the weighting potential would have to be recalculated.

Another aspect to test the quality of the detector simulation is the study of lateral surface events. In section 4.1.2 it was described how deformations of the weighting potential towards the lateral surfaces lead to a dipping of the difference pulse below the pre-baseline level (DIP event) or to an early rise phase (ERT (= early rise time) event) before rising sharply toward the post-baseline. The behavior is distinctive for an event on an NCA or CA detector side, respectively. Both features are reproduced by the simulation as can be seen in figures 5.10 (a) and (b).

5.2.2 Energy Resolution

The detector simulation was used to determine a theoretical energy resolution. For real detectors, a common method is to measure the width of the 662 keV photopeak from the transition



Correspondingly, a ^{137}Cs source was simulated with VENOM. The detector parameters needed as input were chosen in accordance with specific detectors from the demonstrator setup which can be identified by their layer number and position. For the chosen detectors, pulses were simulated for 50 000 events. From these, the deposited energies were calculated. A reconstructed energy spectrum can be seen in the right panel of figure 5.11, together with the discrete energy distribution obtained from the VENOM simulation in the left one. The energy resolution

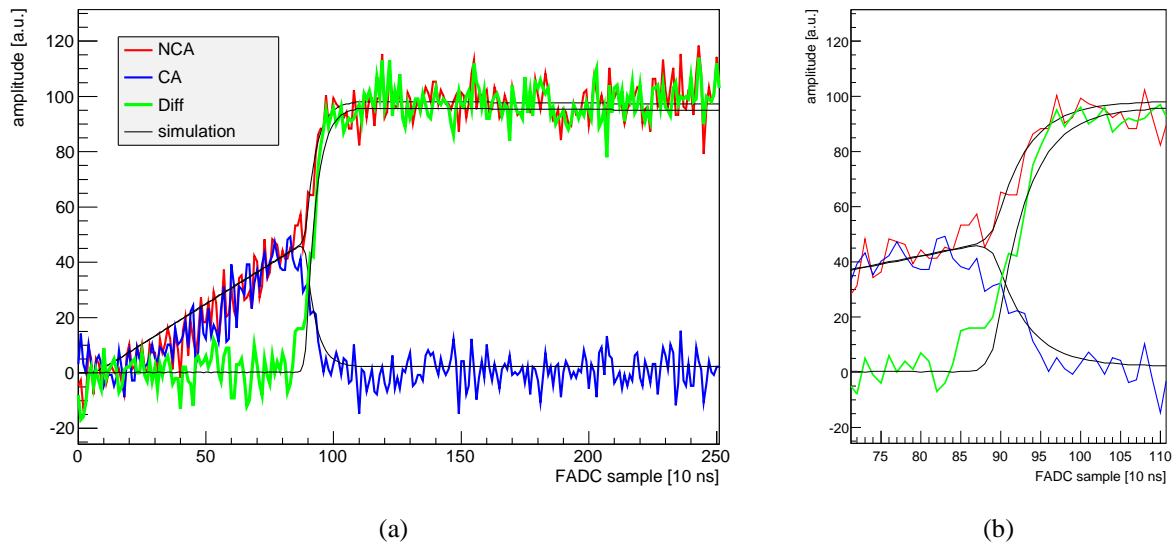


Figure 5.9: Simulated compared to experimental pulses with $E_{dep} = 255$ keV. μ_e was multiplied by a factor of 1.4 to reach an optimal fit. A close-up of the divergent region is shown in panel (b). τ_{rise} and τ_{fall} seem not to vary for different energies.

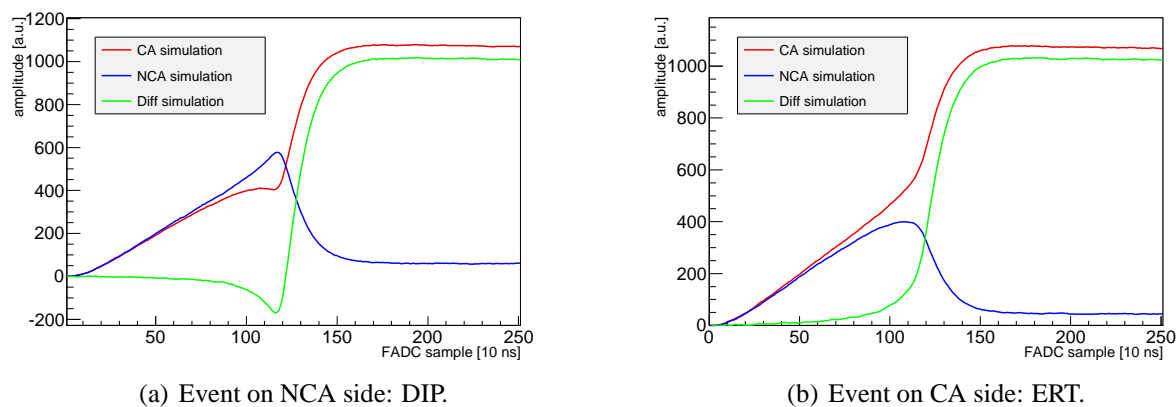


Figure 5.10: Simulated pulses for lateral side events. The characteristic DIP and ERT features are reproduced well by the simulation.

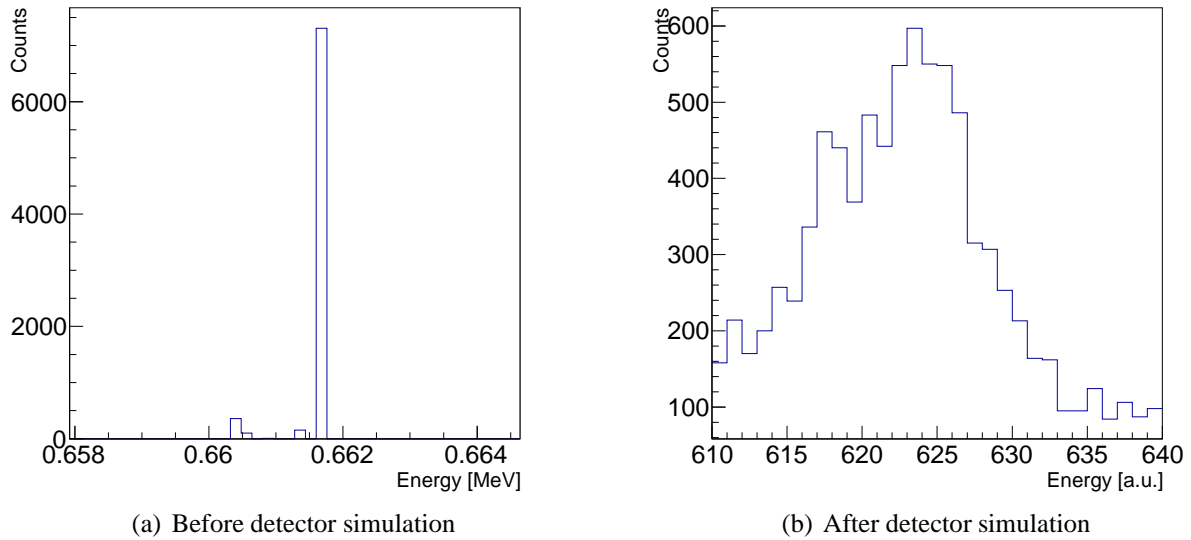


Figure 5.11: Reconstructed energy spectrum from simulated ^{137}Cs decay in detector 7, before and after applying the detector simulation. The FWHM of the photopeak at 662 keV was used to determine the energy resolution of the detector simulation. In the depicted example, the FWHM is 12 samples at peak position 623.5, leading to an energy resolution of 1.92 %.

Table 5.2: Energy resolutions obtained from the detector simulation. Experimentally observed values were taken from [Zat14].

| Layer | Position | HV [V] | GB [V] | w | ΔE_{exp} @ 662 keV [%] | ΔE_{sim} @ 662 keV [%] |
|-------|----------|--------|--------|------|--------------------------------|--------------------------------|
| 1 | 5 | 900 | 60 | 0.90 | 2.65 | 1.93 |
| 1 | 6 | 1200 | 70 | 0.95 | 2.38 | 1.89 |
| 1 | 7 | 1200 | 80 | 0.91 | 3.21 | 1.92 |

was defined as the full width at half maximum (FWHM) of the photopeak divided by the peak position. The obtained values ΔE_{sim} are presented in table 5.2 together with experimentally observed resolutions ΔE_{exp} .

The simulated resolutions lie between 1.89 % and 1.93 %. They are very close to each other and in fact not far from the experimental values, coming from the range between 2.38 % and 3.21 % and thus being a little higher than in the simulation. The relative ordering, however, is not reproduced: A better simulated resolution is not necessarily correlated with a better behavior in the laboratory. It can be concluded that the actual resolution is influenced strongly by individual crystal defects and inhomogeneities that are not explicitly part of the simulation. These tend to interfere charge transport and lead to a worse resolution.

5.3 Discussion

The presented detector simulation has proven to be a functional tool to produce realistic pulse shapes. It was designed from the perspectives of accuracy, speed and flexibility. The electric field predefined by the electrode biases was considered static. In terms of an acceptable process-

ing time, the stepwise numerical solution of a differential equation to describe charge transport phenomena was prohibitive. An approximation was used in form of an analytical description. Thus, the charge cloud was treated as a whole instead of calculating the direct impact of neighboring spots of energy deposition on each other. An alternative approach was to solve an adjoint carrier continuity equation, as described in [Pre99]. A further compromise was made in order to keep things flexible. Since all COBRA detectors are operated with individual voltage settings, a simplified electric field distribution was assumed, so that the electronic potential does not have to be simulated every so often but can easily be adjusted.

The adaptability and the consideration of all major charge transport aspects open up a wide range of applications. Pulses are calculated from arbitrary initial energy distributions which can previously be generated with the VENOM framework. Also the lateral side features DIP and ERT are taken into account. This allows for efficiency calculations for cuts based on pulse shapes, e.g. the alpha cut which will be presented in the following chapter, or the multi-site event cut.

While charge carrier trapping has been considered, detrapping has not. If it should turn out that the detrapping times are in fact considerably shorter than formerly expected, it is straightforward to implement an equivalent line in the code. The density of carrier traps was assumed to be constant. A decreasing trapping time towards the crystal surfaces would lead to a more realistic treatment.

An aspect that has been ignored so far is the possible loss of charge carriers in dead detector layers and charge sharing between CA and NCA. For a consideration the simplified assumption of a constant electric field in the crystal has to be replaced by appropriate field simulations. These can be produced for example with the COMSOL Multiphysics software, which allows for the consideration of boundary effects and junctions. For every point along the carrier track the components of the velocity vector can then be calculated in accordance with the field vector at the current location. The basic procedure was successfully tested with COMSOL fields throughout the simulation development.

Another possible reason for charge loss is the lateral extension of charge clouds due to thermal diffusion and electrostatic repulsion, which has not been implemented yet. So far, only the spread in drift direction is considered by a variation of the carrier velocities. As for the movement in z direction, also the lateral components can be varied to meet the desired extension of the cloud.

Chapter 6

Development of an Alpha Discrimination Cut

Towards a large-scale COBRA setup, background reduction is the most crucial issue in reaching the desired half-life sensitivity. As pointed out in section 3.2, it is mostly alphas from primordial decay chains that penetrate the detectors – thus their removal would mean a large step forward for the experiment. So far, the identification of incident particles is very limited. It is possible, for instance, to use pulse shape analyses to recognize multi-site events, which originate most likely from γ -interactions. The only way to vaguely recognize alpha induced events is to assign them to striking features in the energetic spectrum or the spatial event distribution.

A more efficient alpha discrimination has to be built on a characteristic of the alpha detection. The size of the generated charge carrier cloud is such an outstanding property. In section 4.2.1 it was demonstrated that alphas with energies up to several MeV do not travel further than $10\ \mu\text{m}$ in CZT, while betas cover up to mm distances. This should lead to an extended charge collection time for betas and could in principle be visible in the pulse shape.

Unfortunately, the initial difference in cloud size is counteracted by drift effects. Thermal diffusion and electrostatic repulsion account for the fact that during the drift clouds from alphas and betas become more and more alike. In section 5.1.2, it was depicted how alpha clouds can gain more than one magnitude in radius on their way to the anodes. On the basis of simulated particle ranges for alphas and betas in CZT (see section 4.2.1) and the analytic approximation for the cloud extension due to electrostatic repulsion given by equation (4.24), the cloud radius after maximum drift time was plotted for alphas and betas as a function of the particle energy. Thermal diffusion was not taken into account, but as figured out in section 5.1.2, electrostatic repulsion is the dominant drift effect for the considered energies and drift times. The plot is shown in figure 6.1. A red and a blue curve represent alpha and beta radii, respectively. For low energies, both curves run alongside each other and only at several hundred keV they drift apart. The radius uncertainties, taking into account the RMS values of the initial radius distributions, were calculated via error propagation and are shown as light colored bands. Since the alpha curve is dominated by the drift effect, the error band is not visible. The beta cloud

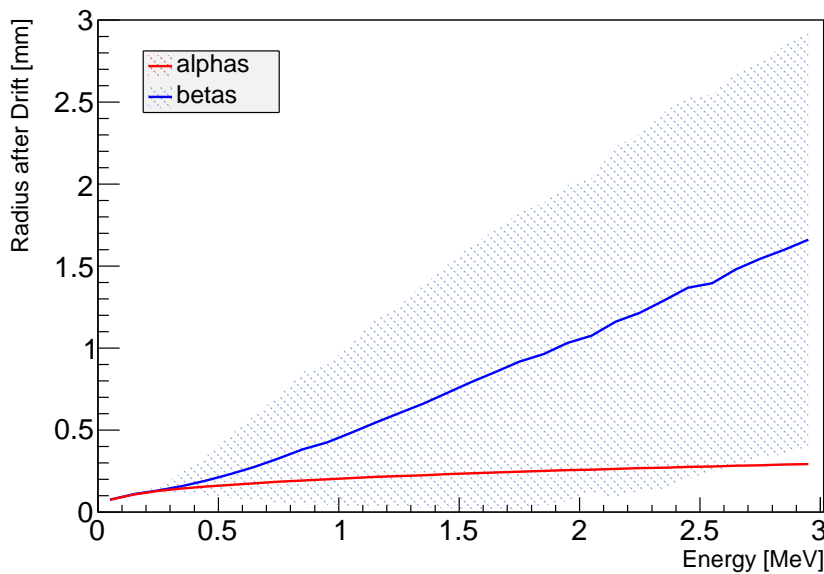


Figure 6.1: Cloud radius after drift plotted against particle energy. Thermal diffusion was not considered. A red and a blue curve represent alpha and beta radii, respectively. Uncertainties, calculated from the RMS values of the initial radius distributions, are drawn as light colored bands.

however is mainly determined by the size of the original cloud which is highly variable, see figure 4.5. The large uncertainty band overlaps the alpha curve throughout most of the plotted range. Conclusively, even for an ideal detector the distinction between alpha and beta clouds would be possible only above a certain energy threshold, and the cut efficiency is expected to rise with the particle energy.

This chapter investigates the potential of a possible alpha discrimination based on pulse shape analyses. The above considerations are used to define simple cut criteria. These are then applied to measured and simulated signals to determine cut efficiencies. In the end the results and further measures are discussed.

6.1 Definition of Cut Parameters

For an alpha discrimination via pulse shape analysis, signal characteristics must be found and translated into suitable parameters that can easily be compared. Afterwards, cut criteria can be defined.

The discrimination is based on the fact that alphas leave very compressed charge clouds in the crystal. Due to the almost immediate generation of all electron-hole pairs, and the constantly rising weighting potential in the crystal bulk, the size of the charge cloud does not affect the pulse shapes until the drifting electrons enter the near anode region. Figure 6.2 shows very simple signal sketches to understand the major consequences for the pulses. In panel (a) a constant dot-like charge distribution in the crystal is assumed, or a single electron, analogously. The detector would give a signal featuring very sharp bends at the point of CA and NCA signal divergence, and again at the transition into the post-baseline. For wide charge distributions, as

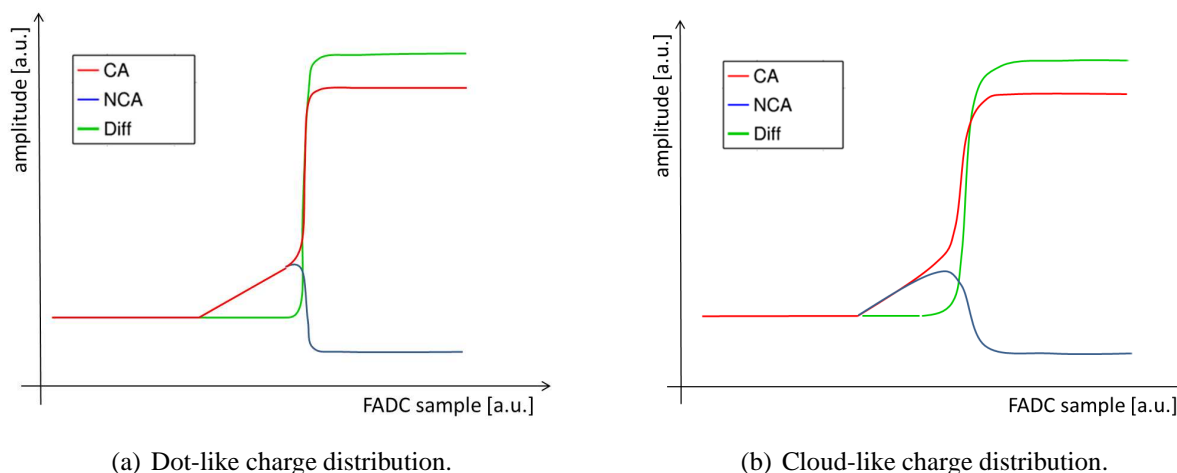


Figure 6.2: Signal schemes for different initial charge distributions.

assumed in panel (b), the electrons start the collection phase one after the other. The resulting signal is a superposition of single electron pulses with the shape from panel (a), shifted slightly on the time axis according to their delayed arrivals. The sharp bends smooth out and the steep slope towards the post-baseline gets shallower. Subsequently, the process of charge collection takes longer and so does the signal rise.

Although the discussed properties hold also for the CA and NCA signal, only the difference signal is considered for further analyses. Since the CA and NCA curves bend in opposite direction at the positions of interest, the studied effect should be more distinctive in the difference signal. Its dependence on the interaction depth is lower since the constant slopes at the beginning of CA and NCA signal cancel each other. The same principle leads to a reduction of simultaneous electronic signal distortions.

Considering the difference signal, three characteristic parameters can now be derived from the given assumptions.

- (1) The maximum height of the pulse derivative is a measure for the signal rise towards the post-baseline.
- (2) The full width at half-maximum (FWHM) of the pulse derivative is linked to the duration of charge collection.
- (3) The maximum height of the second pulse derivative characterizes the upward bend of the signal.

One could argue that the minimum height of the second pulse derivative could serve as an additional parameter, marking the transition into the post-baseline. But since this signal region is most significantly shaped by the delayed signal rise due to readout electronics, see section 5.2.1, the maximum height turned out the better choice.

Parameters (1) through (3) now allow to compare difference signals from known alpha and beta events – on condition that they were acquired with the same detector, since operational settings and individual intrinsic properties influence the values decisively. The parameters are expected

to be correlated: The integral over the first derivative is proportional to the energy, and thus a higher maximum value (parameter (1)) is connected with a steep rise (parameter (3)) and a small width (parameter (2)) of the derivative.

When the signal parameters are well studied, cut criteria can be defined.

6.2 Pulse Smoothing and Differentiation

Electronic noise causes high frequent wiggling around the baseline and thus signal differentiation always needs to go along with signal smoothing. In the course of this thesis, two different smoothing techniques have been tested on their performance in alpha discrimination.

6.2.1 Mean Value Method

A simple way to smooth a pulse given by a discrete sequence (x_1, x_2, \dots, x_n) is to build a sequence (y_1, y_2, \dots, y_n) from mean values of $2m + 1$ neighboring samples, i.e.

$$y_i = \frac{1}{2m + 1} \sum_{i-m}^{i+m} x_i \quad , \quad (6.1)$$

where the integer m controls the degree of smoothing. The derivative sequence $(y'_1, y'_2, \dots, y'_n)$ is given by

$$y'_i = y_{i+1} - y_i \quad . \quad (6.2)$$

Insertion of equation (6.1) yields

$$y'_i = \frac{1}{2m + 1} \left(\sum_{i-m+1}^{i+m+1} x_i - \sum_{i-m}^{i+m} x_i \right) = \frac{1}{2m + 1} (x_{i+m+1} - x_{i-m}) \quad . \quad (6.3)$$

For the analysis in this chapter, $m = 2$ was observed to yield satisfactory results.

6.2.2 Whittaker-Henderson Method

A more complex smoothing method is based on the attempt to use a generalized least-squares solution to find a good balance between smoothness and precision to the measured data. Although the idea goes back until the late 19th century, it is usually associated with the work done by E.T. Whittaker [Whi23] and R. Henderson [Hen24] in the 1920s. The idea is to find a sequence (y_1, y_2, \dots, y_n) for a measured sequence (x_1, x_2, \dots, x_n) that minimizes

$$\lambda \sum_{j=1}^n (x_j - y_j)^2 + \sum_{j=1}^{n-p} (\Delta^p y_j)^2 \quad . \quad (6.4)$$

Here, Δy_j describes the forward difference

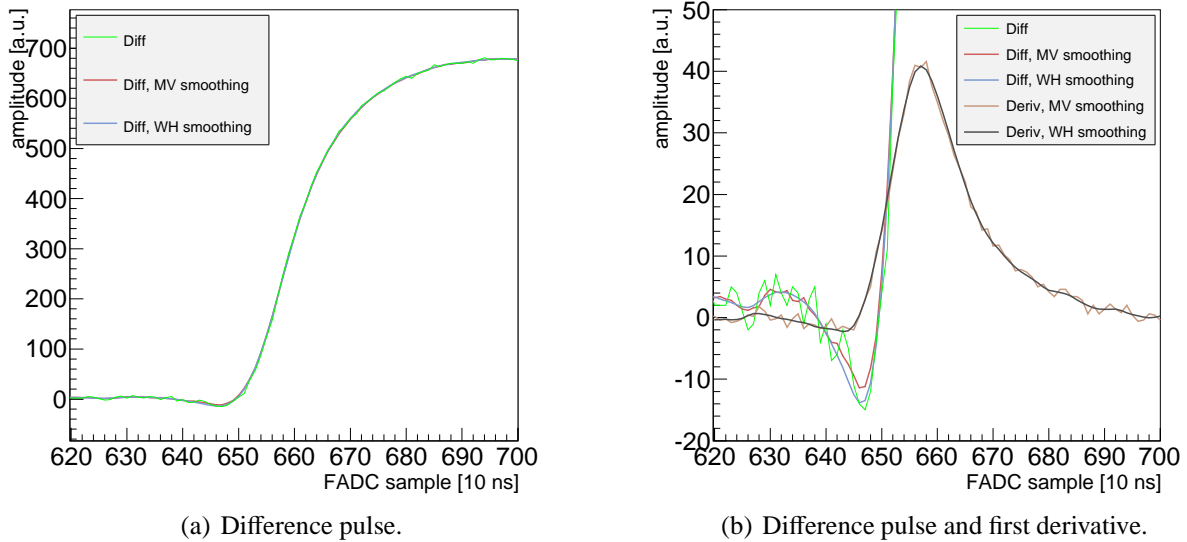


Figure 6.3: Sample pulse to demonstrate mean value (MV) and Whittaker-Henderson (WH) smoothing.

$$\Delta y_j = y_{j+1} - y_j \quad , \quad \text{where} \quad (6.5)$$

$$\Delta^2 y_j = \Delta(\Delta y_j) = \underbrace{(y_{j+2} - y_{j+1})}_{\Delta y_{j+1}} - \underbrace{(y_{j+1} - y_j)}_{\Delta y_j} \quad ,$$

and so on. The degree of smoothing is controlled by the positive real number λ and the integer $p < n$. The first sum of expression (6.4) is the least-squares term in order to stick to the original data. For $\lambda \rightarrow \infty$, the solution is identical to the measured sequence. The second term is a polynomial of degree $p - 1$, considering the deviation between neighboring sample values.

The parameters λ and p can be optimized automatically for a given measurement sequence. An efficient algorithm to compute both the control parameters and the estimates (y_1, y_2, \dots, y_n) for the smoothed pulse is presented in [Wei06]. The proposed implementation was adapted for the use in C++. For differentiation, equation (6.2) was used.

Figure 6.3 demonstrates the smoothing of a difference pulse with both methods, mean value (MV) and Whittaker-Henderson (WH). Panel (a) shows the rising part of the pulse. The smoothed curves stay close to the original signal. A close-up of the same region is given in panel (b). Here, the baseline noise of the original signal is visible. The fact that smoothing reduces baseline noise while the slight DIP-feature is not lost is a sign of quality for both smoothing techniques. The depicted first derivatives show that the degree of smoothing is higher when using the WH method.

Table 6.1: Detector parameters for measurements with alpha and beta sources.

| HV [V] | GB [V] | w |
|--------|--------|-------|
| 1000 | 50 | 0.609 |

Table 6.2: Q-values of utilized alpha and beta sources [hn].

| source element | ²³⁹ Pu | ²⁴¹ Am | ²⁴⁴ Cm | ⁹⁰ Sr | ⁹⁰ Y |
|----------------|-------------------|-------------------|-------------------|------------------|-----------------|
| Q-value [MeV] | 5.244 | 5.638 | 5.902 | 0.546 | 2.279 |

6.3 Test with Laboratory Measurements

6.3.1 Setup

The potential of the discrimination parameters was tested with data from specific laboratory measurements. These were done by D. Gehre at TU Dresden. A $(1 \times 1 \times 1) \text{ cm}^3$ CZT detector of CPG type was used with a readout chain comparable to the setup at LNGS. The applied voltages and the weighting factor are given in table 6.1. The detector was in turn irradiated with α - and β -particles from the cathode side. To cover a wider energy range, a combination of ²³⁹Pu, ²⁴¹Am and ²⁴⁴Cm was used as alpha source. The opening in the sample holder served as collimator. The beta source contained ⁹⁰Sr and ⁹⁰Y. The betas were collimated by a drill-hole in the 3 mm thick mounting plate.

The Q-values of all source elements are shown in table 6.2. It can be seen that the decay energy for the alpha sources is much higher than for the beta sources. In order to study events in the same energy range, the alpha source was installed 4 cm away from the target. In doing so, the alphas were slowed down by the surrounding air and the cathode before entering the fiducial detector volume. The energies were thus shifted to better match the beta spectrum. The shift is visible in the energy spectra depicted in figure 6.4. The beta source was placed in 6 cm distance to the cathode. This was necessary in order to not overstrain the DAQ system with the high source activity of 72 kBq.

A total of 10^5 events was acquired for each particle type. The analyzed particle energies range from 0 to 2 MeV.

6.3.2 Pulse Shape Analysis

For the pulse shape analysis, all acquired events with reconstructed interaction depths $0.95 < z < 1.05$ were taken into account. All other events can be considered either wrongly reconstructed or to come from other detector areas than the cathode.

For each of the remaining events, the difference pulse was smoothed and differentiated. Then, parameters (1) through (3) from section 6.1 were determined. Since all three parameters are expected to show energy dependence, and, moreover, energy dependent efficiencies need to be calculated, the events were subdivided into energy intervals of 100 keV before being filled into ROOT histograms, so that parameter values from events within one interval share a histogram.

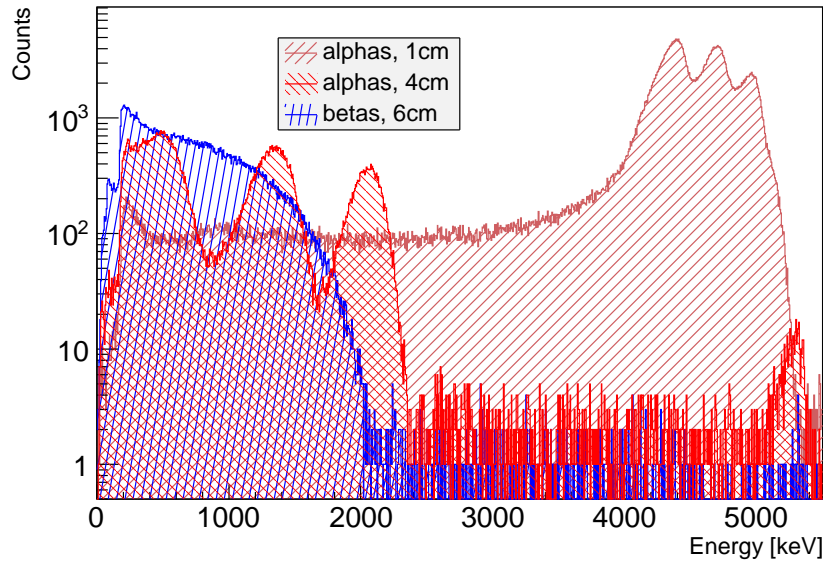


Figure 6.4: Energy spectra of measurements with alpha and beta source. The alpha spectrum was shifted through a larger distance to the target to better match the beta spectrum.

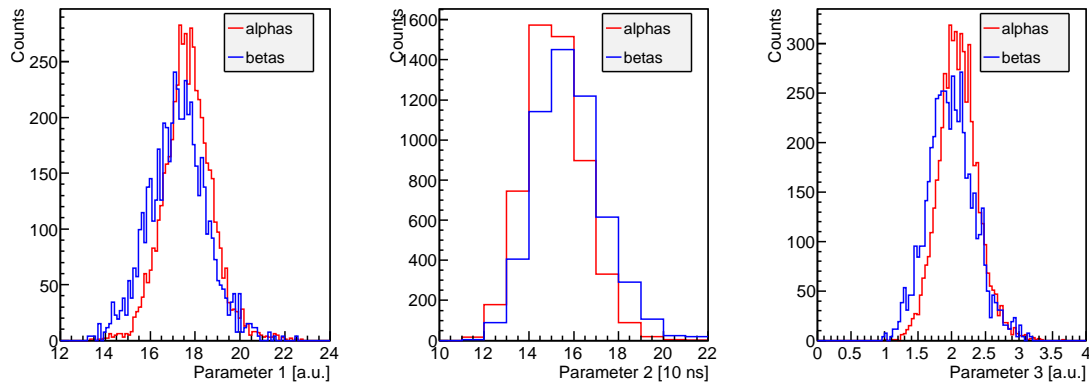


Figure 6.5: Parameter values for events with $1.4 \text{ MeV} < E_{dep} < 1.5 \text{ MeV}$. The beta distributions were scaled to make the comparison to the alphas easier. The values of parameters (1) and (3) tend to be higher for alphas than for betas. For parameter (2) it is vice versa.

For 3 parameters and an energy range from 0 to 2 MeV this results in a total of 3×20 histograms. The histograms for deposited energies E_{dep} between 1.4 MeV and 1.5 MeV are given as examples in figure 6.5. Red distributions represent alphas, blue distributions denote betas. The beta distributions were scaled to make the comparison to the alphas easier. Just as expected, the values of parameters (1) and (3), defined as the maximum height of the first and second derivative, respectively, tend to be higher for alphas than for betas. For parameter (2) on the other hand, given as the FWHM of the first derivative, it is vice versa. Nevertheless, in all cases the distributions show a large overlap.

The next step towards a discrimination is to use the obtained parameter distributions to define cut values. Two approaches were adopted.

- (i) Constant alpha ratio: The requirement is that all events from the median value of

the alpha distribution onwards are treated as alpha-induced – or downwards in case of parameter (2). This should flag 50 % of all alphas as such while a higher ratio of betas would remain untouched.

- (ii) Constant beta ratio: This approach requires a constant ratio of surviving betas which was set to 90 %. The integral over the beta distribution is built until the critical benchmark is reached. Just as before, the direction of integration depends on the parameter. From there on, all events are flagged as alphas. By doing so, more than 10 % of the alphas should be flagged correctly, while 90 % of the betas remain untouched.

The methods are in the following referred to as approaches (i) and (ii). The cut values for both approaches and all considered energy intervals are depicted in figure 6.6 using the example of MV smoothing. The error bars refer to statistical uncertainties. Parameters (1) and (3) show an almost linear energy dependence.

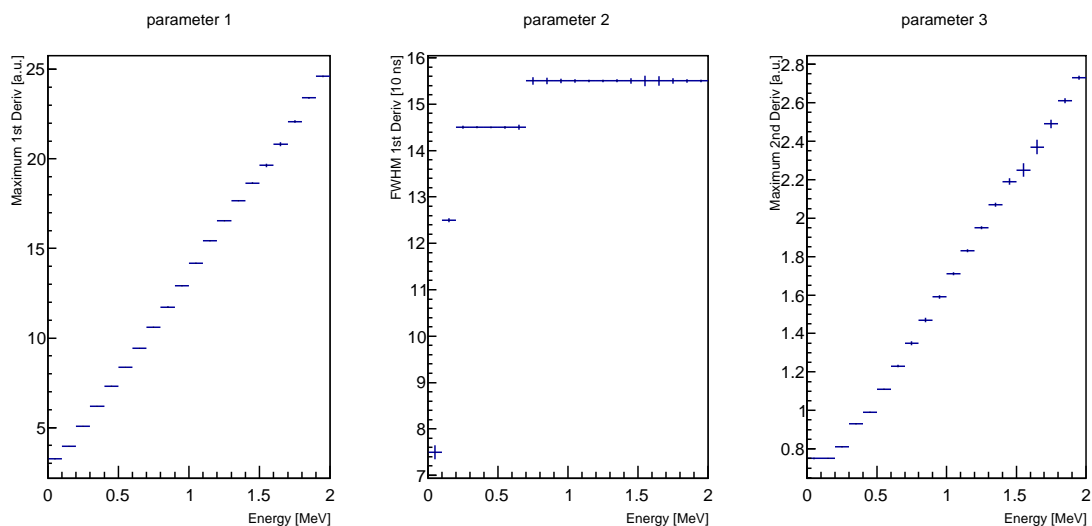
Based on the cut values, cut criteria can be formulated. The simplest method is to consider parameters (1) through (3) individually and cut off the alpha-flagged events. The percentage of surviving events is plotted in figure 6.7 for all considered energy intervals. A distinction was made between results from the MV and WH smoothing methods as well as for the approaches (i) and (ii). Again, the red and blue marks belong to alphas and betas, respectively. The error bars refer to statistical uncertainties. The uncertainties rise for betas towards higher energies since less events are available here, compare figure 6.4.

Panels (a) and (b) show the results for the requirement of a constant alpha ratio (approach (i)). Accordingly, the alpha ratios fluctuate around 50 %. At the same time, the amount of surviving betas is higher for almost every energy interval. Furthermore, the beta ratios rise with particle energy. Near 2 MeV, they exceed the alpha values by about 30 percentage points.

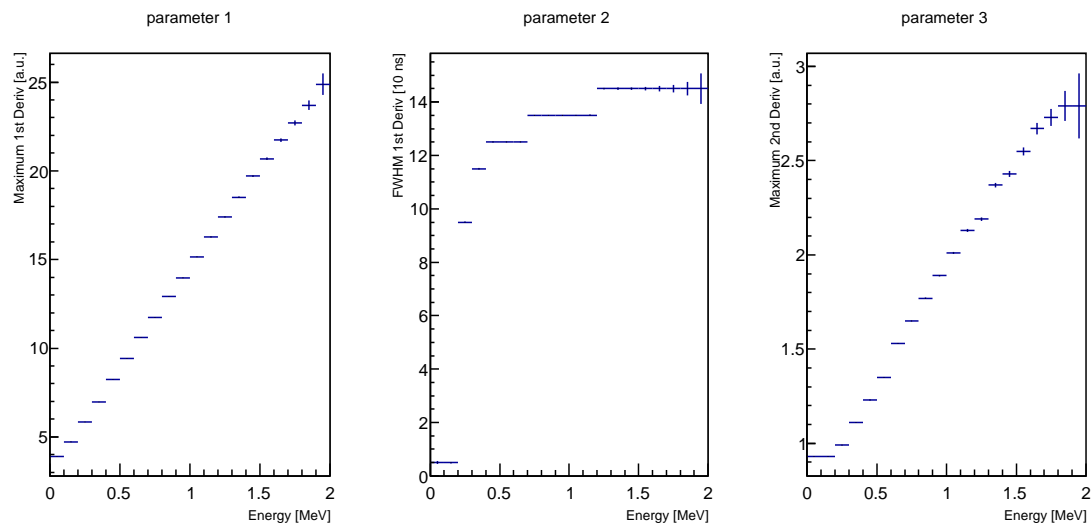
Irregularities arise for parameter (2). Occasionally, the alpha and beta ratios show an immediate rise or drop-off. This happens simultaneously and in correlation with changes in the cut value. The reason is that the FWHM values were determined to be integers. As can be seen in figure 6.5, they are distributed over a small range, so that a change in the cut value can have a large impact on the amount of affected events. A more consistent result could be achieved with a more complex method to determine the FWHM, e.g. a Gaussian fit to the signal derivative.

For parameters (1) and (3), the comparison between the two smoothing methods shows only minor differences. The different patterns at parameter (2) are again due to the rough binning during the parameter determination.

The results for a constant beta ratio (approach (ii)) are depicted in panels (c) and (d). While the relative amount of surviving betas is held at about 90 %, the alpha ratio starts to decrease around 1 MeV. Near 2 MeV it has dropped to values between 50 % and 70 %. Immediate drops and rises can again be observed for parameter (2).

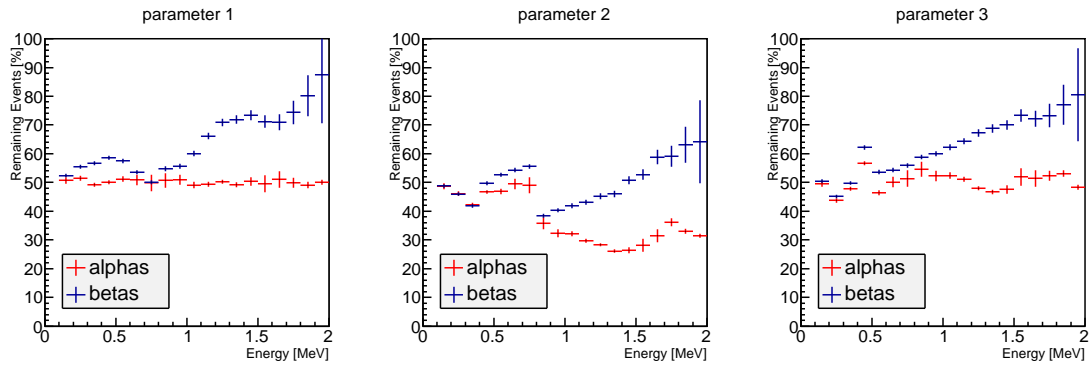


(a) MV smoothing, approach (i): constant alpha ratio of 50 %.

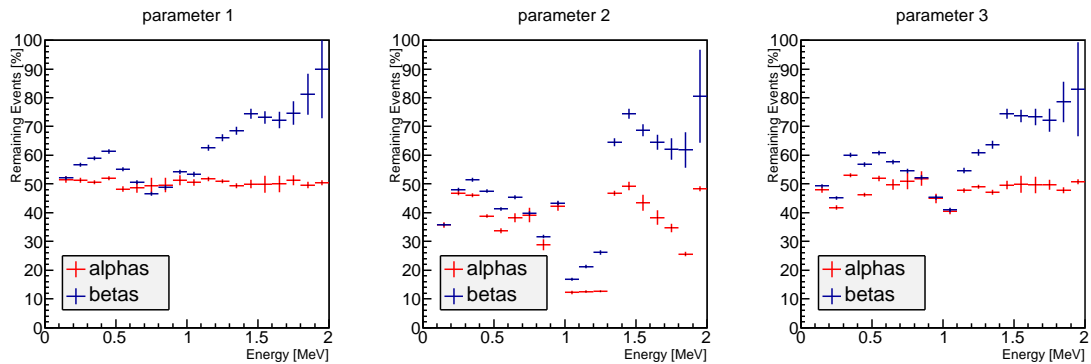


(b) MV smoothing, approach (ii): constant beta ratio of 90 %.

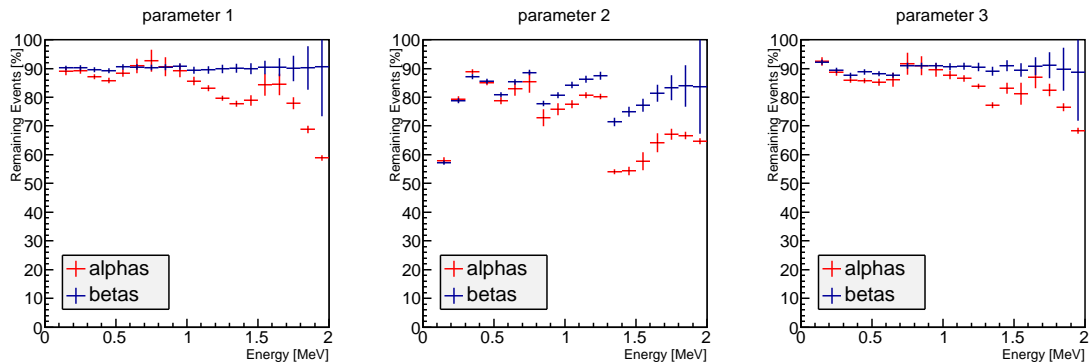
Figure 6.6: Cut values for the considered energy intervals. Parameters (1) and (3) show an almost linear energy dependence. The error bars refer to statistical uncertainties.



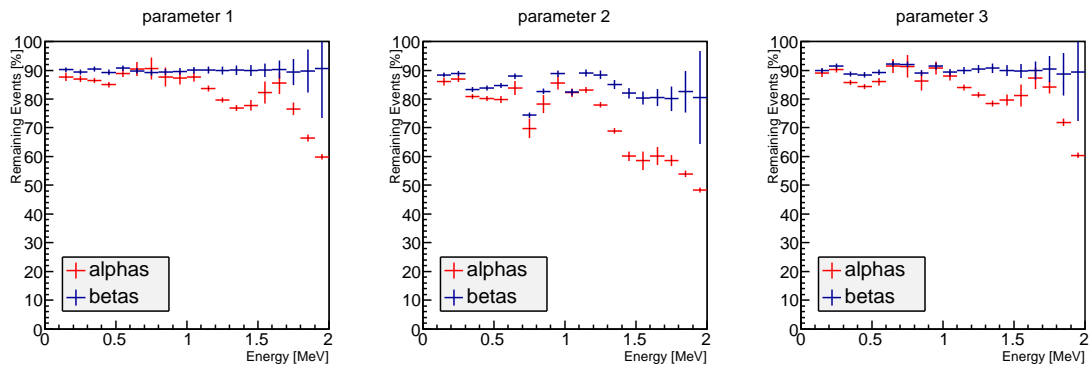
(a) MV smoothing, approach (i): constant alpha ratio of 50 %, single parameter cuts.



(b) WH smoothing, approach (i): constant alpha ratio of 50 %, single parameter cuts.



(c) MV smoothing, approach (ii): constant beta ratio of 90 %, single parameter cuts.



(d) WH smoothing, approach (ii): constant beta ratio of 90 %, single parameter cuts.

Figure 6.7: Results of alpha discrimination with laboratory measurements. The plots show the percentage of surviving events after the cut for all considered energy intervals. The cut parameters were considered individually. The error bars refer to statistical uncertainties.

Another strategy to define cut criteria is the combination of different parameters. The following cuts were built on the conditions that for the survival of an event at least 1, 2, or even all 3 parameters must hint at an incident beta. The results are depicted in figure 6.8. The histograms are titled *combine cuts 1* through 3, respectively. Case (a) is based on MV smoothing and demands a constant alpha ratio (approach (i)). The first two cut combinations are more cautious than the third, by which the alphas can be reduced to about 20 %, while up to 60 % of the betas survive. For WH smoothing, case (b), the pattern is less steady due to the fluctuations in connection with parameter (2). Nevertheless, with the third cut combination about 70 % betas survive compared to only about 35 % alphas at high energies.

The cuts with a constant beta ratio (approach (ii)) yielded very similar results for MV (c) and WH (d) smoothing. Here, the most radical cut eliminates only 20 – 30 % of all betas but three times as much alphas near 2 MeV.

The correlation between the three parameters can be visualized with scatter plots in which the values for different parameters are drawn against each other. Figure 6.9 shows such plots for events with $1.4 \text{ MeV} < E_{dep} < 1.5 \text{ MeV}$. The correlations appear as diagonal structures.

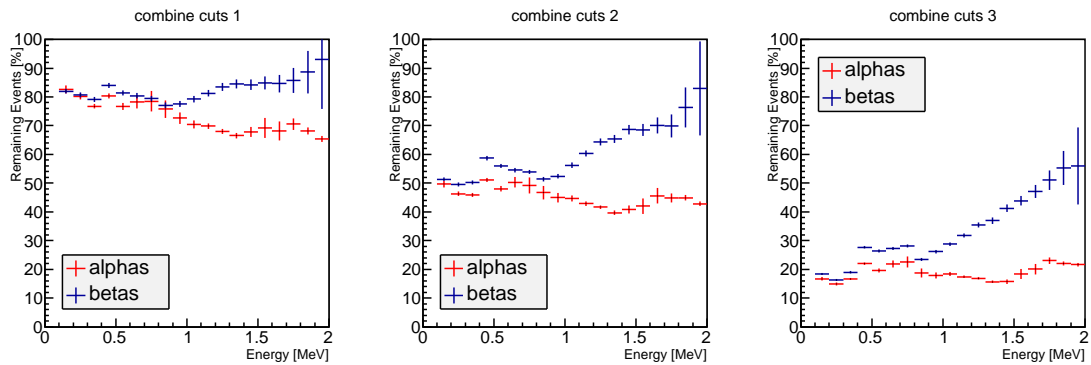
So far, cut values that were determined for a given energy interval were considered constant. It might be beneficial to use dynamic cuts in the plotted dimensions in order to achieve better results. The cuts applied so far would correspond to horizontal and vertical lines in the plots. For a dynamic cut, the alpha and beta populations should split in a way that they might be separated any better by alternative lines, e.g. a diagonal. Such features could not be observed. Therefore the issue of dynamic cuts was not investigated any further.

6.3.3 Discussion

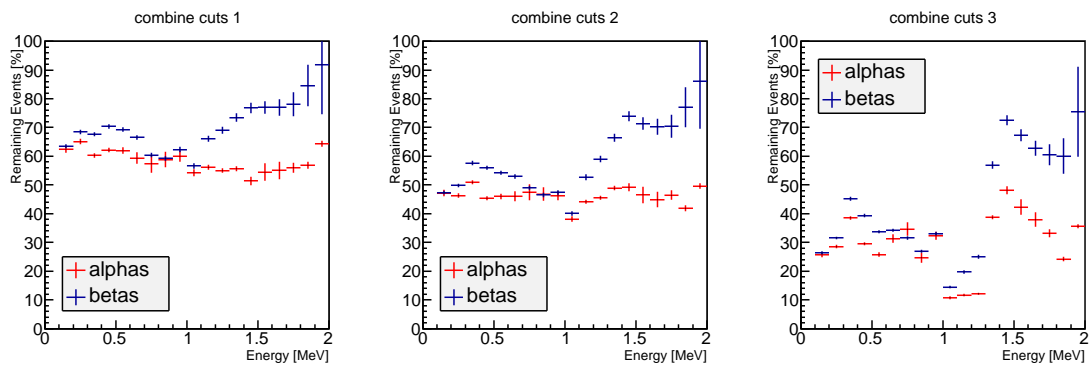
The investigation of cathode events holds valuable information about the potential of alpha discrimination. Since the charge clouds from alphas and betas approach in size for the time of their drift, the cathode marks the point of minimum distinctness. If successful here, the discrimination should work anywhere else in the crystal and is expected to be even more powerful for shorter drift times. Longer drift times occur, if the distance between cathode and anode plane is larger than in the utilized detector, which is the case for the quad grid detectors under investigation for a large-scale setup. It has to be investigated how the cuts perform for cathode events from the quad grid type. However, considering the time development of cloud sizes depicted in figure 5.3 it can be expected that the probability for a discrimination for after $1.5 \mu\text{s}$ of drift is not considerably less likely than after $1 \mu\text{s}$.

One could argue that the discrimination took advantage of the orientation of the beta radiation parallel to the drift direction. Instead, it could be shown with MC methods in section 4.2.1 that the initial flight direction does not have much impact on the spatial extension of the actual charge cloud.

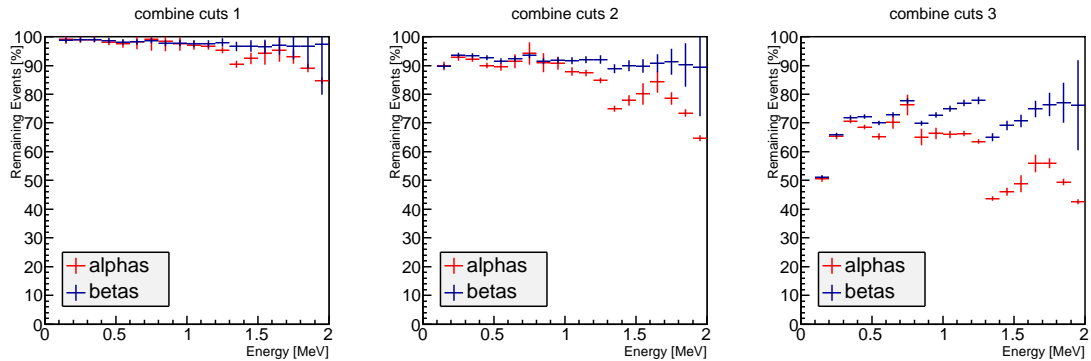
The relative amount of surviving betas can be interpreted as cut efficiency. The amount of



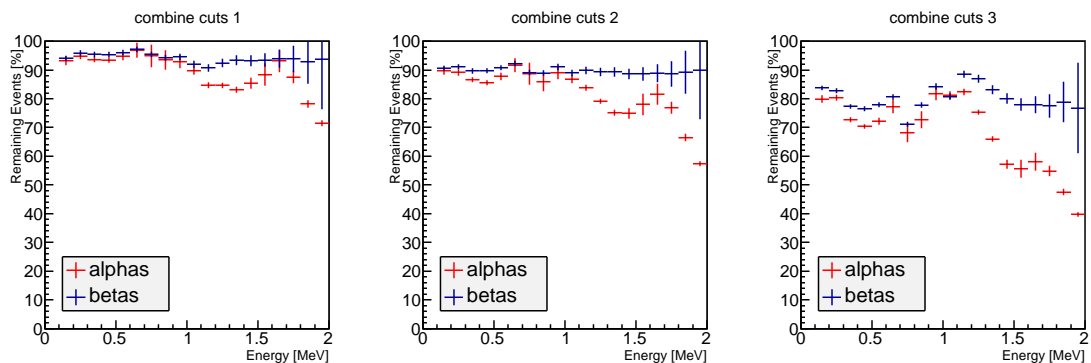
(a) MV smoothing, approach (i): constant alpha ratio of 50 %, combined parameter cuts.



(b) WH smoothing, approach (i): constant alpha ratio of 50 %, combined parameter cuts.



(c) MV smoothing, approach (ii): constant beta ratio of 90 %, combined parameter cuts.



(d) WH smoothing, approach (ii): constant beta ratio of 90 %, combined parameter cuts.

Figure 6.8: Results of alpha discrimination, this time with combined parameters. The plots show the percentage of surviving events after the cut for all considered energy intervals. The error bars refer to statistical uncertainties.

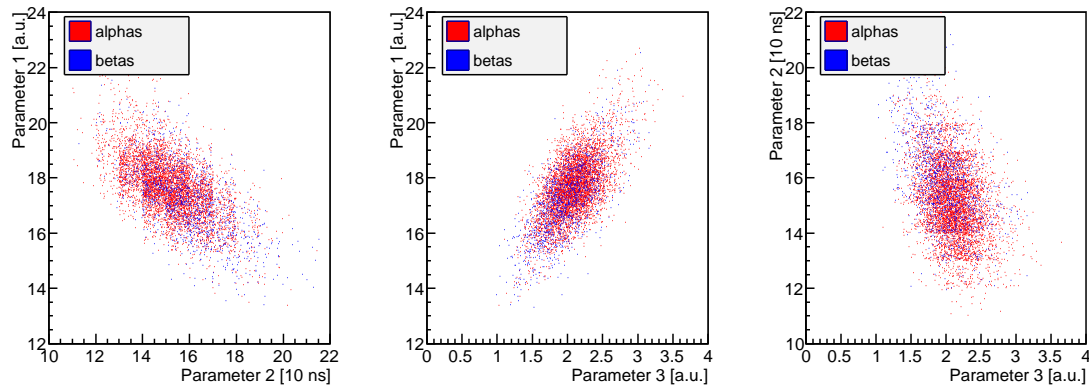


Figure 6.9: Values for different parameters plotted against each other. The example for energies between 1.4 MeV and 1.5 MeV shows that the parameters are slightly correlated. The vertical (horizontal) structure in the first (third) plot is due to the binning of parameter (2).

surviving alphas is defined as cut impurity. In comparison, these quantities are a measure for the quality of the cuts. In the considered cases, the efficiencies exceed the impurities. From a certain energy on, the ability to distinguish between alphas and betas rises with particle energy, which fits the expected behaviour according to which the clouds are very similar in size for low energies.

The results of the pulse shape analysis are a clear indication that events can in principle be distinguished by means of their cloud size. It can be concluded from figure 6.1 that an absolute distinction between alphas and betas is not possible for cathode events due to the wide spread cloud sizes for betas. In this regard, the achieved results are even more convincing.

As the ROI for the ^{116}Cd decay is around 2.8 MeV, efficiencies and impurities for higher energetic particles would be instructive. Unfortunately, it is not easy to get betas with energies above 2 MeV for use in the laboratory and thus such measurements are not applicable.

To test if alphas can in fact be better distinguished at lower interaction depths, scan measurements with alphas and betas at the lateral detector sides are in preparation at TU Dortmund. The bulk region is experimentally hard to access due to the short penetration depths of alphas and betas.

The studies were carried out for both MV and WH smoothed pulses. None of the methods proved significantly more successful than the other. Thus, only the MV method was used for the further analysis. Nevertheless, WH smoothing returned satisfactory results, and should always be considered as an option for future pulse shape analyses which are based on signal differentiation.

6.4 Test with Simulated Data

The experimental access to cut efficiencies is limited. The detector simulation can be used to formulate a hypothesis about the discrimination potential beyond 2 MeV and for detector areas

other than the surfaces. The simulation is used to reproduce the results from measured data and to extrapolate them to higher energies. Furthermore, the cut behavior in terms of interaction depth is investigated. Overall efficiencies are calculated for the whole detector and for lateral side areas only.

6.4.1 Reproduction of Laboratory Measurements

To reproduce the results from measured data, the experimental detector values from table 6.1 were passed as parameters to the detector simulation, together with a noise level determined from pulse samples. The energy range between 0 and 3 MeV was divided into 100 keV intervals. For every interval, 10 000 alphas and betas were simulated to enter the detector from the middle of the cathode side. Their initial direction was set perpendicular to the electrode.

During the analysis, the same steps were performed as for the measured data. The MV method was used for smoothing.

The results are presented in figure 6.10 in addition to the already discussed experimental values. Panels (a) and (b) cover the individual parameter cuts for alpha and beta ratios, respectively. The corresponding results for parameter combinations are given in panels (c) and (d). The simulated alpha and beta ratios were drawn with a dark red and a light blue line, respectively. Statistical errors are below 1 % and not represented in the plots for the sake of clarity.

The first impression of the plots is a general agreement between experiment and simulation. Not only do the associated lines lie very near to each other and are located in the same region, they also show the same tendencies on a similar scale. The experimentally observed trend towards a higher discrimination power at higher energies proceeds beyond 2 MeV. Deviations between experiment and simulation are often below 5 % and rarely higher than 20 %.

A closer look also reveals discrepancies. The simulated lines fluctuate less due to higher statistics. This holds especially for the sudden leaps of the parameter (2) cuts, which occur at different energies but still in accordance with changes in the associated cut values.

The most prominent difference between experiment and simulation is located around 700 keV. The simulation shows an enhanced likelihood for discrimination by means of parameters (1) and (3). This behavior could not be confirmed in the experiment. On the contrary, the experimental ratios of surviving alphas and betas approach in the very same region, although this fluctuation is small. The simulated feature discussed grows and declines over an extended energy range up to 800 keV. A plausible explanation is a connection with the number of simulated spots of energy deposition. Other than for betas, only one spot is simulated for alphas below 800 keV (see section 5.1.2). The detector simulation does not take into account repulsive cloud extensions in that special case. The alpha cloud remains dot like while the beta cloud grows towards higher energies: A systematic error helping to distinguish the clouds. The issue should be fixed in future versions of the detector simulation. Above 800 keV, the amount of energy spots rises fast, providing enough spots for a suitable treatment of repulsion. Since the discussed anomaly is constrained to low energies, the validity of further conclusions from the simulation concerning

the ROI is not affected.

In general, this leaves three major conclusions:

- (i) Disregarding the discrepancy around 700 keV, the experimental results for efficiency and impurity are reproduced well. This is a strong attest for the good performance of the detector simulation.
- (ii) By the same token, this cross-check emphasizes the validity of the experimental outcome.
- (iii) On the basis of argument (i), the predictions for high energies can be considered trustworthy.

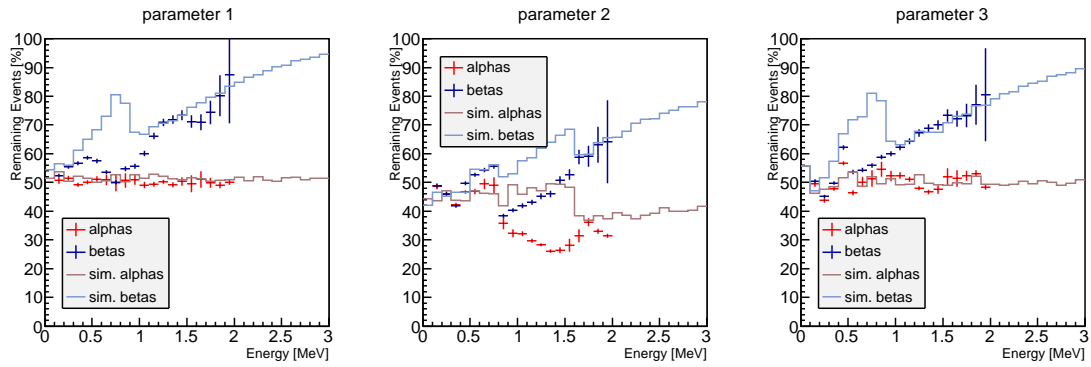
These predictions include the enhanced cut performance to higher energies. Among the individual parameter cuts, parameter (1) with approach (ii) turned out to have the strongest discrimination power with only 10 % beta loss but an alpha reduction by a factor of 5 near 3 MeV. For parameter (2) and approach (ii), the simulation indicates only little success – although the experimental data shows a larger distance between efficiency and impurity even at lower energies. Among the cut combinations, the third criterion returned the most striking divergence between efficiency and impurity. Both for approaches (i) and (ii) about 70 % beta events survived in contrast to about 15 % alphas near 3 MeV.

6.4.2 Depth Dependent Efficiency

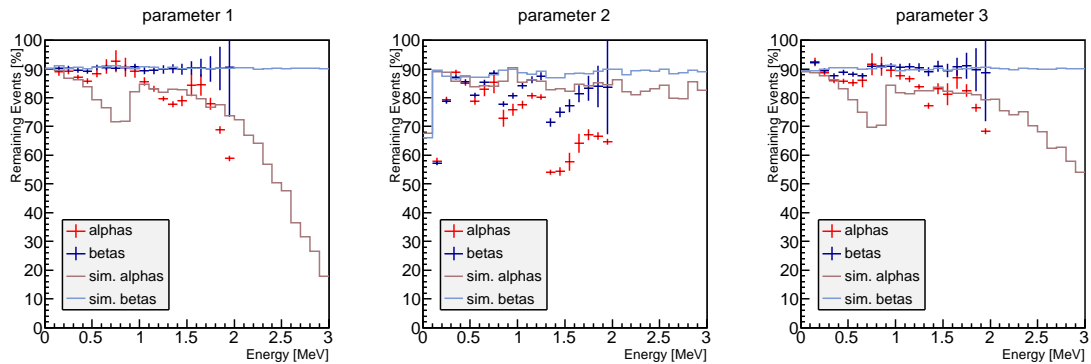
To test the depth dependence of the cuts, efficiencies were calculated for 5 different ranges along the interaction depth. The same energy intervals were considered as before. The initial particle directions were distributed randomly. In practice, the cathode is the only region where cut values for the bulk could be derived from irradiation with particles, since no DIP and ERT features arise here. So the cut values were adopted from the previous cathode simulations and used on the simulated pulses from the entire depth. Every calculated ratio is based on the simulation of 10 000 events. The results for the single parameter cuts are presented in figure 6.11. The two dimensional plots used for cathode events were complemented by the dimension of interaction depth. Within the 3D histograms, the cathode plots would appear as a step function at the backplane of the cube at the interaction depth $z = 1$. The ratios of surviving alphas and betas were plotted separately.

The constant alpha ratio of 50 % (approach(i)), which is the depicted case in panel (a), was required for cathode events. Towards the anodes, more and more alpha events get cut off. This holds also for betas, although the descent is weaker. Apparently, the alpha ratios are not even constant within a fixed depth range: Near the anodes, the amount of remaining alphas decreases with rising energy. At the same time, the rise in surviving betas towards higher energies remains almost constant. The local peak around 700 keV persists throughout all energy ranges.

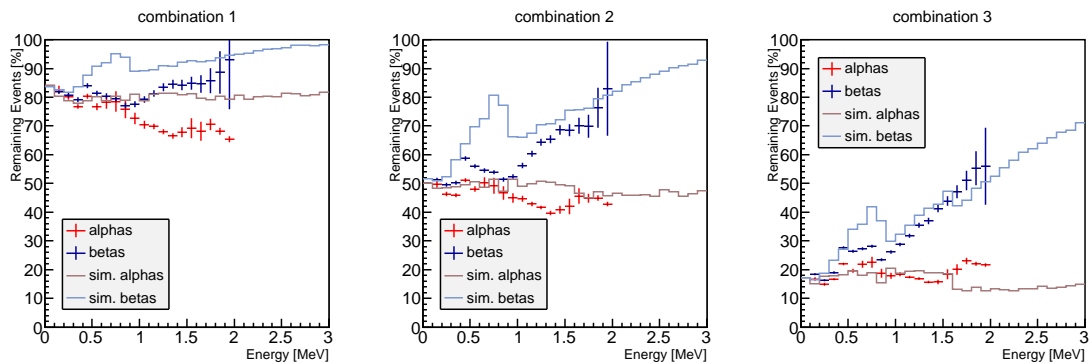
Some general remarks can also be made for the requirement of a constant beta ratio (approach (ii)) at the cathode, see panel (b). For all cuts, the amount of remaining events decreases towards



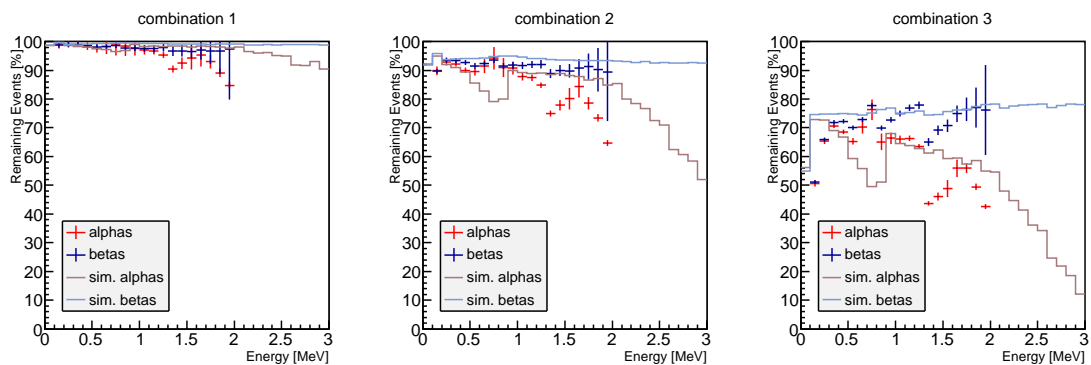
(a) MV smoothing, approach (i): constant alpha ratio of 50 %, single parameter cuts.



(b) MV smoothing, approach (ii): constant beta ratio of 90 %, single parameter cuts.



(c) MV smoothing, approach (i): constant alpha ratio of 50 %, combined parameter cuts.



(d) MV smoothing, approach (ii): constant beta ratio of 90 %, combined parameter cuts.

Figure 6.10: Results of alpha discrimination for cathode measurements and simulation. The plots show the percentage of surviving events after the cut for all considered energy intervals. Statistical errors of the simulation are below 1 % and not represented in the plots.

the anodes, for alphas stronger than for betas, and for parameters (1) and (3) stronger than for parameter (2). For low energies, alpha and beta ratios are almost equal. In case of parameters (1) and (3), both drop along the energy axis until at 700 keV a valley is reached for the beta curve. From there on, the beta ratios start to increase again while for alphas the decrease continues. The valley is most distinctive near the anode plane. For parameter (2), the beta ratios stay constant within a given depth range. For higher energetic alphas, a drop can be observed near the anodes.

The respective results for the combined cuts can be seen in figure 6.12. General trends are a ratio decrease towards the anodes and a rise with energy for betas accompanied by a decrease for alphas. The discussed features around 700 keV show up, too.

Efficiency and impurity diverge along the depth axis for all considered cut criteria. In the previous section it was observed that the single parameter (2) cut with approach (ii) yields only a slight discrimination of simulated alphas. The depth dependent analysis shows that the cut performs much better near the anodes.

It was expected that charge clouds are easier to distinguish for lower interaction depths. Not only do the results of the analysis support this hypothesis, they also give a quantitative impression of the drift impact. Furthermore it can be assumed that the obtained cut values have discrimination power beyond the cathode region. This is an important condition w.r.t. an actual application in the experiment. Even more powerful cuts should be possible if the cut values were made depth dependent. But for this, more extensive studies of clouds in bulk events – not alone on the basis of simulated data – need to be done.

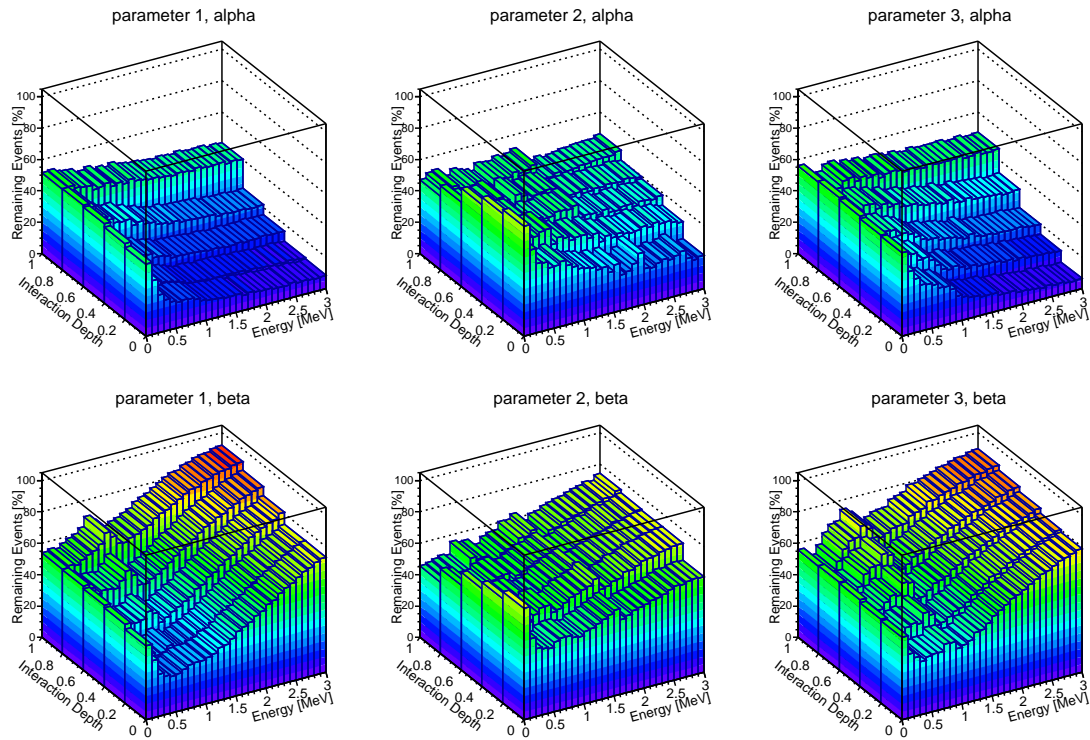
6.4.3 Overall Efficiency

To express the potential of the discrimination in a compact form, alpha and beta ratios have been calculated for the total fiducial volume, i.e. for interaction depths $0.2 < z < 0.97$. 10 000 events were simulated in that region with randomly distributed initial direction. Their energy was set uniformly distributed within the ROI defined as $Q \pm \sigma$, where Q is the Q-value for ^{116}Cd and σ the standard deviation. For an assumed energy resolution $\Delta E = 2\% \text{ FWHM}@Q$, the standard deviation is given by

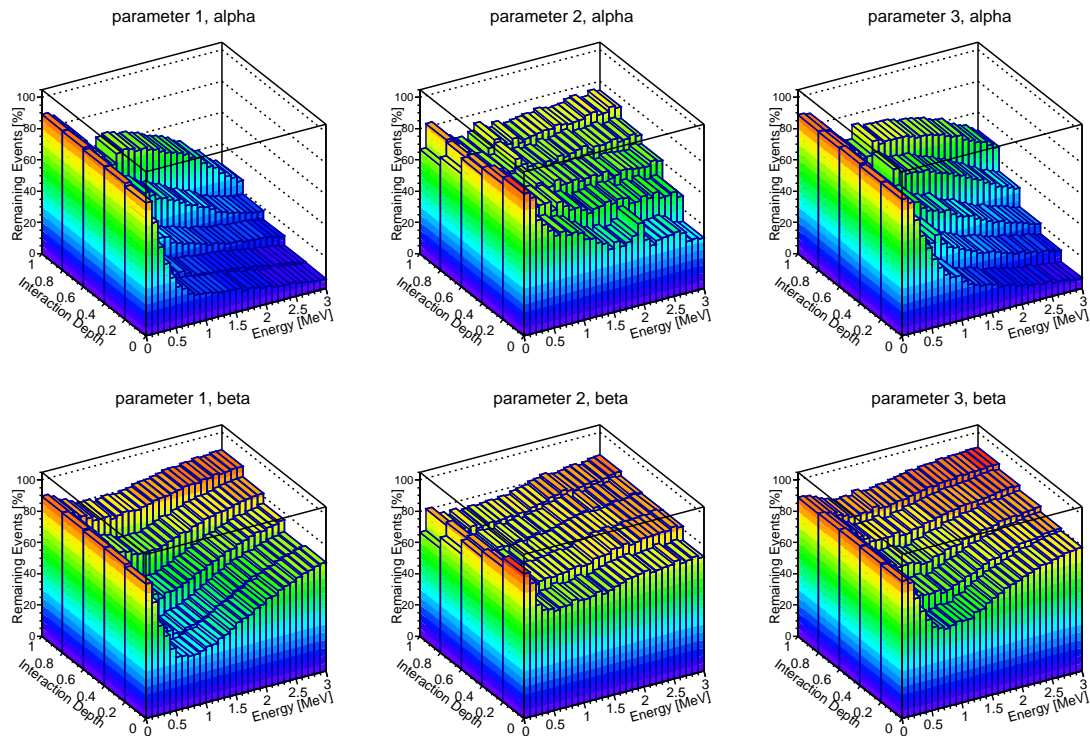
$$\sigma = \frac{\Delta E}{2.355} = \frac{0.02 \cdot 2814 \text{ keV}}{2.355} = 24 \text{ keV} \quad (6.6)$$

[Hei14]. The results are shown in table 6.3. Here, the alpha ratio is referred to as impurity ι_α and the beta ratio as efficiency ε_β .

Since the intention of the discrimination is not to separate alpha events from beta but from double beta events, the simulation was repeated for 10 000 $0\nu\beta\beta$ decays of ^{116}Cd . The VENOM simulation was carried out in combination with the software DECAY0 to account for peculiarities in the kinematics of $0\nu\beta\beta$ decay. The resulting efficiency can also be found in table 6.3 as $\varepsilon_{\beta\beta}$. $\varepsilon_{\beta\beta}$ is generally a little lower than ε_β since the total energy is distributed among two betas

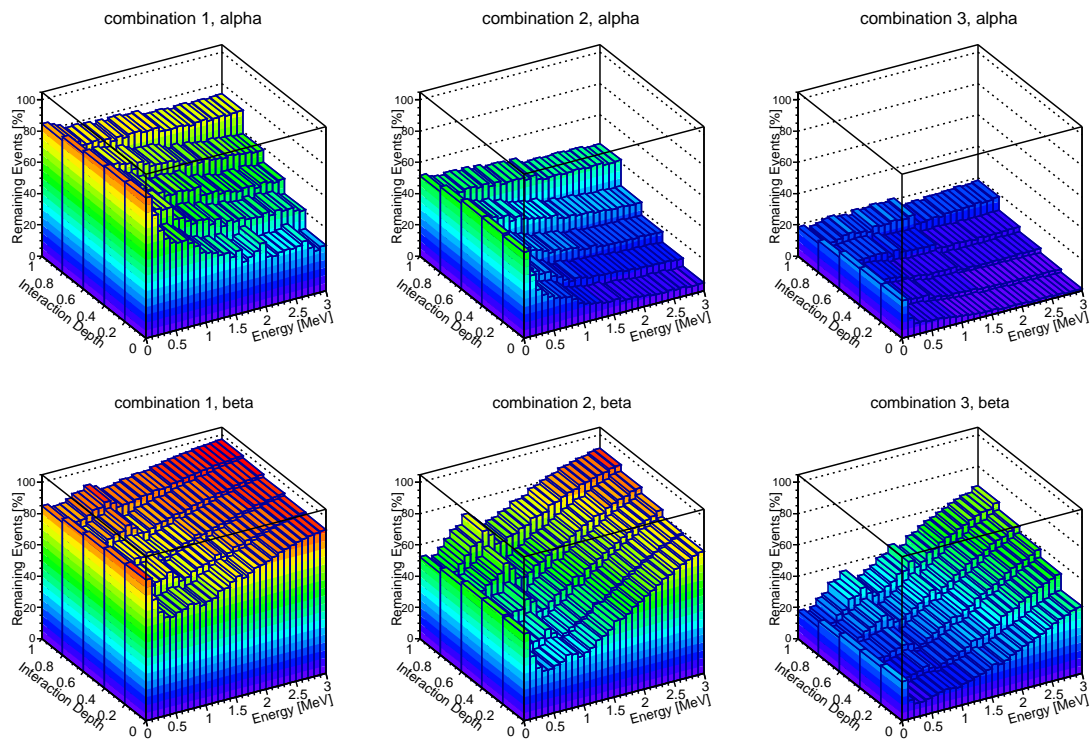


(a) MV smoothing, approach (i): constant alpha ratio of 50 %, single parameter cuts.

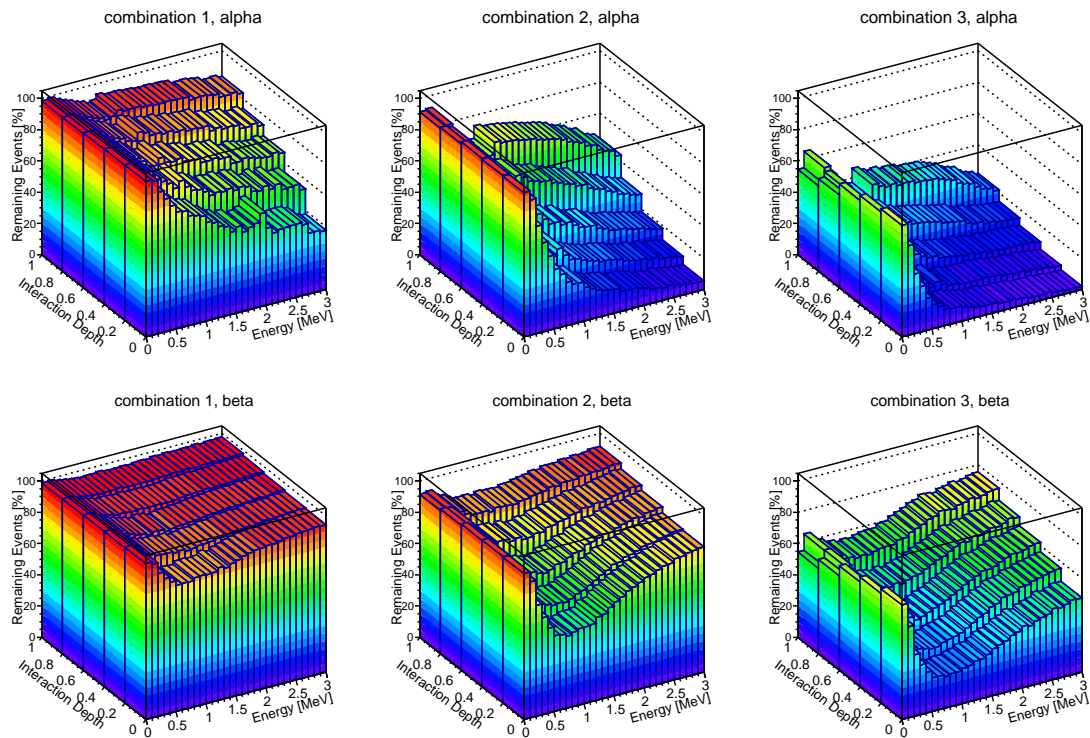


(b) MV smoothing, approach (ii): constant beta ratio of 90 %, single parameter cuts.

Figure 6.11: Results of depth dependent alpha discrimination with individual parameter cuts. The plots show the percentage of surviving events after the cut for all considered energy intervals. Statistical errors are below 1 %.



(a) MV smoothing, approach (i): constant alpha ratio of 50 %, combined parameter cuts.



(b) MV smoothing, approach (ii): constant beta ratio of 90 %, combined parameter cuts.

Figure 6.12: Results of depth dependent alpha discrimination with combined parameter cuts. The plots show the percentage of surviving events after the cut for all considered energy intervals. Statistical errors are below 1 %.

Table 6.3: Efficiencies and gain in half-life sensitivity for the fiducial detector volume. The individual parameter cuts are referred to as P1, P2 and P3. The combined cuts are called C1, C2 and C3.

| Approach | Cut | ι_α | ε_β | $\varepsilon_{\beta\beta}$ | $G_{T_{1/2}}$ |
|----------------------------|-----|----------------|---------------------|----------------------------|-----------------|
| (i): const. α ratio | P1 | 0.23 | 0.83 | 0.72 | 1.49 ± 0.21 |
| | P2 | 0.31 | 0.71 | 0.70 | 1.26 ± 0.18 |
| | P3 | 0.28 | 0.84 | 0.75 | 1.41 ± 0.20 |
| (ii): const. β ratio | P1 | 0.19 | 0.78 | 0.67 | 1.56 ± 0.20 |
| | P2 | 0.48 | 0.81 | 0.81 | 1.17 ± 0.22 |
| | P3 | 0.30 | 0.85 | 0.77 | 1.38 ± 0.17 |
| (i): const. α ratio | C1 | 0.48 | 0.94 | 0.89 | 1.29 ± 0.18 |
| | C2 | 0.25 | 0.85 | 0.75 | 1.51 ± 0.21 |
| | C3 | 0.10 | 0.60 | 0.53 | 1.70 ± 0.24 |
| (ii): const. β ratio | C1 | 0.57 | 0.95 | 0.92 | 1.22 ± 0.17 |
| | C2 | 0.27 | 0.85 | 0.77 | 1.48 ± 0.21 |
| | C3 | 0.13 | 0.63 | 0.57 | 1.55 ± 0.22 |

that in addition produce a smaller charge cloud than a single beta with the total energy.

To make the different cuts comparable, a quantity must be found relating the signal gain due to background reduction to the simultaneous signal loss due to an efficiency $\varepsilon_{\beta\beta} < 1$. A functional and intuitive quantity is given by the half-life sensitivity $T_{1/2}^{0\nu}$ introduced in section 3.4. $T_{1/2}^{0\nu}$ is proportional to the total detection efficiency ε and inversely proportional to the square root of the background index B . The application of the cut would mean a factor of $\varepsilon_{\beta\beta}$ to the total efficiency. If, justified by the strong alpha domination, the background is approximated to be 100 % alpha induced, the effect on B would be a factor of ι_α . The half-life sensitivity $T_{1/2, cut}^{0\nu}$ after the cut can therefore be approximated as

$$T_{1/2, cut}^{0\nu} \approx \frac{\varepsilon_{\beta\beta}}{\sqrt{\iota_\alpha}} T_{1/2}^{0\nu} = G_{T_{1/2}} T_{1/2}^{0\nu} \quad (6.7)$$

with the gain in half-life sensitivity defined as $G_{T_{1/2}} = \frac{\varepsilon_{\beta\beta}}{\sqrt{\iota_\alpha}}$. $G_{T_{1/2}}$ was calculated for all cuts and also listed in table 6.3. The uncertainty was calculated via error propagation and with an assumed uncertainty of 10 % both on ι_α and $\varepsilon_{\beta\beta}$. According to the results, the highest gains can be achieved with the third cut combination, which scores 1.70 at a constant alpha ratio (approach (i)). Several other cuts exceed $G_{T_{1/2}} = 1.5$. For both approach (i) and approach (ii), parameter (1) and the combinations 2 and 3 are among the most powerful cuts.

It has to be emphasized that these numbers refer to an occurrence of alpha decay which was considered uniformly distributed over the entire detector. Under this assumption, the obtained numbers state that the sensitivity in half-life can be increased by 70 % by applying the alpha cut. Actually, most of the background is known to come from the lateral surfaces. This confinement has to be taken into account which will be done in the following section.

6.4.4 Lateral Surface Efficiency

Alpha background at the COBRA demonstrator arises mostly from contaminations at detector surfaces. Events at the cathode and anode side can most effectively be separated by a cut on the interaction depth. Therefore, the performance of the alpha cut at the lateral surfaces is of special interest.

20 000 alpha and beta events were simulated with VENOM. Their origin was set to be at the lateral detector surfaces. Their initial flight direction was distributed randomly, so ca. half of them were directed towards the detector. For these, pulses were calculated with the detector simulation. So far, bulk events were considered. Cut values had to be determined from cathode irradiation. In the case of lateral surface events, it makes sense to irradiate the lateral surfaces and use scan measurements in order to obtain depth dependent cut values. The presented simulations are therefore based on this approach.

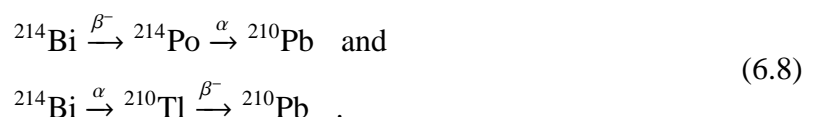
Impurity, efficiency and gain in half-life sensitivity were calculated for four different ranges along the fiducial part of the interaction depth z , i.e. $0.2 < z < 0.97$. The results for all cuts are plotted in figure 6.13. According to expectations, $G_{T_{1/2}}$ drops towards the cathode in every considered case. $G_{T_{1/2}}$ ranges between 1 and 1.4 almost everywhere. To make them comparable to the overall results from the previous section, mean values were calculated and listed in table 6.4. Again, the third cut combination scores the best results with values of $G_{T_{1/2}} = 1.32$ (1.26) for the third cut combination and a constant alpha (beta) ratio, but apparently, even when using depth dependent cut values, the cut works worse near the lateral sides than in the crystal bulk. This can be explained with the special pulse shapes of lateral surface events explained in section 4.1.2. DIP and ERT features have clear impact on the difference pulse and thus also on its differentiations.

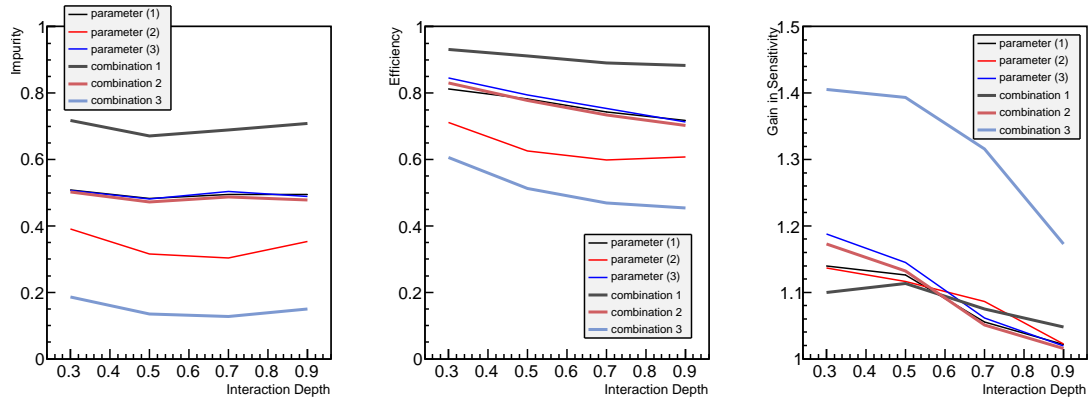
It has however not yet been observed to what extent the presented method removes events that are already flagged as bad events by the LSE cut (see section 4.1.2). Thus the given numbers have to be treated with caution.

It can be assumed that more powerful cuts are possible if the events were generally separated into ERT- and DIP-like pulses before deriving cut values for each class. The approach is left to further investigation beyond this thesis.

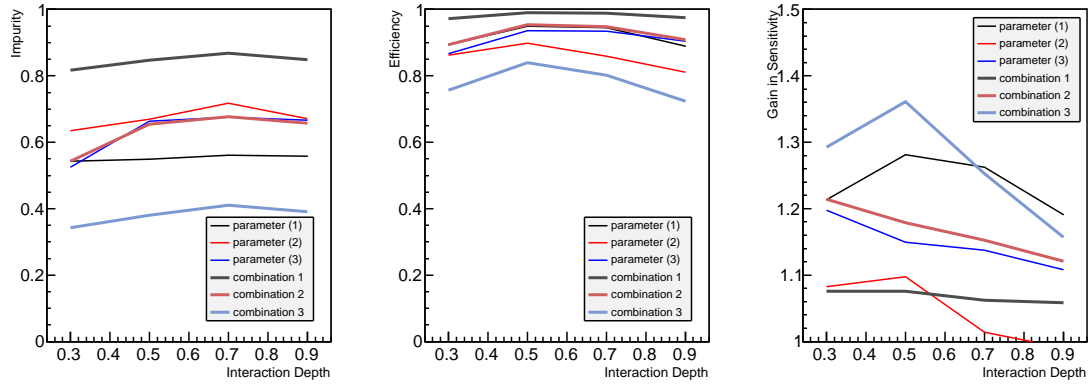
6.5 Test with Coincidence Data

Coincidence analysis is a useful tool to identify sequenced decays. J. Timm searched for coincidences from natural decay chains within the data taken at the COBRA demonstrator [Tim15]. In connection with alpha discrimination, two of the investigated transitions from the uranium chain are of special interest:





(a) MV smoothing, approach (i): constant alpha ratio of 50 %.



(b) MV smoothing, approach (ii): constant beta ratio of 90 %.

Figure 6.13: Results of depth dependent alpha cuts at lateral surfaces.

Table 6.4: Mean values for efficiencies and gain in half-life sensitivity for the lateral surfaces.

| Approach | Cut | ι_α | $\varepsilon_{\beta\beta}$ | $G_{T_{1/2}}$ |
|----------------------------|-----|----------------|----------------------------|-----------------|
| (i): const. α ratio | P1 | 0.50 | 0.76 | 1.09 ± 0.15 |
| | P2 | 0.34 | 0.64 | 1.09 ± 0.15 |
| | P3 | 0.50 | 0.78 | 1.10 ± 0.16 |
| (ii): const. β ratio | P1 | 0.55 | 0.92 | 1.24 ± 0.17 |
| | P2 | 0.67 | 0.86 | 1.04 ± 0.15 |
| | P3 | 0.63 | 0.91 | 1.15 ± 0.16 |
| (i): const. α ratio | C1 | 0.70 | 0.90 | 1.08 ± 0.15 |
| | C2 | 0.49 | 0.76 | 1.09 ± 0.15 |
| | C3 | 0.15 | 0.51 | 1.32 ± 0.19 |
| (ii): const. β ratio | C1 | 0.85 | 0.98 | 1.07 ± 0.15 |
| | C2 | 0.63 | 0.93 | 1.16 ± 0.16 |
| | C3 | 0.38 | 0.78 | 1.26 ± 0.18 |

Table 6.5: Coincidences used for pulse shape analysis [Tim15].

| coincidence | start event | stop event | half-life of stop event |
|-------------------------------------|------------------------------|------------------------------|-------------------------|
| $^{214}\text{Bi} - ^{214}\text{Po}$ | $\beta: E < 3.3 \text{ MeV}$ | $\alpha: 7.7 \text{ MeV}$ | $164 \mu\text{s}$ |
| $^{214}\text{Bi} - ^{208}\text{Tl}$ | $\alpha: 6 \text{ MeV}$ | $\beta: E < 1.8 \text{ MeV}$ | 180 s |

Table 6.6: Energy and time windows used for coincidence search [Tim15].

| coincidence | start energy window | stop energy window | time window |
|-------------------------------------|---|--|-----------------------|
| $^{214}\text{Bi} - ^{214}\text{Po}$ | $0.3 \text{ MeV} < E < 1.5 \text{ MeV}$ | $7.45 \text{ MeV} < E < 8.4 \text{ MeV}$ | $t < 1.6 \text{ ms}$ |
| $^{214}\text{Bi} - ^{208}\text{Tl}$ | $6.1 \text{ MeV} < E < 6.4 \text{ MeV}$ | $0.3 \text{ MeV} < E < 1.8 \text{ MeV}$ | $t < 915.9 \text{ s}$ |

Both contain an alpha and a beta decay and both happen near to each other in the detector. This provides the rare opportunity to compare alpha and beta pulses not only from side but also from bulk events. The first decay in the sequence is searched for within a well-defined energy window. It serves as trigger for the search for the second decay, which has to follow within a certain time and energy window. The decay energies and half-lives are given in table 6.5. The used time and energy windows follow in table 6.6.

23 coincidences of the $^{214}\text{Bi} - ^{214}\text{Po}$ type and 35 coincidences of the $^{214}\text{Bi} - ^{208}\text{Tl}$ type could be found within $134.9 \text{ kg} \cdot \text{days}$ of data. Their pulses were analyzed to determine parameters (1) through (3). Other than for the measurements from section 6.3, the energies from the coincident alphas and betas differ significantly. Although an unorthodox approach, parameters (1) and (3) from alpha events, which are known to be linearly dependent on the energy, were scaled to make them comparable to betas. Parameter (2) was determined without adaptation since here only minor energy dependence is expected. The resulting values were filled into scatter plots, comparing the parameters in pairs. Figure 6.14 shows the plots for all $^{214}\text{Bi} - ^{208}\text{Tl}$ type bulk events, i.e. below an interaction depth of 0.9. Alphas and betas are represented by red and blue marks, respectively.

It might impress at first sight that the alphas and betas are indeed distributed in distinct clouds – even with the event pairs coming from many detectors with different characteristics and voltages. However, their constellation is not the intended one. For a discrimination, parameter (1) and (3) should be higher for alphas than for betas. For parameter (2) it should be the other way round. A constellation in the described way would have been a strong indication that a discrimination is possible for events of similar energy. But apparently the alpha clouds at the considered energies exceed the beta clouds in size due to the large energy difference between alphas and betas.

6.6 Discussion

The cut criteria tested in the analysis proved to hold potential for an alpha discrimination at the COBRA experiment. The studies provide the important finding that pulse shape analysis enables event discrimination by means of cloud sizes although the applied cuts were chosen to

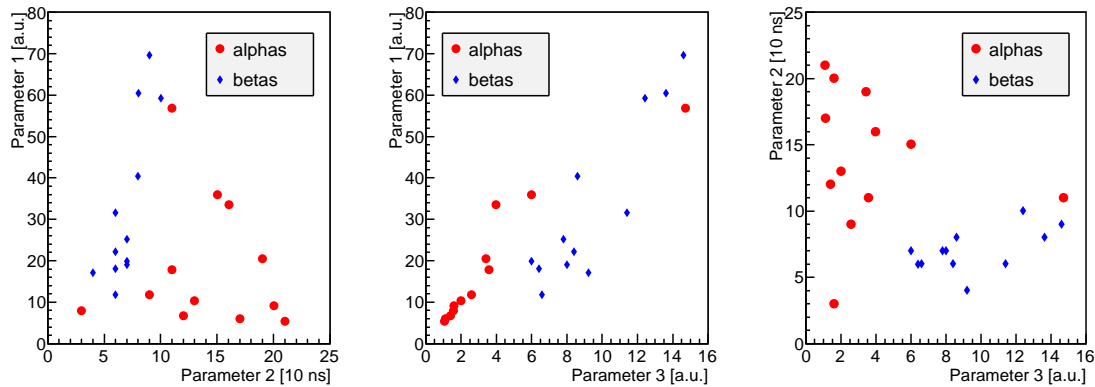


Figure 6.14: Scatter plots with cut parameters obtained from the analysis of coincident event pairs. The plots show all coincident events from the $^{214}\text{Bi} - ^{208}\text{Tl}$ type which have an interaction depth below 0.9.

be static and simple. This opens up opportunities for a variety of future studies.

Known alpha peaks in the energy spectrum can be used as enriched samples in order to determine cut values. It could be insightful to see how the whole spectral shape would react on such a cut. Another interesting aspect could be the study of pulse shapes from double escape events. These can occur subsequent to pair production processes when the emitted positron gets caught by an electron in the detector material and the subsequent annihilation photons escape the detector. The charge clouds generated by the initially produced electron and positron pair are the only contribution to the detector pulse which should in principle be very close to a double beta signal.

So far, the cut values for measured data were obtained experimentally. It is not possible to simply adopt values from the detector simulation. It might be possible to do so in the future, when further development of the simulation allows for the determination of absolute cut values. Thinking of circa 10 000 detectors in a large-scale setup, such a possibility could save a high amount of effort.

From the experimental point of view, the irradiation measurements at the cathode have to be repeated with different detectors to study the dependence of cut parameters and cut performance on intrinsic detector characteristics. Since the drift time proved a crucial factor for a successful discrimination, other HV settings should also be tested. A high bias should make the carriers faster. It might be useful to choose the working point for HV and GB not only w.r.t. energy resolution but to optimize it by means of alpha discriminability. Furthermore, scan measurements with alphas and betas on the lateral detector sides should be done and analyzed in terms of the developed pulse parameters. This could lead to a better understanding of charge drift and improve the cut methods.

The discrimination was studied with the $(1 \times 1 \times 1) \text{ cm}^3$ single grid detector type currently in use at the demonstrator. For a large-scale COBRA setup, $(2 \times 2 \times 1.5) \text{ cm}^3$ quad-grid detectors are favored. Since it was shown that a longer drift diminishes the cut performance, the distance between cathode and anode plane of now 1.5 cm is expected to not be negligible. The cathode measurements and simulations presented in this chapter should be repeated with the larger quad-

grid detectors.

In the long term, the studies lay the foundation for a more complex multivariate analysis using neural networks. Nonetheless, one has to bear in mind that discrimination is only possible if the clouds are actually different when collected, delineating in a way the limiting factor of the method.

The alternative to an alpha discrimination is the reduction of surface events. Up to a certain degree, this is possible with the already used LSE cut. A further analytic approach worth investigation is the $\frac{A}{E}$ criterion used at the GERDA experiment, where the amplitude A of the current pulse, corresponding to the first derivative of the COBRA difference pulse, is divided by the energy E and plotted against E to display pulse features.

It should also be tested both from the experimental side and with simulations if charge clouds from lateral side events can be prevented from being collected at the anodes by modifications of the electric field. These could be due to changes in the anode grid design or to the contacting of the already present guard ring.

Chapter 7

Conclusion and Outlook

The aim of this thesis was to study if and to what extent alpha events in CZT CPG detectors can be discriminated by means of pulse shape analysis. The small size of their charge cloud is the key property for this approach. On the basis of detailed studies regarding formation and transport of charge clouds as well as signal generation, relevant parameters for comparison were defined. Several static cuts were developed and tested on their discrimination power. Measurements of cathode irradiation of a $(1 \times 1 \times 1) \text{ cm}^3$ detector with alphas and betas up to 2 MeV were analyzed and revealed that large parts of the events were in fact distinguishable. It was possible to reduce the alphas to 20 % while nearly 60 % betas survived for 2 MeV particles. This can be regarded as a measurable success. Furthermore, the behavior of cut efficiency and impurity indicates that all cuts perform even better for higher energies including the COBRA ROI. This impression was substantiated by detector simulations. These also confirmed the hypothesis that the discrimination of cathode events is complicated by drift effects and will be more successful near the anodes.

Even though on the one hand a total separation between alpha and beta events was not achieved, the studies show on the other hand that due to high fluctuations of initial cloud sizes for betas and strong electrostatic repulsion for alphas the cloud sizes partially share the same range. From this point of view, the conclusion must be rephrased: The tested methods did not reach a full distinction between alphas and betas, but nevertheless they seem to be quite sensitive to the size of charge clouds. Future analysis methods within and beyond the COBRA experiment can benefit from this important finding.

Assuming a uniformly distributed alpha contamination, the detector simulation predicted that COBRA can increase its half-life sensitivity by $(70 \pm 24) \%$ by using the developed cuts. The applied cut values were determined from cathode events. It is expected that depth dependent cut values will yield even better results.

For a pure surface contamination, the gain is $(32 \pm 19) \%$. At the moment however, an application in the running experiment is impracticable. The cut values have to be derived individually for each detector from irradiation measurements which cannot be done inside the current shielding. For detectors to be installed in the future, it is advisable to perform preliminary studies.

In any case, the subject of alpha discrimination is worth further investigation. This includes scan measurements with alphas and betas at the lateral surfaces. An important aspect is the cut performance in the larger quad-grid detectors. It has to be investigated how the discrimination works for longer drift times. The performed studies are the basis for a more complex multivariate analysis using neural networks.

The detector simulation which was further developed in the course of this thesis turned out to be an important spin-off tool with applications far beyond the described alpha discrimination. Drift effects and impact of electronics were considered, being important steps towards a realistic pulse simulation. Simulations of the electric field were carried out and used to estimate the impact of surfaces and junctions. The detector simulation was used to reproduce the cathode measurements and returned accurate results that resembled very much the experimental outcome. This underlines the quality of the device. Apart from the application in terms of alpha discrimination, the detector simulation has a great significance for the COBRA experiment. It can be manifoldly used, e.g. for pulse studies and efficiency calculation – as already done to calculate COBRA limits on $0\nu\beta\beta$ half-lives [Q⁺15].

Energy resolutions were calculated from simulated pulses. For different detectors, the detector simulation produced resolutions between 1.89 and 1.93 % @662 keV compared to experimental values between 2.38 and 3.21 % @662 keV. The deviation can be explained with individual crystal defects which are not part of the simulation.

Possible improvements of the simulation include the implementation of an enhanced density of trapping centers towards all detector surfaces and the lateral extension of drifting charge clouds, allowing for charge to get lost by crossing a surface. In the future, it will be important to adapt the detector simulation to a quad-grid detector design. In principle, this is a solvable task. The weighting potential has to be recalculated with COMSOL Multiphysics and changes have to be made in the hard-coded detector geometry within the source code.

An improved detector simulation could become of great importance for the alpha discrimination: If the simulation can be used to determine the cut values, a considerable amount of measurement time and effort can be saved in a large-scale COBRA setup.

Appendix A

Natural Decay Chains

Table A.1: Overview on the uranium decay chain [W. 07]. Half-lives and Q-values are given for all decay stages. Branching ratios and emission probabilities are written in brackets behind the Q-value.

| half-life | isotope decay (branch [%]) | α -decay energy [MeV] (branch [%]) | β -decay energy [MeV] (branch [%]) | γ -decay energy [keV] (emiss. prob. [%]) |
|---------------------------|--|--|---|--|
| 4,468 · 10 ⁹ y | ²³⁸ U 100 ↓ α | α : 4,197 (77) α : 4,147 (23) | | γ : 49,55 (0,062) |
| 24,1 d | ²³⁴ Th 100 ↓ β | | β : 0,199 (72,5) β : 0,104 (17,8) β : 0,060 (7,1) | γ : 92,37 (2,42) γ : 63,28 (4,1) γ : 92,79 (2,39) |
| 1,175 m | ^{234m} Pa 100 ↓ β | | β : 2,29 (98,4) β : 1,53 (0,62) β : 1,25 (0,74) | γ : 766,37 (0,316) γ : 1001,03 (0,839) |
| 2,45 · 10 ⁵ y | ²³⁴ U 100 ↓ α | α : 4,775 (72,5) α : 4,723 (27,5) | | γ : 53,20 (0,123) |
| 7,538 · 10 ⁴ y | ²³⁰ Th 100 ↓ α | α : 4,688 (76,3) α : 4,621 (23,4) | | γ : 67,67 (0,38) |
| 1600 y | ²²⁶ Ra 100 ↓ α | α : 4,784 (94,5) α : 4,601 (5,55) | | γ : 186,10 (3,51) |
| 3,8235 d | ²²² Rn 100 ↓ α | α : 5,490 (99,9) α : 4,987 (0,08) | | |
| 3,05 m | ²¹⁸ Po 0,018 99,98 $\beta \swarrow \searrow \alpha$ | α : 6,002 (100) | | |
| ~2 s | ²¹⁸ At ²¹⁴ Pb 85 82 | | β : 0,73 (40,5) | γ : 295,21 (18,15) |
| 26,8 m | $\alpha \searrow \swarrow \beta$ | | β : 0,67 (46) | γ : 241,98 (7,12) γ : 351,92 (35,1) |
| 19,9 m | ²¹⁴ Bi 0,021 99,979 $\alpha \swarrow \searrow \beta$ | | β : 3,275 (19,9) β : 1,88 (7,18) β : (17,5) β : (8,26) β : 1,51 (16,9) β : 1,02 (16,9) | γ : 609,32 (44,6) γ : 768,36 (4,76) γ : 1120,29 (14,7) γ : 1238,11 (5,78) γ : 1764,49 (15,1) γ : 2204,21 (4,98) |
| 1,3 m | ²¹⁰ Tl ²¹⁴ Po 81 84 | α : 7,687 (100) | | |
| 164,3 μ s | $\beta \searrow \swarrow \alpha$ | | | |
| 22,3 y | ²¹⁰ Pb ~100 ↓ β | | β : 0,063 (19) β : 0,017 (81) | γ : 46,54 (4,24) |
| 5,013 d | ²¹⁰ Bi ~100 ↓ β | | β : 1,161 (99) | |
| 138,4 d | ²¹⁰ Po 100 ↓ α | α : 5,305 (99) | | |
| stable | ²⁰⁶ Pb 82 | | | |

Table A.2: Overview on the thorium decay chain [W. 07]. Half-lives and Q-values are given for all decay stages. Branching ratios and emission probabilities are written in brackets behind the Q-value.

| half-life | isotope decay (branch [%]) | α -decay energy [MeV] (branch [%]) | β -decay energy [MeV] (branch [%]) | γ -decay energy [keV] (emiss. prob. [%]) |
|--------------------------|---|---|---|---|
| 1,405·10 ¹⁰ y | ²³² ₉₀ Th 100 ↓ α | α : 4,012 (77,9) α : 3,954 (22,1) | | γ : 63,81 (0,27) |
| 5,75 y | ²²⁸ ₈₈ Ra 100 ↓ β | | β : 0,039 (60) β : 0,015 (40) | |
| 6,15 h | ²²⁸ ₈₉ Ac 100 ↓ β | | β : 2,18 (10) β : 1,70 (11,6) β : 1,11 (31,0) | γ : 338,32 (11,3) γ : 968,97 (16,2) γ : 911,21 (26,6) |
| 1,9131 y | ²²⁸ ₉₀ Th 100 ↓ α | α : 5,423 (71,1) α : 5,340 (28,2) α : 5,221 (0,44) | | γ : 84,37 (1,22) γ : 215,99 (0,28) |
| 3,664 d | ²²⁴ ₈₈ Ra 100 ↓ α | α : 5,685 (94,9) α : 5,449 (5,1) | | γ : 240,99 (4,1) |
| 55,6 s | ²²⁰ ₈₆ Rn 100 ↓ α | α : 6,288 (99,9) α : 5,747 (0,11) | | γ : 549,73 (0,11) |
| 0,145 s | ²¹⁶ ₈₄ Po 100 ↓ α | α : 6,778 (100) | | |
| 10,64 h | ²¹² ₈₂ Pb 100 ↓ β | | β : 0,569 (12) β : 0,331 (83) β : 0,159 (5) | γ : 300,09 (3,25) γ : 238,63 (43,5) |
| 60,55 m | ²¹² ₈₃ Bi 35,94 64,06 α ↙ ↘ β | α : 6,089 (27,1) α : 6,050 (69,9) | β : 2,248 (86,6) β : 1,521 (6,8) | γ : 1620,74 (1,5) γ : 727,33 (6,7) |
| 3,053 m | ²⁰⁸ ₈₁ Tl ²¹² ₈₄ Po β ↘ ↙ α | α : 8,785 (100) | | |
| 0,298 μ s | | | β : 1,80 (51) β : 1,52 (21,7) β : 1,29 (22,8) β : 1,52 (3,1) | γ : 583,19 (30,6) γ : 860,56 (4,5) γ : 511,77 (8,2) γ : 2614,53 (35,8) |
| stable | ²⁰⁸ ₈₂ Pb | | | |

Appendix B

Software

The following paragraphs briefly describe the software tools used for analysis and simulation in the course of the present thesis.

ROOT

ROOT is a modular scientific software framework based on the programming language C++ [httd]. It was developed at CERN and is appropriate for the processing, analysis, visualization and storage of huge data volumes. All histograms and graphs created in the course of this thesis were made with ROOT.

Geant4

The Geant4¹ framework uses Monte Carlo (MC) methods to simulate the passage and transport of particles through matter [httc]. Various models and parameter lists are considered and allow to implement the respective detector materials and geometries. The object-orientated software is based on C++ and was developed at CERN. For the MC simulations presented in this thesis, version 4.10.0 was used.

VENOM

The simulation package VENOM was designed for the special needs within the COBRA collaboration. It can be used for MC simulations of semiconductor detector based double beta experiments. VENOM is object-orientated and uses the methods and models provided by Geant4. The geometries of single detectors, the demonstrator array or even models of the large-scale setup including electronics and shielding can be loaded via GDML files.

Decay0

DECAY0 is an event generator written in FORTRAN for the simulation of particle decays [Tre15]. It was developed to generate the initial kinematics of particles emitted especially in

¹GEometry ANd Tracking

double beta processes. Within this thesis, DECA_{Y0} was used to simulate the neutrinoless double beta decay of ^{116}Cd . The outcome was passed to VENOM.

MANtiCORE

MANtiCORE² is a processing tool written in C++ and based on ROOT. It was designed for COBRA and is used to determine e.g. deposited energy and interaction depth from the raw data. MANtiCORE is also used to flag and reject background and unphysical events. A documentation can be found in [Zat14]. For the pulse shape analysis presented in this thesis, the code was adapted to determine additional information such as extrema of signal derivatives.

COMSOL Multiphysics

COMSOL Multiphysics is a commercial software for the simulation and analysis of physical phenomena in applications [hm]. Coupled problems and physical equations are solved based on the finite element method. For this thesis, version 5.0 was used together with the modules *AC/DC* and *Semiconductor* to simulate the weighting potential and the electric potential inside the detector.

²Multiple Analysis Toolkit for the COBRA Experiment

List of Figures

| | | |
|------|--|----|
| 2.1 | Illustration of mass hierarchies | 13 |
| 2.2 | Effective Majorana mass depending on the lightest neutrino mass | 17 |
| 2.3 | Mass parabolas for $A = 116$ | 18 |
| 2.4 | Schematic view of the Schlegler-Valle theorem. | 20 |
| 2.5 | Overview on nuclear matrix elements for $0\nu\beta\beta$ decay. | 21 |
| 2.6 | Summed electron energy spectra for $2\nu\beta\beta$ and $0\nu\beta\beta$ decay | 22 |
| 3.1 | Contributions of different particle types to the total background | 28 |
| 3.2 | Delrin holder with 4×4 CZT crystals. | 29 |
| 3.3 | Scheme of the current demonstrator shielding at LNGS | 30 |
| 3.4 | DAQ chain of the COBRA demonstrator at LNGS | 30 |
| 3.5 | Interaction depth plotted against energy deposition for LNGS 2011 - 2014 data | 32 |
| 3.6 | Count rate of the demonstrator with 218.9 kg-days exposure | 34 |
| 3.7 | Half-life sensitivities of a possible large scale COBRA experiment | 35 |
| 3.8 | Three different types of CPG detectors | 36 |
| 4.1 | CPG detector scheme | 38 |
| 4.2 | Weighting potentials of CA and NCA in a CPG detector | 40 |
| 4.3 | Selection of typical CPG signals: SSE, MSE, DIP, ERT | 40 |
| 4.4 | Stopping power of alpha and beta particles | 44 |
| 4.5 | Particle ranges for alphas and betas | 45 |
| 4.6 | Cloud extensions for alphas and betas for 1.7 MeV particles. | 46 |
| 4.7 | Example for MC simulated particle tracks | 47 |
| 4.8 | Scheme of anode geometry used in electric field simulations | 51 |
| 4.9 | Simulation of the electric potential of a 1 cm^3 CPG detector | 51 |
| 4.10 | Formation of a Schottky junction | 53 |
| 4.11 | Schottky junction with applied bias | 54 |
| 4.12 | Simulated charge carrier concentrations at Schottky contact, no bias applied . . | 55 |
| 4.13 | Simulated charge carrier concentrations at Schottky contact, 1000 V bias applied | 56 |
| 5.1 | Schematic course of the detector simulation | 59 |
| 5.2 | Charge cloud radius against initial radius considering electrostatic repulsion . . | 62 |

| | | |
|------|--|----|
| 5.3 | Lower and upper limit for the cloud radius plotted against the drift time | 63 |
| 5.4 | Illustration of the effective cloud enlargement | 64 |
| 5.5 | CR high-pass filter and RC low-pass filter | 66 |
| 5.6 | Impact of electronics on simulated pulses | 69 |
| 5.7 | Simulated compared to experimental pulses, $E_{dep} = 2783$ keV | 70 |
| 5.8 | Simulated compared to experimental pulses, $E_{dep} = 2783$ keV | 71 |
| 5.9 | Simulated compared to experimental pulses, $E_{dep} = 255$ keV | 72 |
| 5.10 | Simulated pulses for lateral side events | 72 |
| 5.11 | Energy spectrum from simulated Cs137 decay before and after detector simulation | 73 |
| 6.1 | Cloud radius after drift plotted against particle energy | 76 |
| 6.2 | Signal schemes for dot-like and cloud-like initial charge distributions | 77 |
| 6.3 | Sample pulse: Whittaker-Henderson and mean value smoothing | 79 |
| 6.4 | Energy spectra of measurements with alpha and beta source | 81 |
| 6.5 | Parameter values for events with $1.4 \text{ MeV} < E_{dep} < 1.5 \text{ MeV}$ | 81 |
| 6.6 | Cut values for the considered energy intervals. | 83 |
| 6.7 | Results of alpha discrimination with measurements, individual parameter cuts . | 84 |
| 6.8 | Results of alpha discrimination with measurements, parameters in combination | 86 |
| 6.9 | Search for parameter correlations in scatter plots | 87 |
| 6.10 | Results of alpha discrimination for cathode simulation | 90 |
| 6.11 | Results of depth dependent alpha discrimination, individual parameter cuts . . . | 92 |
| 6.12 | Results of depth dependent alpha discrimination, individual parameter cuts . . . | 93 |
| 6.13 | Results of depth dependent alpha cuts at lateral surfaces | 96 |
| 6.14 | Scatter plots with cut parameters from coincidence data | 98 |

List of Tables

| | | |
|-----|--|-----|
| 2.1 | Current values for mixing angles and squared mass differences | 12 |
| 2.2 | Division of the elementary SM fermions into quarks and leptons | 14 |
| 2.3 | Phase space factor for several double beta isotopes. | 21 |
| 2.4 | Current limits on half-lives for $0\nu\beta\beta$ -decay and effective Majorana masses . . . | 23 |
| 3.1 | List of $0\nu\beta\beta$ candidate isotopes contained in CZT. | 24 |
| 3.2 | Material properties of CZT, CdTe, Ge, and Si | 25 |
| 3.3 | Limits on half-lives for the $0\nu\beta\beta$ candidate isotopes under investigation | 34 |
| 4.1 | Material properties used in the COMSOL simulation | 54 |
| 5.1 | Detector input parameters for simulated pulses | 68 |
| 5.2 | Energy resolutions obtained from the detector simulation | 73 |
| 6.1 | Detector parameters for measurements with alpha and beta sources | 80 |
| 6.2 | Q-values of utilized alpha and beta sources | 80 |
| 6.3 | Efficiencies and gain in half-life sensitivity for the fiducial detector volume. . . | 94 |
| 6.4 | Efficiencies and gain in half-life sensitivity for the lateral surfaces. | 96 |
| 6.5 | Coincidences used for pulse shape analysis | 97 |
| 6.6 | Energy and time windows used for coincidence search | 97 |
| A.1 | Uranium decay chain | 103 |
| A.2 | Thorium decay chain | 104 |

Bibliography

- [A⁺04a] I. Abt et al. A New ⁷⁶Ge Double Beta Decay Experiment at LNGS. 2004.
- [A⁺04b] C. Arnaboldi et al. CUORE: a cryogenic underground observatory for rare events. *Nucl. Instrum. Meth. A*, 518:775–798, 2004.
- [A⁺13] M. Agostini et al. Results on Neutrinoless Double- β Decay of ⁷⁶Ge from Phase I of the GERDA Experiment. *Phys. Rev. Lett.*, 111:122503, 2013.
- [And66] W.W. Anderson. Electron Beam Excitation in Laser Crystals. *Applied Optics*, 5:167–168, 1966.
- [B⁺09] M. Benoit et al. Simulation of charge collection processes in semiconductor CdZnTe γ -ray detectors. *Nucl. Instrum. Meth. A*, 606:508–516, 2009.
- [Bal09] D.S. Bale. Multiple-Scale Analysis of Charge Transport in Semiconductor Radiation Detectors: Application to Semi-Insulating CdZnTe. *Journal of Electronic Materials*, 38:126–144, 2009.
- [BB36] H.A. Bethe and R.F. Bacher. Nuclear Physics A. Stationary States of Nuclei. *Rev. Mod. Phys.*, 8:82, 1936.
- [BD76] J.N. Bahcall and R. Davis. Solar neutrinos: a scientific puzzle. *Science*, 191:264–267, 1976.
- [Bet30] H. Bethe. Zur Theorie des Durchgangs schneller Korpuskularstrahlen durch Materie. *Annalen der Physik*, 397:325–400, 1930.
- [Blo33] F. Bloch. Zur Bremsung rasch bewegter Teilchen beim Durchgang durch Materie. *Annalen der Physik*, 408:285–320, 1933.
- [C⁺71] G. Cavalleri et al. Extension of Ramo’s theorem as applied to induced charge in semiconductor detectors. *Nucl. Instrum. Meth.*, 92:137–140, 1971.
- [Car69] E. Carle. *Die kleine Raupe Nimmersatt*. Gerstenberg Verlag, Hildesheim, 1969.
- [Car06] G.A. Carini. Effect of Te precipitates on the performance of CdZnTe detectors. *Appl. Phys. Lett.*, 88, 2006.

- [Che08] M.C. Chen. The SNO+ Experiment. 2008.
- [D⁺05] B. Dönmez et al. Continued Studies of Single-Sided Charge Sharing CZT Strip Detectors. *Nuclear Science Symposium Conference Record, IEEE*, 3:1408–1411, 2005.
- [D⁺11] A. Dueck et al. Neutrinoless Double Beta Decay, the Inverted Hierarchy and Precision Determination of θ_{12} . *Phys. Rev. D*83, 2011.
- [Dir28] P.A.M. Dirac. The Quantum Theory of the Electron. *Proc. R. Soc. Lond. A*, 117:610–624, 1928.
- [Dre13] M. Drewes. The Phenomenology of Right Handed Neutrinos. *Int. J. Mod. Phys. E*, 22, 2013.
- [eV 13] eV Products Inc. Semiconductor Detector Material Properties, http://www.evproducts.com/pdf/material_prop.pdf. 2013.
- [F⁺13] M. Fritts et al. Analytical model for event reconstruction in coplanar grid CdZnTe detectors. *Nucl. Instrum. Meth.*, A708:1–6, 2013.
- [Fic55] A. Fick. On liquid diffusion. *Poggendorfs Annalen*, 94, 1855.
- [Fri44] O. Frisch. *British Atomic Energy Report BR-49*, 1944.
- [FT⁺14] M. Fritts, J. Tebrügge, et al. Pulse-shape discrimination of surface events in CdZnTe detectors for the COBRA experiment. *Nucl. Instrum. Meth.*, A749:27–34, 2014.
- [Fur39] W.H. Furry. On transition probabilities in double beta-disintegration. *Phys. Rev.*, 56:1184–1193, 1939.
- [G⁺87] E. Gatti et al. Dynamics of Electrons in Drift Detectors. *Nucl. Instrum. Meth. A*, 253:393–399, 1987.
- [G⁺15] D. Gehre et al. Long Term Stability of Underground Operated CZT Detectors Based on the Analysis of the intrinsic ^{113}Cd β^- Decay. 2015.
- [Gle14] T. Gleixner. Rejection of α -particle background for neutrinoless double beta decay search with pixel detectors. *Journal of Instrumentation*, 9, 2014.
- [GP12] A. Giuliani and A. Poves. Neutrinoless Double-Beta Decay. *Adv. High Energy Phys.*, 2012:857016, 2012.
- [Gro14] Particle Data Group. <http://pdg.lbl.gov/2014>. 2014.
- [He01] Z. He. Review of the Shockley-Ramo theorem and its application in semiconductor gamma-ray detectors. *Nucl. Instrum. Meth. A*, 463:250–267, 2001.

- [Hei14] N. Heidrich. *Monte Carlo-based Development of a Shield and Total Background Estimation for the COBRA Experiment*. PhD thesis, Universität Hamburg, 2014.
- [Hen24] R. Henderson. A new method of graduation. *Trans. Actuarial Soc. Amer.*, 25:29–40, 1924.
- [hm] <http://www.comsol.com/comsol/multiphysics>.
- [HM14] Y. Huang and B.-Q. Ma. Constraints on absolute neutrino Majorana mass from current data. *Universe*, 2:65–71, 2014.
- [hn] <https://www.nds.iaea.org/relnsd/NdsEnsdf/QueryForm.html>.
- [hp] <http://www.cremat.com/CR110.pdf>.
- [hta] <http://physics.nist.gov/PhysRefData/Star/Text/ASTAR.html>.
- [htb] <http://physics.nist.gov/PhysRefData/Star/Text/ESTAR.html>.
- [htc] <https://geant4.web.cern.ch/geant4/>.
- [htd] <https://root.cern.ch/>.
- [hte] <http://www3.imperial.ac.uk/pls/portallive/docs/1/71370000.GIF>.
- [htf] http://www.analog.com/media/en/technical-documentation/data-sheets/AD8129_8130.pdf.
- [htg] <http://www.analog.com/media/en/technical-documentation/evaluation-documentation/AD8369.pdf>.
- [JD] Provided by Jürgen Durst, Universität München.
- [Jen41] C.K. Jen. On the induced current and energy balance in electronics. *Proceedings of the I.R.E.*, pages 345–349, 1941.
- [JT] Provided by Jan Timm, Universität Hamburg.
- [K⁺05] Ch. Kraus et al. Final Results from phase II of the Mainz Neutrino Mass Search in Tritium β Decay. *Eur.Phys.J.*, C40:447–468, 2005.
- [KKK06] H.V. Klapdor-Kleingrothaus and I.V. Krivosheina. The evidence for the observation of $0\nu\beta\beta$ decay: The identification of $0\nu\beta\beta$ events from the full spectra. *Mod.Phys.Lett.*, A21:1547–1566, 2006.
- [Kno10] G.F. Knoll. *Radiation Detection and Measurement*. 4th edition, 2010.
- [L⁺15] R. Ahl Laamara et al. Dark neutrinos as Cold Dark Matter. *Astroparticle Physics*, 62:122–124, 2015.

- [Leo94a] W.R. Leo. *Passage of Radiation Through Matter*. Springer Berlin Heidelberg, 1994.
- [Leo94b] W.R. Leo. *Techniques for Nuclear and Particle Physics Experiment*. 2nd edition, 1994.
- [LP14] J. Lesgourgues and S. Pastor. Neutrino cosmology and Planck. *New Journal of Physics*, 16:065002, 2014.
- [Luk94] P.N. Luke. Single-polarity charge sensing in ionization detectors using coplanar electrodes. *Appl. Phys. Lett.*, 65:2884–2886, 1994.
- [Lüt15] H. Lüth. *Solid Surfaces, Interfaces and Thin Films*. 6th edition, 2015.
- [Maj37] E. Majorana. Teoria simmetrica dellelettrone e del positrone. *Il Nuovo Cimento*, 14:171–184, 1937.
- [MNS62] Z. Maki, M. Nakagawa, and S. Sakata. Remarks on the Unified Model of Elementary Particles. *Progress of Theoretical Physics*, 28:870–880, 1962.
- [Mün07] D. Münstermann. *Construction of a Low Background Facility for the COBRA Experiment and its Performance*. PhD thesis, Universität Dortmund, 2007.
- [MV04] R.D. McKeown and P. Vogel. Neutrino masses and oscillations: Triumphs and challenges. *Phys.Rept.*, 394:315–356, 2004.
- [Old15] C. Oldorf. *Operation of CdZnTe Semiconductor Detectors in Liquid Scintillator for the COBRA Experiment*. PhD thesis, Universität Hamburg, 2015.
- [OW08] E.W. Otten and C. Weinheimer. Neutrino mass limit from tritium beta decay. *Rept.Prog.Phys*, 71:086201, 2008.
- [P⁺01] T.H. Prettyman et al. Effect of surfaces on the performance of CdZnTe detectors. *Proc. SPIE*, 4507, 2001.
- [P⁺02] T.H. Prettyman et al. Effect of differential bias on the transport of electrons in coplanar grid CdZnTe detectors. *Nucl. Instrum. Meth. A*, 476:658–664, 2002.
- [Par13] D.S. Parno. The KATRIN Experiment: Status and Outlook. *ArXiv e-prints*, 2013.
- [Pre99] T.H. Prettyman. Thoretical framework for mapping pulse shapes in semiconductor radiation detectors. *Nucl. Instrum. Meth. A*, 428:72–80, 1999.
- [Q⁺15] T. Quante et al. Results of a search for neutrinoless double beta decay using the COBRA demonstrator. 2015.
- [R⁺11] S. Rahaman et al. Double-beta decay Q values of ¹¹⁶Cd and ¹³⁰Te. *Physics Letters B*, 703:412–416, 2011.

- [Rac37] G. Racah. Sulla simmetria tra particelle e antiparticelle. *Nuovo Cimento*, 14:322, 1937.
- [Ram39] S. Ramo. Currents Induced by Electron Motion. *Proceedings of the I.R.E.*, pages 584–585, 1939.
- [Reb13] H. Rebber. Koinzidenzanalysen zur Untersuchung des Einfangs thermischer Neutronen am Cd-113 im COBRA-Experiment, 2013.
- [RR⁺15] G. Rong-Rong et al. Effect of de-trapping on carrier transport process in semi-insulating CdZnTe. *Chin. Phys. B*, 24, 2015.
- [S⁺90] A. Sautd et al. Calculation of 2ν and 0ν Double-Beta Decay Rates. *Europhysics Letters*, 13:31, 1990.
- [S⁺10] G. Sgouros et al. Radiobiology and Dosimetry of α -Particle Emitters for Targeted Radionuclide Therapy. *J. Nucl. Med.*, 51:311–328, 2010.
- [Sch01] T.E. Schlesinger. Cadmium zinc telluride and its use as a nuclear radiation detector material. *Materials Science and Engineering: R: Reports*, 32:103–189, 2001.
- [Sch11] O. Schulz. *Exploration of new Data Acquisition and Background Reduction Techniques for the COBRA Experiment*. PhD thesis, Technische Universität Dortmund, 2011.
- [Sch13] B. Schwingenheuer. Status and prospects of searches for neutrinoless double beta decay. *Annalen der Physik*, 2013.
- [SH93] J. Suhonen and E. Hammarén. Massive neutrinos and right-handed weak currents in double beta decay. *Phys. Rev. C*, 47:757, 1993.
- [Sho38] W. Shockley. Currents to Conductors Induced by a Moving Point Charge. *Journal of Applied Physics*, 9:635–636, 1938.
- [Sin00] J. Singh. *Semiconductor Devices: Basic Principles*. 2000.
- [SV82] J. Schlechter and J.W.F. Valle. Neutrinoless double-beta decay in $SU(2) \times U(1)$ theories. *Phys. Rev. D*25, 2951, 1982.
- [SZ] Provided by Stefan Zatschler, Technische Universität Dresden.
- [Sze07] S.M. Sze. *Physics of Semiconductor Devices*. 3rd edition, 2007.
- [T⁺15] J. Tebrügge et al. The COBRA demonstrator at the LNGS underground laboratory. 2015.
- [Tep01] G.C. Tepper. Investigation of the electronic properties of cadmium zinc telluride surfaces using pulsed laser microwave cavity perturbation. *Proc. SPIE*, 4507, 2001.

- [Tim15] J.H.K. Timm. *Studien seltener neutroneninduzierter Prozesse und Koinzidenzanalysen zur Bestimmung und Reduktion von Untergrundbeiträgen im COBRA-Experiment*. PhD thesis, Universität Hamburg, 2015.
- [Tre15] V. Tretyak. DECAY0 event generator for initial kinematics of particles in alpha, beta and double beta decays, <https://agenda.infn.it/conferenceDisplay.py?confId=9358>. 2015.
- [TW00] T. Takahashi and S. Watanabe. Recent Progress in CdTe and CdZnTe Detectors. *IEEE Transactions on Nuclear Science*, XX:100–109, 2000.
- [vW35] C.F. von Weizsäcker. Zur Theorie der Kernmassen. *Z. Phys.*, 96:431–458, 1935.
- [W. 07] W. Wahl. *Radionuklid-Handbuch für den Anwender in der Spektroskopie im Strahlenschutz und der Medizin*. ISuS Publikationen, 2007.
- [Wat00] J. Watkinson. *The Art of Digital Audio*. 3rd edition, 2000.
- [Wei06] H.L. Weinert. Efficient computation for Whittaker-Henderson smoothing. *Computational Statistics & Data Analysis*, 52:959–974, 2006.
- [Whi23] E.T. Whittaker. On a new method of graduation. *Proc. Edinburgh Math. Soc.*, 41:63–75, 1923.
- [Y⁺99] H.W. Yao et al. Optical engineering and characterization of the internal electric field of CdZnTe radiation detectors. *Proceedings of the SPIE*, 3768:330–338, 1999.
- [Z⁺99] A. Zumbiehl et al. Electric field distribution in CdTe and Cd_{1-x}Zn_xTe nuclear detectors. *Journal of Crystal Growth*, 197:650–654, 1999.
- [Zat14] S. Zatschler. *Identification of Multi-Site Events in Coplanar-Grid CdZnTe-Detectors for the COBRA experiment*. PhD thesis, Technische Universität Dresden, 2014.
- [Zub01] K. Zuber. COBRA – double beta decay searches using CdTe detectors. *Physics Letters B*, 519:1–7, 2001.
- [Zub12] K. Zuber. *Neutrino Physics*. CRC Press, 2nd edition, 2012.

Danke

Ich danke Prof. Dr. Caren Hagner und der Forschungsgruppe Neutrino-physik für die Möglichkeit meine Masterarbeit an diesem spannenden Projekt zu schreiben – und dazu noch in so freundlicher Atmosphäre. Insbesondere bedanke ich mich für die einmalige Gelegenheit, die Berge Italiens eine Woche lang von innen zu sehen. Danke ebenfalls an die COBRA-Kollaboration für eine gute Zusammenarbeit und die herzliche Stimmung bei allen Treffen.

An Björn, Christian, Mari, Nadine, Sarah und Volker geht ein herzlicher Dank für viele wertvolle Korrekturen und die Mühe, die ihr euch damit gegeben habt.

Bei meiner Familie und meinen Freunden bedanke ich mich für jede Art des Rückhalts und der Ablenkung. Bei Ole entschuldige ich mich dafür, dass ich [Zub01] zeitweise mehr Aufmerksamkeit geschenkt habe als [Car69]. Bei dir und Leonie bedanke ich mich für die Geduld und Unterstützung.

Hiermit bestätige ich, dass die vorliegende Arbeit von mir selbständig verfasst wurde und ich keine anderen als die angegebenen Hilfsmittel – insbesondere keine im Quellenverzeichnis nicht benannten Internet-Quellen – benutzt habe und die Arbeit von mir vorher nicht einem anderen Prüfungsverfahren eingereicht wurde. Die eingereichte schriftliche Fassung entspricht der auf dem elektronischen Speichermedium. Ich bin damit einverstanden, dass die Masterarbeit veröffentlicht wird.

Hamburg, den 30. September 2015

Henning Rebber